الجمهورية الجزائرية الديمقراطية الشعبية

الجمهورية الجزائرية الديمقراطية الشعبية

People's Democratic Republic of Algeria

وزارة التعليم العالي والبحث العلمي

Ministry of Higher Education and Scientific Research

جامعة زيان عاشور بالجلفة

Ziane Achour University of Djelfa

كلية العلوم و التكنولوجيا

Faculty of Sciences and Technology

Department: Civil Engineering

Order N° : . …. / 2023

Defense authorization N° ……/2023

DOCTORATE THESIS

Sciences Doctorate

Presented by

Mohamed GUESMI

Submitted in partial fulfillment of the requirements for Doctorate Degree in

Civil Engineering

Specialty: Structures

Title

Contribution to the study of fracture parameters using eddy current sensors and associated signal inversions by an optimization algorithms for crack analysis

Defended, on February 09, 2023 and approved by the jury:

Last and first name	Grade	Institution of affiliation	Designation
Mr. Ahmed HAFAIFA	Professor	University of Djelfa	President
Mr. Salaheddine HARZALLA	MCA	University of Djelfa	Supervisor
Mr. Boubaker BENCHIKH	MCA	University of Djelfa	Co-Supervisor
Mr. Mohamed CHABAAT	Professor	USTHB	Examiner
Mr. Benazouz CHIKH	MCA	ENTP	Examiner
Mr. Mohamed BADAOUI	MCA	University of Djelfa	Examiner
Mr. Fodil DIF	MCA	University of Djelfa	Guest

Djelfa University, FST - 2023

Acknowledgements

Praise to the Almighty God who gave me faith, courage, and patience to carry out this work.

I want to express my deep gratitude to my supervisors Dr. Salaheddine HARZALLAH and Dr. Boubaker BENCHEIKH from Djelfa University, for the confidence they placed in me, their presence always with me, their availability, listening, and orientation, and for their constructive remarks.

I would like to express my sincere gratitude to Ahmed HAFAIFA Professeur at Djelfa University for heading the examination jury.

My special thanks go to Professor Mohamed CHABAAT from the University of Sciences and Technology Houari Boumedien for accepting to judge my work and for his valuable comments, remarks, and suggestions to deliver a better version of the achieved work.

I would like to thank infinitely, Benazouz CHIKH, associate professor at the National School of Built and Ground Works Engineering (ENTP),Mohamed BADOUI and Fodil DIF Associate Professors at the University of Djelfa, and Khaled TOUNSI Associate Professor at the ENTP, for their acceptance to judge my work, and for their precious remarks, discussions, and questions to enhance further the manuscript.

I would like to thank Professors Kamel GUESMI and Abdellah KOUZOU for their remarks and help with the manuscript preparation. I would like to thank everyone who helped me improve this work and who gave me any remarks to enhance the manuscript's quality.

Dedication

I dedicate this work:

To my dear mother and my dear father who never stopped to support me, support me and encourage me during my years of study. May they find here the testimony of my deep gratitude and acknowledgement

To my brothers and my sisters, my grandparents and my family who give love and liveliness.

To all those who have helped me - directly or indirectly - and those who shared with me the emotional moments during the accomplishment of this work and who warmly supported and encouraged throughout my journey.

To all my friends who have always encouraged me, and to whom I wish more success.

Thanks!

Mohamed GUESMI 

ملخص

من أحد اهم الأسباب الرئيسية لانهيار الهياكل هو الشق الذي يعرف بخصائصه التى هي موقعه واتجاهه. للكشف عن مثل هاته الخصائص ، هناك العديد من تقنيات الاختبار غير المدمر. اخترنا من هاته التقنيات نهج اختبار الكهرباء الدوارنية. في هذا السياق ، لدينا ثلاثة مساهمات رئيسية. أولا ، قمنا بتحسين النموذج التناظرى ثنائي الابعاد للكشف عن اتجاه الشق وأظهرنا التأثير المباشر لشق على مقاومة المستشعر. ثانيا، مددنا المساهمة الى النموذج ثلاثي الأبعاد وقمنا بتطوير معادلة تجريبية تعطي بشكل آلي زاوية الشق بدلالة إشارات الكهرباء الدوارنية. ثالثا، اقترحنا نهجا محسنا بديلا للكشف عن زاوية الشق فى حالة المشكلة العكسية وفشل الأساليب المباشرة لانجاز المهمة. النتائج التي تم الحصول عليها من خلال عمليات المحاكاة المقدمة توضح فعالية التقنية المقترحة لاكتشاف اتجاه زاوية الشق. أثبتت نتائج المحاكاة صحة المساهمات الرئيسية الثلاثة وأظهرت فعالية الأساليب المقترحة لاكتشاف وتوصيف زاوية اتجاه الشقوق.

كلمات مفتاحية : زاوية الشق ، الكهرباء الدوارنية ، الاختبار غير المدمر ، المعاوقة ، طريقة العناصرالمحدودة ، عامل شدة الإجهاد ، التكامل-ج ، النموذج التناظرى ثنائي الابعاد ، النموذج ثلاثي الأبعاد ، مشكلة عكسية ، تحسين.

Abstract

One of the major causes of structures collapse is the crack characterized by its location, dimensions, and its orientation. To detect such parameters, there are many non-destructive testing techniques. We selected among them the eddy current testing approach. In this context, we have three main contributions. Firstly, we enhanced the axisymmertic model for the detection of the crack orientation and we showed the direct effect of the crack orientation on the sensor impedance. Secondly, we extended the contribution to the 3D model and developed an empiric function that systematically relates the crack orientation to the eddy current signals. Thirdly, we proposed an alternative optimized approach to detect the crack orientation for the case of inverse problem and failure of the direct methods to accomplish the task. The simulation results validated the three main contributions and demonstrated the effectiveness of the proposed approaches for the detection and characterization of the crack orientation angle.

Key words: *Crack orientation, Eddy Current, Non-Destructive Testing, Impedance, Finite Element Method, Stress Intensity Factor, J-Integral, Axisymmetric Model, 3D Model, Inverse Problem, Optimization.*

Résumé

L'une des principales causes de l'effondrement des structures est la fissure caractérisée par son emplacement, dimensions et son orientation. Pour détecter ces paramètres, il existe de nombreuses techniques des essais non destructives. Nous avons sélectionné parmi eux, l'approche de test à courant de Foucault. Dans ce contexte, nous avons trois contributions principales. Premièrement, nous avons amélioré le modèle axisymétrique pour détecter l'orientation de la fissure et nous avons montré l'effet direct de la fissure sur l'impédance du capteur. Deuxièmement, nous avons étendu la contribution au modèle 3D et nous avons développé une fonction empirique qui relie systématiquement l'orientation de la fissure aux signaux de courant de Foucault. Troisièmement, nous avons proposé une approche optimisée alternative pour détecter l'orientation des fissures dans le cas du problème inverse et l'échec des méthodes directes pour accomplir la tâche. Les résultats de simulation ont validé les trois principales contributions et ont démontré l'efficacité des approches proposées pour la detection et la characterisation de l'angle d'orientation de la fissure.

Mots clés :*Orientation des fissures, Courant de Foucault, Essais Non Destructives, Impédance, Methode des Eléments Finis, Facteur d'Intensité de Contraintes, J-intégral, Modèle Axisymétrique, Modèle 3D, Problème Inverse, Optimisation.*

Sources of Images

for Copyright purposes

Figure 2.1

https://www.flyability.com/inspection-tools

Figure 2.3

www.nationalboard.org/index.aspx?pageID=164&ID=377

Figure 2.5

www.magnumndt.com/different-types-of-weld-defects-phased-array-radiography-blog

Figure 2.6

www.visionenergy.com.my

Figure 2.7

www.indiamart.com/proddetail/infrared-thermography-testing-service-24009381462.html

Figure 2.8

www.qualitymag.com/articles/96942-eddy-current-inspection-of-in-service-aircraft-structure

Figure 2.17

blog.bestknow.my.id/what-are-eddy-currents-write-their-two-applications.html

Figure 2.19

www.mechanicalbooster.com/2018/10/what-is-induction-heating.html

Contents

List of Figures

List of Tables

Abbreviations & Symbols

Abbreviations

NDT : Non-Destructive Testing
EC : Eddy Current
IGMRM : Improved Giant Magneto-Resistance Magnetometer
TMR : Tunnel Magneto Resistive
2D : Two dimensions
3D : Three dimensions
SIF : Stress Intensity Factor
LEFM : Linear Elastic Fracture Mechanics
CTOD : Crack Tip Opening Displacement parameter
EPRI : Electric Power Research Institute
EFPM : Elastic-Plastic Fracture Mechanics
NDE : Non-Destructive Evaluation
PT : Penetrant Test
ECT : Eddy Current Testing
UV : Ultra Violet
RT : Radiography Testing
UT : Ultrasonic Testing
NDT-EC : Non-Destructive Testing by Eddy Current
HHO : Harris Hawks Optimization
PDE : Partial Differential Equation
DSTO : Defence Science and Technology Organisation
NUEC : Near Unidirectional Eddy Current
LB,UB : Lower and Upper bounds of the search area,

Symbols

G	: Energy release rate or Griffith energy
E	: Young's modulus
σ^{∞}	: Remote applied stress
a	: Half-length of the crack
G_c	: Toughness
r, β	: polar coordinates
σ_{xx}, σ_{yy}	: normal components of the stress
τ_{xy}	: tangential component of the stress
K_I, K_{II}, K_{III}	: Stress intensity factor for I , II, III modes
K_{Ic}	: Tenacity of the material
θ	: Crack orientation
W	: Pate's width
σ_{YS}	: Yield stress
r_y	: First-order estimate of plastic zone size
r_p	: Second-order estimate of the plastic zone size
a_{eff}	: effective crack length
Y	: Geometry correction factor.
ρ	: Length of the plastic zone
K_{eff}	: Effective stress intensity factor
C_{ij}	: Coefficients for the Dynamic stress intensity factor
δ	: Crack Tip Opening Displacement parameter
J	: J-integral
Γ	: Closed path contour
w_s	: Strain energy density
t	: Traction vector
$\overrightarrow{n}$	: Outer normal
u	: Displacement vector
J^{act}, J^{aux}	: J-integral actual and auxiliary states
M	: interaction integral
w_s, w_s, w^M	: The strain energy density for the actual, auxiliary states and interaction
J_1,J_2	: J-Integral for modes I and II
d_m	: Constant in relation between the J-integral and CTOD

σ_0, τ_0	: Magnitudes of normal and shear stress pulses
f_I^d, f_{II}^d	: Functions of the propagation velocity of crack
c_l, c_s	: Longitudinal and shear wave speeds of the material
c_R	: Rayleigh wave speed.
c_l, c_s	: Longitudinal and shear wave speeds of the material. ν is the Poisson's ratio
ν	: Poisson's ratio
K_{Ic}^d	: Dynamic crack initiation toughness
K_{tt}	: Dynamic maximum hoop stress intensity factor
v_c	: Propagation velocity
ΔK	: stress intensity factor range for fatigue cycle
da/dN	: Crack growth rate
K_{max}, K_{min}	: SIF at the maximum and minimum stress values for each loading cycle
C, m	: constant and exponent of the Paris model
$daor\Delta a_i$	: Growth increment
dN	: Fatigue cycle increment
J_z	: Skin effect
z	: Depth of the tested plate
J_s	: : Current density
f	: Excitation frequency
μ_r	: Relative magnetic permeability
μ_0	: Magnetic permeability of the vacuum
σ	: Electrical conductivity
δ_z	: Penetration depth
F_l	: Lorentz force
q	: charge particle
V	: speed of the charge
E, B	: Electric and magnetic fields
ρ	: Electric load distribution
$\overrightarrow{J}$	: Current density
dl	: Small portion of the coil wire
I_i	: electric current in turn i
n	: Number of turns
$\overrightarrow{E}$	: electric field
$\overrightarrow{H}$	: magnetic field
$\overrightarrow{B}$	: magnetic induction

$\overrightarrow{D}$	: electric induction
ϵ	: electric permittivity
ϵ_0	: electric permittivity of vacuum
$\overrightarrow{J}_s$	: imposed current density
$\overrightarrow{J}_{ind}$	: induced current density
$u[m/s]$	: scan movement of the coil
$\overrightarrow{A}$	: magnetic vector potential
V	: electric scalar potential
$\vec{e_r}, \vec{e_\varphi}, \vec{e_z}$	: unitary vectors in cylindrical coordinates
$\vec{i}, \vec{j}, \vec{k}$	: unitary vectors in cartesian coordinates
Γ_a	: boundary with Dirichlet condition
Γ_s	: boundary with Neumann condition
Γ_m	: boundary with mixed condition
ψ_i	: projection functions for each element i
α_i	: interpolation function for the element i
R_i^e	: elementary residue
R_i	: global residue
ne	: number of finite elements
$[K], [M], [L]$	: global matrices that contains all characteristic of the studied domain
(A)	: global magnetic vector potential
(F)	: global vector of source current
R_{eq}	: average radius of the element e
Z	: sensor impedance
υ_p	: penalty term
Ω_i, Ω_c, Ω_a	: sensor, studied plate,air regions
N_l^s	: vector shape function of node l
(X^s)	: Elementary vector of magnetic potential and electric scalar
R	: resistance
X	: reactance
W_m	: stored in the entire space
P_J	: joule losse
Ld, Wd	:length and width of tested plate
I_0	: amplitude of current source
ΔZ	: normalized impedance
$Z0$	: impedance of the plate without crack

Lf	: Lift-off
J_x, J_y	: eddy current components
B_x , B_y	: magnetic flux density components
T	: number of iterations.
LB, UB	: lower and upper band of the search area
fit	: fitness function
dZ_{est}	: estimated normalized impedance using the optimization
dZ_{exp}	: experimental value of the normalized impedance

General introduction

Durability of structures and their resistance against degradation agents, have been a major challenge for researchers and industrial partners for decades. Among these agents there are cracks and corrosion under environmental effects and overloading conditions. As a consequence, they strive to design and produce new materials, and also to develop new devices for diagnosing structures and materials in an attempt to optimize their durability and lifetime. Moreover, safety is critical for quality requirements, especially in high-risk domains such as civil engineering, mechanical engineering, aeronautical engineering, petroleum engineering, marine engineering, electrical engineering, and so on.

The fracture phenomenon is the main cause of structures collapse, because all other agents are mainly create cracks, which significantly reduces the lifetime of structures, posing a serious threat to society and the economy. On one hand, this phenomenon has piqued the interest of researchers, who are working to develop approaches and tools to diagnose the behavior of cracks and their propagation. On other hand, it is obvious that the detection of cracks and their geometric parameters is crucial point in the domain of fracture mechanics. To deal with this problem, many experimental techniques called the Non-Destructive Testing (NDT) are developed to investigate the main properties and the flaws of materials, components, structures, and systems under use or under operation without causing any kind of damage to the tested objects. Among these techniques, the eddy current testing took great interest because of its effectiveness in identification, detection, localization, and even prediction of different kinds of cracks and their orientation from macro-scale to micro-scale.

The birth of the eddy current (EC) in conductive objects is due to the presence of electromagnetic induction when the these objects are placed in front of probe coils supplied by an alternative current. The signal of induced eddy current provides all information about the material's electric characteristics and/or cracks. In fact, researchers, industrialists and practitioners are still investigating and developing new eddy current probes technologies with higher sensibility and accuracy to enhance the ability of prediction and sizing the flaws in structures and objects under test [1-7]

In the present manuscript, the detection approach based on the eddy current testing has been chosen to be the main tool of detection due to its strong theoretical base, its effectiveness and its ease of coding. Furthermore, it has a large spectre of use for detection of corrosion, fatigue dangerous zones and thickness of layers in composite materials.

Our effort in this manuscript is mainly focused on two points; the first is the study of the influence of the crack orientation on the eddy current created in the materials or structures under study. The second is performing an investigation on the interaction relationship between this kind of currents and the cracks state and their orientations.

During the last three decades, only a few researchers were interested in the use of the eddy current for the detection of cracks orientation. In 1998, Yu et al. developed a new technique for inducing the extended eddy currents in metallic structures which was tested on a conducting plate allowing them to detect subsurface flaws using a superconducting quantum interference device magnetometer [1]. In 2004, Perz et al. designed and built a magnetic imaging system associated with eddy current technique for analysing the fatigue cracks under rivet of aircraft planar structures [2]. In 2006, Dolabdjian et al. proposed a detection approach of fatigue cracks close to fasteners using an improved rotating head built around an Improved Giant Magneto-Resistance Magnetometer (IGMRM), where it was found that the proposed technique seems to be very accurate for this kind of cracks [3]. In 2009, Rimond et al. implemented a 3-D finite-element model using an IGMRM applied for the detection of corrosion on some benchmarks [4]. In 2010 Lei et al.[5] used the results, carried out from their previous research[6], for predicting pulsed signals of eddy current and for the design of new probe topologies. In 2012, Yang et al. [7] developed an eddy current-giant magnetoresistive sensor system with a good ability for the detection of the subsurface cracks. In 2014, Rimond et al. [8] proposed a approach validated numerically and experimentally with a new excitation technique to improve the detection results of internal cracks with arbitrary orientation. In 2015, Chaofeng et al. [9] proposed a prototype probe using a finite-element model and validated experimentally in diagnosing a cracks in a two-layer aluminum sample. In 2016, Mengban et al. [10] studied the possibility of finding the optimum excitation frequency to enhance the prob sensitivity for surface defect detection. The proposed approach was a combination of the kernel principal component analysis method and the support vector machine technique. In 2019, Chaofeng al. [11] presented an eddy current probe based on orthogonal excitation coils with the ability to change the exciting current direction electrically without a mechanical tool. A tunnel magnetoresistive (TMR) sensor was used for the examination of samples of stacked carbon fiber reinforced polymers. In the same year Repelianto et al. [12]

proposed a new rotating uniform eddy current probe built based on two pairs of excitation coils placed perpendicular to each other and in two different layers. It was proved that this topology can provide larger induction and enhance the prob sensitivity for flaws detection. Furthermore, the proposed probe was validated experimentally on a sample of aluminum plate with arbitrary flaws.

Recently, many researches were interested to ensure the detection of hidden cracks using rotating focused eddy current without the aid of mechanical tools. However, this may causes the generation of noises and, thus, affecting the sensing and measurements accuracy. In 2020, Zhiyunan et al. [13] has developed a rotating focused eddy current formed of two pairs of coils on the shape of eight placed orthogonally to each other and in the same layer. It has been proved that it presents a good sensitivity for detecting the crack regardless of its orientation. However, the approach presented a major drawback in its topology which is the identical magnetic flux density curves for all crack orientations. It means that the authors have not taken into account the crack orientation effect which has an significant impact on the main parameters calculation in fracture mechanics.

To deal with the most part of the aforementioned limits, especially those presented in recent studies and to ensure detection of cracks and prediction of their orientation in an optimal way, this manuscript is organized as follows:

In **chapter one**, the definitions of the most important principles of fracture mechanics are presented, focusing on the importance of crack orientation and how to use it for the calculation of the important parameters of the fracture mechanics. In **chapter two**, a brief review on the common used NDT testing techniques are presented, than more concepts and benefits of the eddy current testing are detailed to justify its selection to detect the crack orientation. In **chapter three**, and initially, the mathematical formulation of problem are developed, secondly a numerical implantation based on the finite elements method is done for axisymmetric and 3D models. In **the last chapter**, the validation of the proposed solutions is done in two cases of direct problem and the inverse one. In the direct problem type, an axisymmetric model of tested rod using an absolute sensor is simulated to demonstrate and quantify the influence of crack orientation on the sensor impedance. Then, a 3D model of the investigate plate using multi turn coil is given to study the influence of the crack orientation on the components of eddy current and the magnetic flux density. We proposed, after, an empiric relation that relate the crack orientation as function of the eddy current output signals. In the inverse problem we use the Harris Hawks Optimization(HHO) to find the best crack orientation corresponding for a given value of the sensor impedance.

Chapter 1

Fracture mechanics

1.1 Introduction

During the ancient times, cracks were not a real problem due to the primitiveness of buildings, and if it existed, it did not present any risk to people's lives. However, with the increase of human requirements, the complexity of construction methods and the invention of new complex and heterogeneous materials, cracks became one of the most important challenges that researchers try to avoid, treat, manage their risks and even predict its propagation specially for the case of internal or hidden cracks in brittle materials. All research efforts, devoted in this direction, formed the well-known science of fracture mechanics.
This chapter addresses the basics of this field of science. It starts with a historical review of the important theories in this domain, followed by the most important basic concepts of linear, elasto-plastic and dynamic fractures, to end with the dynamic or propagation of cracks.

1.2 Historical review

Among the most important domains, in which researchers pay great attention to fractures, we can mention the aviation industry, the nuclear domain, the heavy industries, the shipbuilding, the pipelines for transporting petrochemicals and gas ...etc. Furthermore, for safety purposes, the designers of residential complexes, towers and technical facilities (bridges, dams, tunnels, ...etc.); also take the concept of fractures in the first place of their priorities. Indeed, cracks may lead to material disasters, human life losses and have a huge impact on the economy as shown in [14]. Indeed, this study estimated the annual cost of fractures in the United States

during 1978 by 119 billion dollars or about 4% of the USA national product. In addition, it is estimated that this loss invoice could be reduced considerably if fracture mechanics research were applied to reduce the risks of cracks.
Generally speaking, the failure of any structure is caused, mainly, by one of the following major factors:

- Ignorance of the design and/or construction imperfections and inappropriate use of facilities.
- Design and/or use of new materials without a rigorous study of their interaction with old ones.

Fracture research was early started with experimental studies carried out by Leonardo Da-Vinci [15].He observed that the strength of iron wires is inversely related to the length of the wire, and the possibility of the defects' existence increases.
Several centuries ago, The scientist Griffith [16] was the first who established a quantitative relationship between fracture stress and the flaw size. He used the approach developed by Inglis [17] for the case of crack's unstable propagation. He developed a fracture theory based on the energy balance using the first law of thermodynamics. He announced that when the strain energy increase, the crack becomes unstable and propagates large enough to balance the material's surface energy.
Griffith model proved his efficiency for brittle material like glass and ceramic materials. Nevertheless, this modelling technique remains inapplicable for ductile materials until 1948 when several correctional approaches were developed to take into account the plastic zones around the crack.
Irwin developed in [18] a significant contribution to extend Griffith's method to metals by considering energy dissipated by local plastic Flow. After that, he established the energy rate approach [19], based on Griffith theory; the concept used to solve many engineering problems. He also demonstrated in [20], that the stresses and displacements around the crack can be characterized by a parameter of the energy release rate using the Westergaard technique [21]. This parameter was called later "the Stress Intensity Factor"(SIF).
The scientist Wells proposed in [22] the use of earlier fracture approaches to demonstrate that reaching critical size of fatigue cracks is the main cause for aircraft crashes. The cracks initially starts near the square corners of windows, because of the high-stress concentration, and ends to the catastrophic crashes.
Authors in [23] used the Irwin's energy release rate approach to predict the cracks of big

rotors in steam turbines. They were predicted the exploding behavior of huge disks to avoid rotor fractures.

In the same context and despite the powerful experimental and theoretical evidence for their approach, Paris and his colleagues were stacked to publish and convince technical journals community by their ideas on application of fracture mechanics to analyze fatigue crack propagation. After many unsuccessful attempts, they finally published their study [24] in the Washington University periodical called *Trend in Engineering*.

For years of hard work, researchers around the world established the foundations of Linear Elastic Fracture Mechanics (LEFM), and they started focusing on crack plasticity. Numerous researchers performed studies to take into account the effect of the plastic zone around the crack to improve the LEFM approaches. Among them we can mention the works of: Irwin [25], Dugdale [26], Barenblatt [27] and Wells [28]. The plastic zone correction approach given in [25] was a simple extension of LEFM, whereas approaches in [26] and [27] created more complex models using a small strip of yielding material near the crack.

In [28] authors noticed that when fracture is accompanied with considerable plasticity, the displacement of the crack faces can be considered as an alternative fracture criterion. When Wells attempted to apply LEFM to ductile materials, he observed that the crack faces move separately with plastic deformation and as a result he introduced the Crack Tip Opening Displacement parameter(CTOD).

In another research direction, Rice proposed in [29] a new parameter to quantify the nonlinear behavior of cracked materials. It is done by adjusting the energy release rate for nonlinear materials and considering plastic deformation as nonlinear elastic. He described this nonlinear energy release rate by the J-integral calculated along the contour around the crack. Rice used the integral developed by Eshelby in [30] for fracture problems. Authors in [31] and [32] proposed a process for relating the J-integral to crack stress fields and according to this relation, the J-integral is served as a nonlinear stress intensity parameter as well as an energy release rate.

Begley and Landes proposed in [33] to quantify the fracture toughness of steels using the J-integral and their experimental plant had achieved great success and considered after that as a standard protocol for J-testing of metals [34].

The relationship between toughness, stress, and crack size allows using the linear fracture mechanics concepts for design purposes. Shih and Hutchinson [35] proposed the theoretical framework for the nonlinear fracture design analysis using J-integral. Based on this study, a fracture design handbook [36] was published, after that, by the Electric Power Research In-

stitute (EPRI). In [37] a mathematical relation was developed between J-integral and CTOD to show that both parameters are equally diagnosing the crack state.
In recent years, the combination of the J-based approaches from USA and structural design methodologies (CTOD) from UK, become an effective solution to select and to combine the best aspects of each one and to deliver successful analysis of fracture problems.
In the last two decades, plasticity received a lot of interest in fracture studies, by incorporating time-dependent nonlinear behaviors such as viscoplasticity and viscoelasticity. These studies gain recently more interest due to the urgent need for tough creep-resistant, high-temperature materials and composite materials in structural applications. In addition, new directions of research, on the fracture problems in micro and nanoscale are appeared, to deliver microstructural models for fracture; models that can relate the local behavior of fractures and the global one. They allow also nanoscale analysis of the crack in microelectronics domain. The main and important approaches, in the context of our contributions, will be delighted carefully in the last chapter of this manuscript.

1.3 Linear elastic fracture mechanics

The concepts of LEFM are widely used to analyze brittle fracture. These concepts are limited just to fractures in linear elastic materials. Indeed, the LEFM are only valid under conditions of limited plasticity around the crack. There are two methods in LEFM to study brittle fracture. The first one depends on the energy balance and determines the necessary condition for the fracture. The second one is based on calculating the stress intensity near the crack tip and compare it to a critical value for brittle fracture. These two approaches will be detailed in the next sections and we will demonstrate that they are equivalent and therefore one of them, is sufficient, to accomplish the task.
The design criteria in classical mechanics versus those in fracture mechanics are illustrated in Figure 1.1. According to classical mechanics, the material is eligible if its strength is larger than the expected applied stress (Figure 1.1a). In the other side, the fracture mechanics criterion has two more important structural variables: the crack size and the fracture toughness. This last is considered as the critical property of a material instead of its strength.

1.3.1 Griffith energy balance

The energy approach states that the crack extension occurs when the energy available for crack growth is sufficient to override the resistance of the material. The first energy criterion

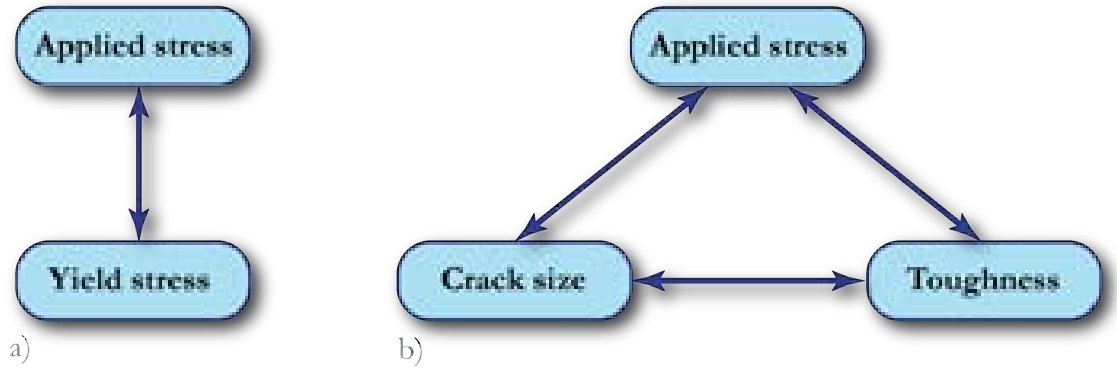

Figure 1.1: Design criteria: a)classical mechanics, b)fracture mechanics.

was proposed by Griffith in [16] followed by the one of Irwin [19] called the energy release rate G. For a linear elastic material, it is defined as the rate of change in potential energy with crack area. At the moment of brittle fracture $G = G_c$ with G_c the critical value of this energy.

If we consider the infinite plate given by Figure 1.2 where the crack dimensions are infinitesimals compared to those of the plate, the energy release rate for a crack of length $2a$ subject to a remote tensile force is given by:

$$G = \frac{\pi(\sigma^{\infty})^2 a}{E} \tag{1.1}$$

where E is Young's modulus, σ^{∞} the remote applied stress and a is the half length of the crack . Toughness G_c is independent of the size and geometry of the cracked body and this

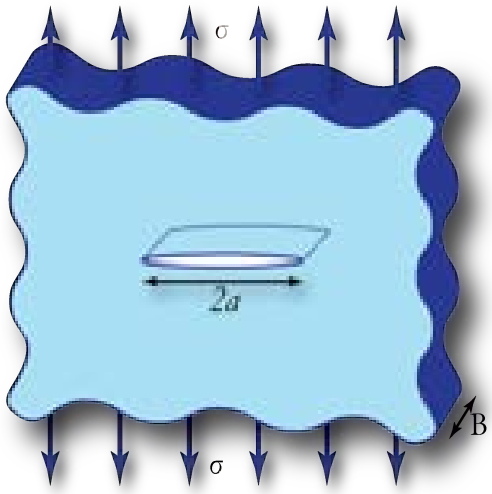

Figure 1.2: Internal crack in an infinite plate subject to a remote tensile stress.

is one of the basic assumptions of fracture mechanics. The measured fracture toughness on a laboratory specimen should be applicable to the structure. It can be done by taking into account all configuration effects and the material behavior should be predominantly linearly elastic.

1.3.2 Stress intensity approach

All possible movements of the crack lips (surfaces) are combined by the three modes shown in Figure 1.3.

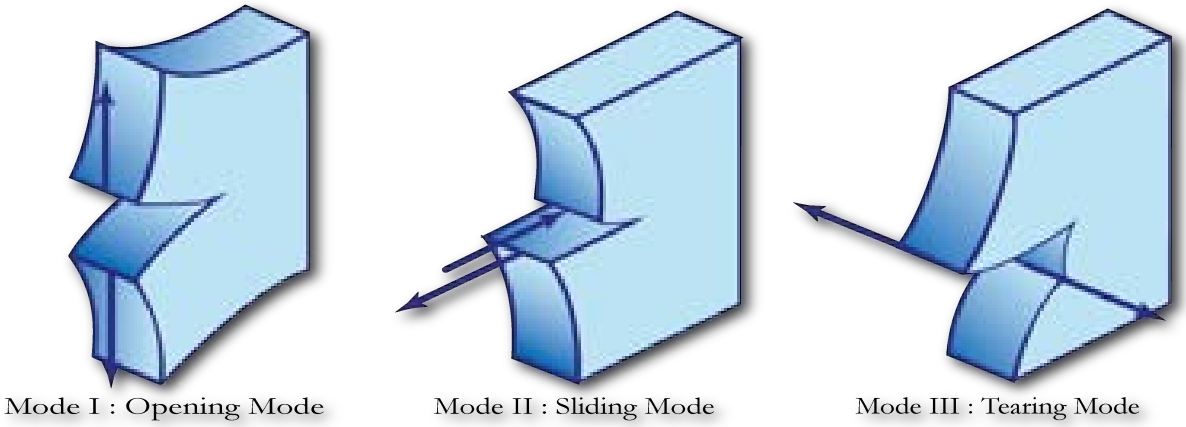

Figure 1.3: Modes of fracture.

Figure 1.4 shows the constraints on an element centered on a point M identified by the polar coordinates r, β relative to the crack tip on opening mode (mode I). These constraints are

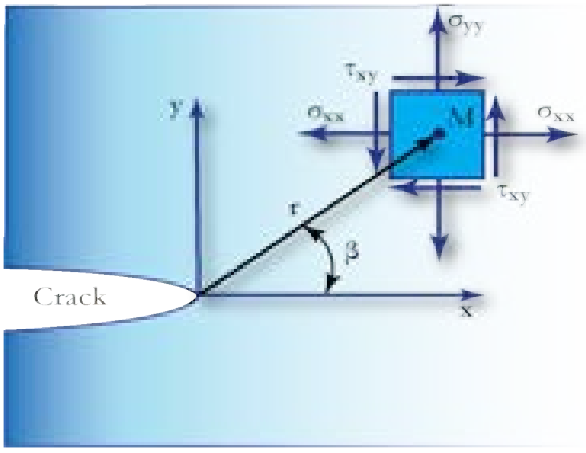

Figure 1.4: Stresses near the crack tip.

expressed in terms of the SIF K_I given, in mode I, by: (1.2).

$$\begin{cases} \sigma_{xx} = \frac{K_I}{\sqrt{2\pi r}} \cos\beta/2(1 - \sin(\beta/2)\sin(3\beta/2)) \\ \sigma_{yy} = \frac{K_I}{\sqrt{2\pi r}} \cos\beta/2(1 + \sin(\beta/2)\sin(3\beta/2)) \\ \tau_{xy} = \frac{K_I}{\sqrt{2\pi r}} \cos\beta/2\sin(\beta/2)\cos(3\beta/2) \end{cases} \tag{1.2}$$

in mode II by:

$$\begin{cases} \sigma_{xx} = -\frac{K_{II}}{\sqrt{2\pi r}} \sin\beta/2(2 + \cos(\beta/2)\cos(3\beta/2)) \\ \sigma_{yy} = \frac{K_{II}}{\sqrt{2\pi r}} \sin\beta/2\cos(\beta/2)\cos(3\beta/2) \\ \tau_{xy} = \frac{K_I}{\sqrt{2\pi r}} \cos\beta/2(1 - \sin(\beta/2)\sin(3\beta/2)) \end{cases} \tag{1.3}$$

and in mode III is:

$$\begin{cases} \sigma_{13} = -\frac{K_{III}}{\sqrt{2\pi r}} \sin\beta/2 \\ \sigma_{23} = \frac{K_{III}}{\sqrt{2\pi r}} \cos\beta/2 \end{cases} \tag{1.4}$$

The expression of K_I in the case of internal crack in the infinite plate of Figure 1.2 is:

$$K_I = \sigma^\infty \sqrt{\pi a} \tag{1.5}$$

By comparing the formulas (1.1) and (1.5), it appears that:

$$G = K_I^2/E' \tag{1.6}$$

with $E' = E$ for plane stress; $E' = \frac{E}{1-\nu^2}$ for plane strain where E is the Young's modulus and ν the Poisson's ratio.

The Stress Intensity Factor (SIF) concept is summarized in the following criterion:

- $K_I = K_{Ic}$: the crack suddenly propagate, where K_{Ic} is the tenacity of the material (critical value of K_I).
- $K_I < K_{Ic}$: the crack is stable.

1.3.3 Mixed mode crack within an infinite plate

Considering an oriented internal crack in an infinite plate as shown in Figure 1.5. If the crack orientation $\theta \neq 0$, the crack is loaded in both modes I and II. Hence, we choose axes x' and y' that coincide with the crack orientation as depicted in Figure 1.5b. The applied stress can be decomposed into normal and shear components. The stress normal component

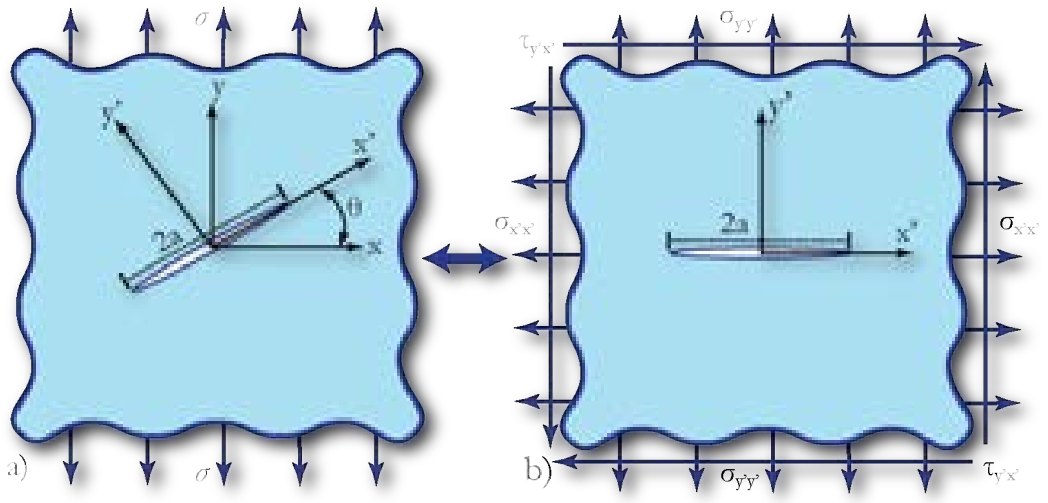

Figure 1.5: Infinite plate with crack on mixed mode.

$\sigma_{y'y'}$ produces pure mode I loading, while $\tau_{x'y'}$ applies mode II loading. The stress intensity factors relating $\sigma_{y'y'}$ and $\tau_{x'y'}$ to the applied stressσ and the crack orientation θ using Mohr's circle is given by:

$$K_I = \sigma_{y'y'}\sqrt{\pi a} = \sigma cos(\theta)^2\sqrt{\pi a} \tag{1.7}$$

$$K_{II} = \tau_{x'y'}\sqrt{\pi a} = \sigma sin(\theta)cos(\theta)\sqrt{\pi a} \tag{1.8}$$

The expressions (1.7) and (1.8) highlight the effect of the crack orientation on the SIF value.

1.3.4 Crack on a plate with finite width

It's obvious that the plate boundaries have no effect on the crack, unless they are near the crack tip. If we consider a cracked plate with finite width $2W$ subject to a remote tensile stress, the stress distribution is affected by the crack tip. The stress lines are concentrated around the crack tips whether the plate width is infinite or not as illustrated in Figure 1.6. However, the stress is more concentrated in the case of finite plate (Figure 1.6b) than it in the case of infinite plate (Figure 1.6a). The mode I stress intensity factor for this situation is given by :

$$K_I = \sigma\sqrt{\pi a}\left[\frac{2W}{\pi a}\tan\left(\frac{\pi a}{2W}\right)\right]^{1/2} \tag{1.9}$$

Using polynomial approximation [38], the finite element analysis has provided more accurate expression given by:

$$K_I = \sigma\sqrt{\pi a}\left[\sec\left(\frac{\pi a}{2W}\right)^{1/2}\right]\left[1 - 0.025(a/W)^2 + 0.06(a/W)^4\right] \tag{1.10}$$

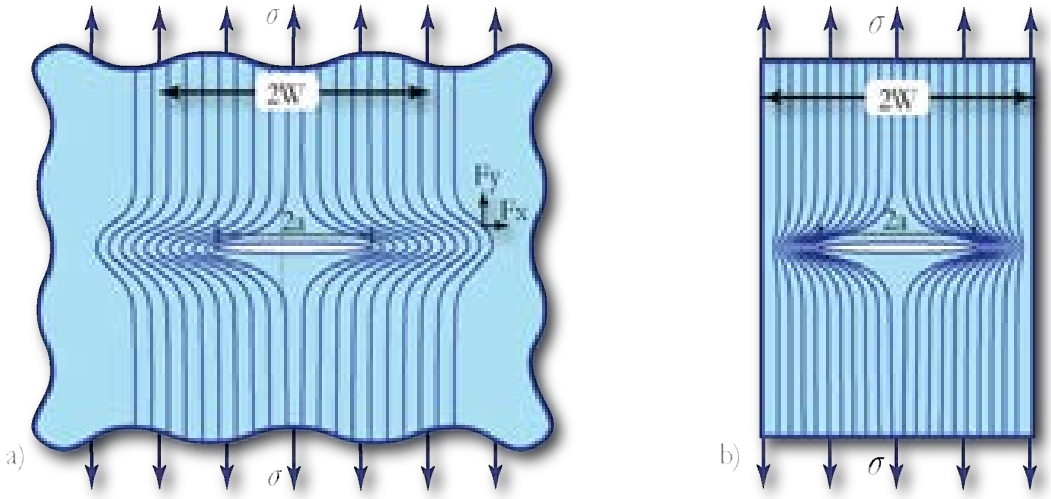

Figure 1.6: Influence of the plate dimension on the stress distribution.

1.3.5 Superposition principle

The principle of superposition illustrated in Figure 1.7 shows that stress intensity factors for different loading types are additive provided all loading types tend to open the crack. In traditional mechanics and for 2D linear elastic materials imposed by different external forces, the stress, strain, and displacement components in the same direction are additive. The total σ_x is obtained by the sum of normal stresses in the x-direction. However, this is not case with a shear stress. Similarly, the stress intensity factors are only additive for the same mode of loading. It means $K_I = K_I^1 + K_I^2 + .. + K_I^n$; for different loads $(n = 1, 2, ...)$ but for different modes $K_I \neq K_I^1 + K_{II}^1 + K_{III}^1$. In the case of a semi-elliptical surface crack subject to an internal pressure P (Figure 1.7a), the principle of superposition can be used to determine the stress intensity factor. Among the simplest cases of fractures is the semi-elliptical surface crack under uniform remote tension p shown in Figure 1.7b. Another case is depicted in Figure 1.7c and characterized by an uniform compressive stress P applied on the crack surface. This situation leads to closed crack faces and the plate acts as an intact one, i. e. $K_I^c = 0$. The subtraction of the stresses shown in Figure 1.7c from the one given in Figure 1.7b, leads to the stress intensity factor of Figure 1.7a expressed as:

$$K_I^a = K_I^b - K_I^c = K_I^b - 0 = K_I^b \tag{1.11}$$

The aforementioned example shows one of the benefits of the superposition principle.

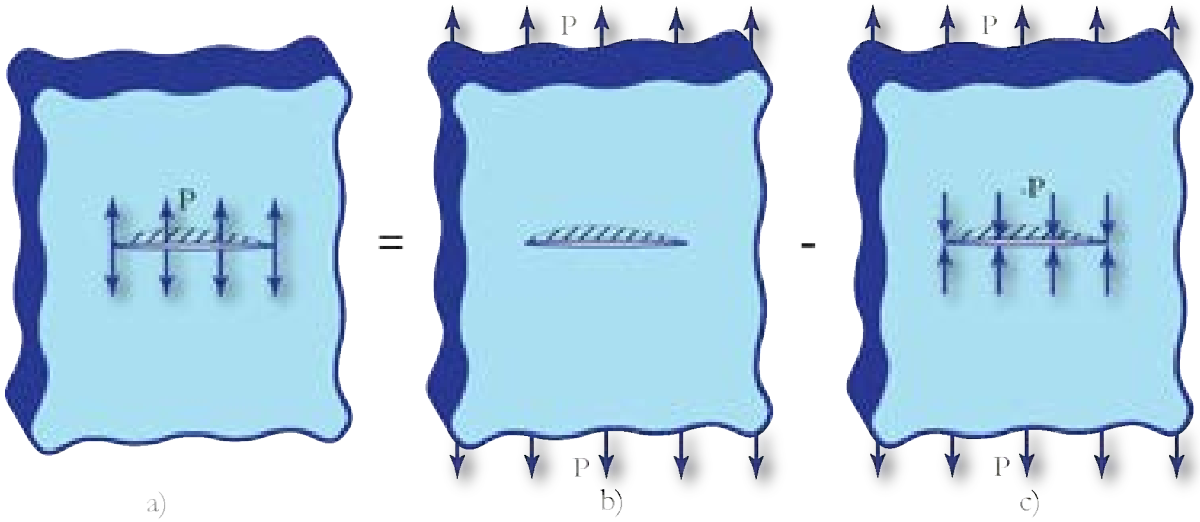

Figure 1.7: Superposition principle

1.3.6 Crack tip plasticity approaches

Simple corrections can be introduced to LEFM approaches when the inelastic region grows around the crack tip and this maintains the elastic stress analysis valid. The size of plasticity zone around crack tip can be estimated by two approaches:

1.3.6.1 Irwin approach

If we consider a linear elastic material with crack in mode I and its orientation $\theta = 0$, the stresses along x and y directions are:

$$\sigma_{xx} = \sigma_{yy} = \frac{K_I}{\sqrt{2\pi a}} \tag{1.12}$$

We assume the normal stress σ_{yy} at the boundary between elastic and plastic zones is equal to the yield stress. That is, $\sigma_{yy} = \sigma_{YS}$ with plane stress conditions. Replacing yield stress σ_{YS} into the left side of equation (1.12), leads to the first-order estimate of plastic zone size given by:

$$r_y = \frac{1}{2\pi}\left(\frac{K_I}{\sigma_{YS}}\right)^2 \tag{1.13}$$

The stress singularity is truncated by yielding at the crack tip and the stress distribution for $r = r_y$ can be replaced by a horizontal line at $\sigma_{yy} = \sigma_{YS}$. The Figure 1.8 illustrates this concept. The previous analysis is limited to case of existence of elastic zone around the crack. In addition, when the stress reaches limit value, the stresses should be redistribute to satisfy equilibrium.

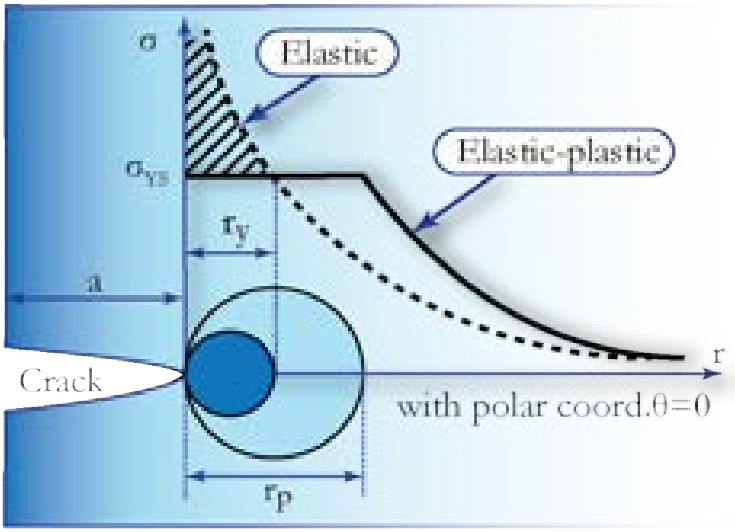

Figure 1.8: First-order and second-order estimates of plastic zone size.

For elastio-plastic materials, the stress can not exceed the limit value; therefore, the elastic energy in the cross-hatched region of Figure 1.8 can be replaced by the increasing in the plastic zone. This fact leads to the second-order estimate of the plastic zone given by:

$$r_p = \frac{1}{\pi}\left(\frac{K_I}{\sigma_{YS}}\right)^2 \tag{1.14}$$

Irwin [25] considered the effect of plastic zone in case of softer material by defining an effective crack length $a_{eff} = a + r_y$ with a is actual crack size and r_y is a plastic zone correction. The effective stress intensity factor K_{eff} can be obtained by inserting a_{eff} into the K expression.

$$K_{eff} = Y(a_{eff})\sigma\sqrt{\pi a_{eff}} \tag{1.15}$$

where Y is the geometry correction factor.

1.3.6.2 Strip yield model

Dugdale [26] and Barenblatt [27] are the first who proposed the strip yield model illustrated in Figure 1.9. The strip yield plastic zone is represented with a crack of length $2a + 2\rho$ in an infinite plate with ρ is the length of the plastic zone and σ_{YS} is a closure stress imposed at each crack tip as shown in Figure 1.8b. The strip yield model is a classical application of the principle of superposition. Using Taylor series, the estimation of the plastic zone size is:

$$\rho = \frac{\pi^2\sigma^2 a}{8\sigma_{YS}^2} \tag{1.16}$$

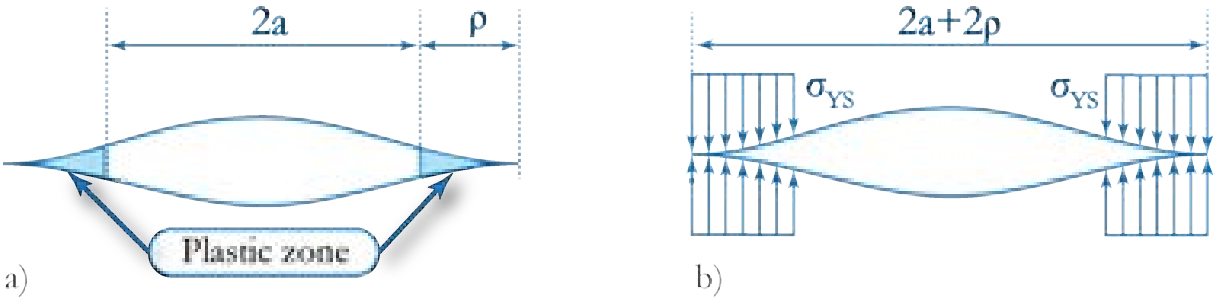

Figure 1.9: Strip yield model: a)plastic zone, b)closure model.

The crack length a can be replaced by the effective length $a_{eff} = a+\rho$ to obtain the effective stress intensity factor as:

$$K_{eff} = \sigma\sqrt{\pi a \quad sec\left(\frac{\pi\sigma}{2\sigma_{YS}}\right)} \tag{1.17}$$

1.3.7 Propagation of an oriented crack

Suppose that an initial crack propagates with a tiny advance inclined by angle θ from the plane of the crack as illustrates the Figure 1.10. The local stress intensity factors at the new

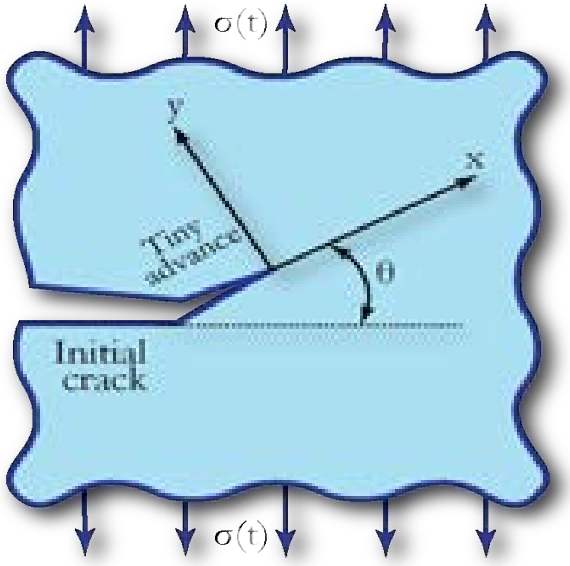

Figure 1.10: Propagation of initial crack tip.

tip are obtained by summing the normal and shear stresses intensity factors as follows:

$$k_I(\theta) = \sigma_{yy}\sqrt{2\pi a} = C_{11}K_I + C_{12}K_{II} \tag{1.18}$$

$$k_{II}(\theta) = \tau_{xy}\sqrt{2\pi a} = C_{21}K_I + C_{22}K_{II} \tag{1.19}$$

where k_I and k_{II} are the stress intensity factors for the actual state of the crack, whereas K_I and K_{II} are the stress intensity factors for the initial crack. The coefficients C_{ij} are:

$$C_{11} = \frac{3}{4}\cos\frac{\theta}{2} + \frac{1}{4}\cos\frac{3\theta}{2} \tag{1.20}$$

$$C_{12} = -\frac{3}{4}[\sin\frac{\theta}{2} + \sin\frac{3\theta}{2}] \tag{1.21}$$

$$C_{21} = \frac{1}{4}[\sin\frac{\theta}{2} + \sin\frac{3\theta}{2}] \tag{1.22}$$

$$C_{22} = \frac{1}{4}\cos\frac{\theta}{2} + \frac{3}{4}\cos\frac{3\theta}{2} \tag{1.23}$$

The energy release rate for the actual state of the crack tip is given by:

$$G(\theta) = \frac{k_I^2(\theta) + k_{II}^2(\theta)}{E} \tag{1.24}$$

the expressions(1.18) and (1.19) illustrate the effect of the crack orientation on its dynamic propagation.

1.4 Elasto-plastic fracture mechanics

Under the theoretical assumptions of linear elastic fracture mechanics, the stress at the crack tip is infinite, this is due to the fact that the plastic zone around the fracture tip is neglected. However, from physical point of view no material can resist to infinite stress. The limit of the plastic zone was considered to correct the concept of the infinite stress near the crack tip. If this zone exceeds its limit, the Elastic-Plastic Fracture Mechanics (EFPM) is needed to explain the observed nonlinear phenomena.

Elastic-plastic fracture mechanics deals with ductile materials that have nonlinear behavior. To analyze this last, two elastic–plastic parameters will be described in this section: the crack tip opening displacement $CTOD$ and the J contour integral. As fracture criteria, both parameters might be used even for relatively large plasticity near the crack tip. The critical values of $CTOD$ and J provide practically size-independent indices of fracture toughness.

1.4.1 Crack tip opening displacement

Wells [22] During his research, noticed whenever the material has higher toughness, the plastic deformation blunted more the sharpness crack tip, as illustrated in Figure 1.11. Wells

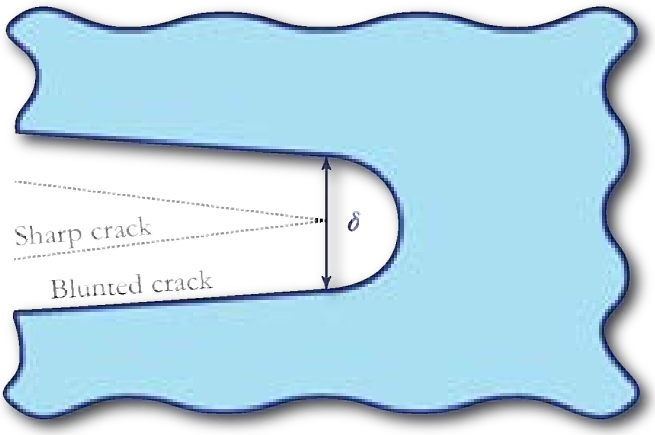

Figure 1.11: Blunting of an initial sharp crack and *CTOD*.

used this discovery to propose the *CTOD* as a measurement of the fracture toughness. Irwin announced in [25] that the crack tip plasticity zone makes the crack behave as if it is slightly longer. This fact is illustrated in Figure 1.12. Based on Irwin results, Wells performed in

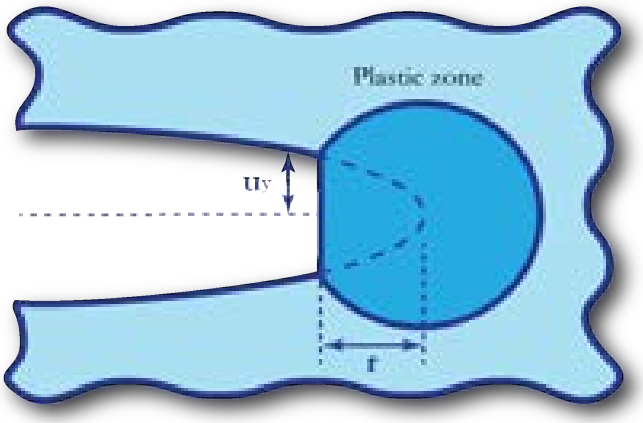

Figure 1.12: Irwin plastic zone correction and *CTOD*.

[22] an approximate analysis that related *CTOD* to the stress intensity factor in the limit of small-scale yielding. This approximated relationship is given by the following expression:

$$\delta = 2u_y = \frac{4}{\pi}\frac{K_I^2}{\sigma_{YS}E} \tag{1.25}$$

Where δ is the *CTOD* displacement.
The other expression that can relate the *CTOD* with the energy release rate is:

$$\delta = \frac{4}{\pi}\frac{G}{\sigma_{YS}} \tag{1.26}$$

The general relation can be expressed as follows:

$$\delta = \frac{K_I^2}{m\sigma_{YS}E'} = \frac{G}{m\sigma_{YS}} \tag{1.27}$$

With $m = 1.0, E' = E$ for plane stress and $m = 2.0, E' = \frac{E}{1-v^2}$ for plane strain.

1.4.2 J-Integral

Characterizing the fracture in nonlinear elastic materials by using a path-independent integral was done for the first time and named J-integral by Rice in [29, 32]. The concept of J-integral is established for nonlinear elastic materials with plastic deformation and load in one unique direction. Rice discovered that a specific J-integral, along a closed path for any nonlinear elastic, planar, homogeneous, and isotropic material in a condition of static equilibrium is always equal to 0. For crack without any body force and tensile force on crack lips ($f^b = f^c = 0$) is illustrated in Figure 1.13a. The two-dimensional form of one of these integrals can be written as:

$$J = \oint_\Gamma \left(w_s dy - t\frac{\partial u}{\partial x} \right) d\Gamma \tag{1.28}$$

in index notation :

$$J = \oint_\Gamma \left(w_s \delta_{1j} - \sigma_{ij}\frac{\partial u_i}{\partial x} \right) n_j \, d\Gamma \tag{1.29}$$

with

$$w_s = \frac{1}{2}\sigma_{ij}\varepsilon_{ij} \tag{1.30}$$

Where Γ is a closed path contour, w_s the strain energy density, $t = \sigma n$ the traction vector on a plane indicated by the outer normal n, and u is the displacement vector. The J-integral

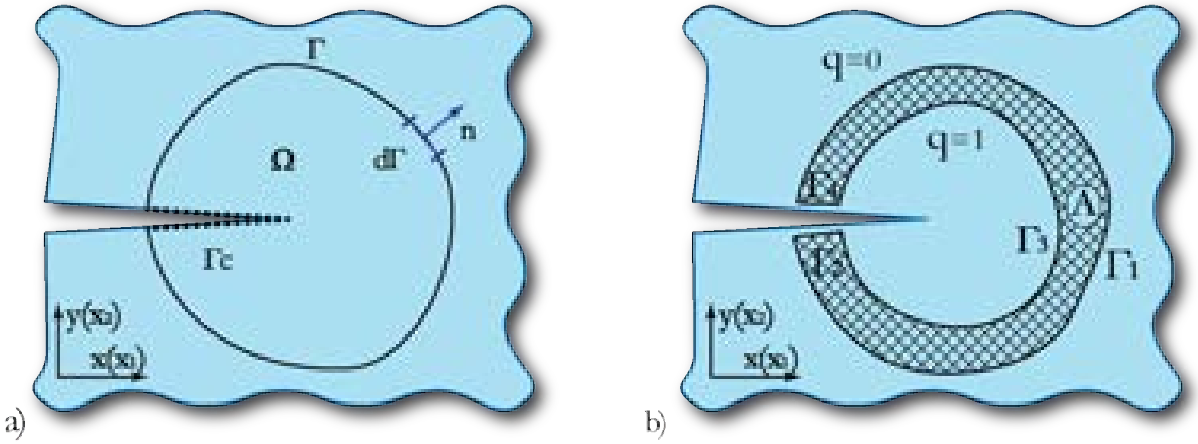

Figure 1.13: Concepts of J-integral path: a)linear path, b)equivalent domain.

has the independency feature. That is, the J contour starts at one crack surface and finishes at the other. The J-integral can be calculated regardless of the path. The size and shape of the contour curve for a given problem is determined by the crack geometry and the type of chosen finite element. This fact will be further explained in the next sections.

1.4.2.1 Equivalent domain integral method

The equivalent domain integral method was suggested by Li et al. [39] as an alternative to the original contour J- integral. According to the concept of equivalent domain, illustrated in Figure 1.13b, the J-integral can be redefined as:

$$J = \int_A \left(\sigma_{ij} \frac{\partial u_i}{\partial x_1} - w_s \delta_{1j} \right) \frac{\partial q}{\partial x_j} dA \tag{1.31}$$

where q is an arbitrary smoothing function equal to unity on Γ_3 and zero on the boundary of the J-domain Γ_1. The finite element method is an appropriate technique for a such approach. Indeed, we need just to replace the contour integral by an equivalent area integral.

1.4.2.2 Interaction integral method

Auxiliary fields are superimposed with the actual fields in the interaction integral approach to solve the boundary value problem [40]. The auxiliary state stresses and strains should satisfy the equilibrium equation as well as the traction-free boundary condition on the crack surface in the A area shown in Figure 1.13b. In order to identify a relationship between the mixed-mode stress intensity and the interaction integrals, these auxiliary fields should be carefully chosen.

For the total of the actual and auxiliary states, the contour of J-integral can be written as:

$$J = J^a ct + J^a ux + M \tag{1.32}$$

Where J^{act} and J^{aux} are, respectively, the J-integral actual and auxiliary states. M is the interaction integral. The expressions of the aforementioned parameters are:

$$J^{act} = \int_A \left(\sigma_{ij} \frac{\partial u_i}{\partial x_1} - w_s \delta_{1j} \right) \frac{\partial q}{\partial x_j} dA \tag{1.33}$$

$$J^{aux} = \int_A \left(\sigma_{ij}^{aux} \frac{\partial u_i^{aux}}{\partial x_1} - w^{aux} \delta_{1j} \right) \frac{\partial q}{\partial x_j} dA \tag{1.34}$$

$$M = \int_A \left(\sigma_{ij} \frac{\partial u_i^{aux}}{\partial x_1} + \sigma_{ij}^{aux} \frac{\partial u_i}{\partial x_1} - w^M \delta_{1j} \right) \frac{\partial q}{\partial x_j} dA \tag{1.35}$$

The strain energy density for the actual, auxiliary and interaction are given by:

$$w_s = \frac{1}{2}\sigma_{ij}\varepsilon_{ij} \tag{1.36}$$

$$w^{aux} = \frac{1}{2}\sigma_{ij}^{aux}\varepsilon_{ij}^{aux} \tag{1.37}$$

$$w^{M} = \frac{1}{2}(\sigma_{ij}^{aux}\varepsilon_{ij} + \sigma_{ij}^{aux}\varepsilon_{ij}) \tag{1.38}$$

1.4.2.3 Effect of crack surface traction

In case of applied tensile force on crack surface as illustared in Figure 1.14. To introduce the effect of the tensile force to the concept of J-integral, Karlsson et al. [41] developed the following equation:

$$J = \int_{\Gamma}\left(W_s dy - t\frac{\partial u}{\partial x}d\Gamma\right) - \int_{\Gamma_c} f^c \frac{\partial u}{\partial x}d\Gamma \tag{1.39}$$

where Γ_c is the crack surface limited by the two ends of the path Γ. f_c is the traction vector applied to the crack surface as illustrated in Figure 1.14.

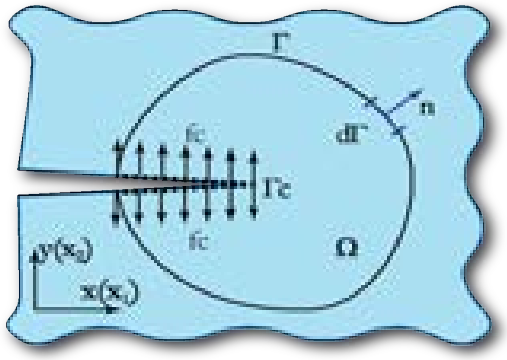

Figure 1.14: Surface crack under traction.

1.4.2.4 Generalization of J-Integral

The generalized J-Integral for modes I and II developed by Hellen et al. [42] is:

$$J = J_1 + iJ_2 = \frac{1}{E'}(K_I^2 + K_I I^2 + 2iK_I K_I) \tag{1.40}$$

where the components J_1 and J_2 corresponding to modes I and II, are given by the following formula:

$$J_1 = \int_{\Gamma}\left(w_s dy - t\frac{\partial u}{\partial x}\right)d\Gamma \tag{1.41}$$

$$J_2 = \int_{\Gamma}\left(w_s dx - t\frac{\partial u}{\partial y}\right)d\Gamma \tag{1.42}$$

1.4.3 Relationship between J and K

One of the choices for the auxiliary state is the displacement and stress fields in the vicinity of the crack tip. The expression that relate the J-integral and stress intensity factors is:

$$J = \frac{1}{E'}(K_I^2 + K_I I^2) \tag{1.43}$$

and M is expressed as:

$$M = \frac{2}{E'}(K_I K_I^{aux} + K_{II} K_{II}^{aux}) \tag{1.44}$$

As a consequence, the stress intensity factors can be calculated using the following formula:

$$K = \frac{E'}{2} M = (K_I K_I^{aux} + K_{II} K_{II}^{aux}) \tag{1.45}$$

where $K_I^{aux} = 1$, $K_{II}^{aux} = 0$ for mode I and $K_I^{aux} = 0$, $K_{II}^{aux} = 1$ for mode II.

1.4.4 Relationship between J and $CTOD$

Figure 1.15 depicts the various displacement components around the crack tip region according to the $CTOD$ definition of Tracy et al. [43]. The crack opening at the intersections of two

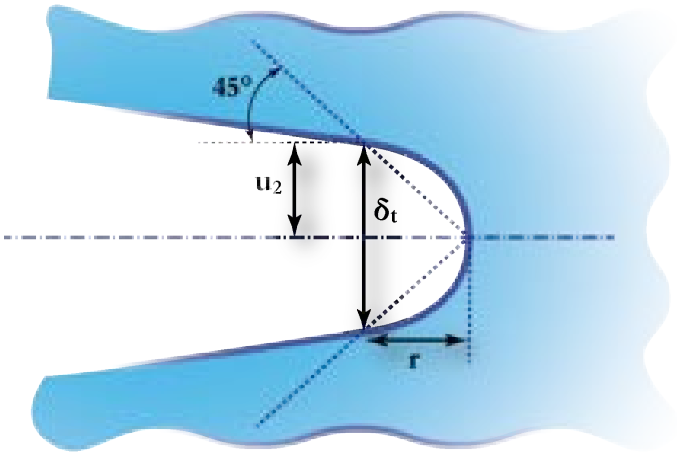

Figure 1.15: Displacement components in $CTOD$.

symmetric lines from the deformed crack tip and the crack shape as illustrated in Figure 1.15 and is known as the crack opening diameterδ_t. Using the crack tip fields, the displacement component u_2 along the crack shape is defined as follows:

$$u_2 = \alpha\varepsilon_0 \left(\frac{J}{\alpha\varepsilon_0\sigma_0 I_m}\right)^{\frac{m}{m+1}} r^{\frac{1}{1+m}} \hat{u}(\pi) \tag{1.46}$$

Using the above relationships, Shih [44] was established the following general relationship between the J-integral and *CTOD*:

$$\delta_t = d_m \frac{J}{\sigma_0} \tag{1.47}$$

where d_m is a constant that depends on m value in the two cases of plane stress or plane strain. The values of d_m for various values of m were obtained from the finite element study [44] summarized in Figure 1.16.

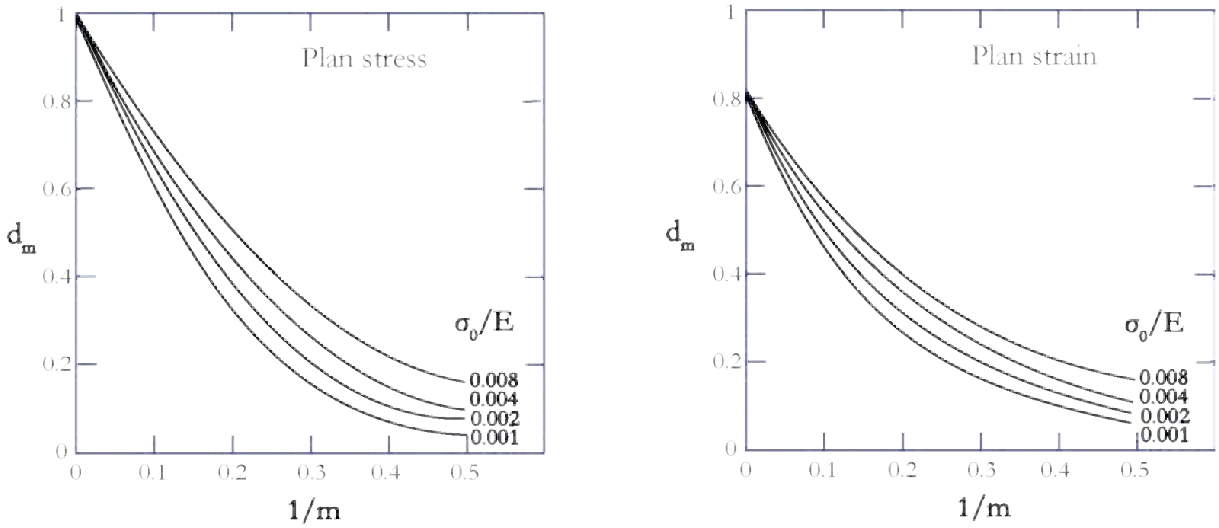

Figure 1.16: Relation of d_m on $1/m$ for: a)plane stress, b)plane strain.

1.5 Dynamic and time-dependent fracture

Time is a crucial variable in certain fracture problems. For example, instationary thermal loading, fatigue and quick dynamic loading, inertia effects and creep deformation. Unfortunately, Linear elastic and elastic–plastic approaches are ineffective in such cases. Despite the fact that many researchers were included the dynamic impacts in their studies but the proposed solution still limited to isolated and special situations. The most recent and effective time-dependent fracture approaches are based mainly on J-integral generalizations.

Dynamic fractures are more complex than static ones, due to the fact that we deal with motion equation rather than simple equilibrium. The dynamic fracture mechanics is characterized by three features: inertia forces, rate-dependent material behavior and reflected stress waves. When the load varies sharply or the crack grows rapidly, inertia effects are significant and a portion of the load is turned into kinetic energy.

The rapid load in rate-sensitive materials such as polymers, produces stress waves that propagate into the material and reflect on their boundary. These waves and their reflections influence the local crack tip stress and strain fields, and hence affect the fracture behavior. One of the disciplines of dynamic fracture is the elastodynamic fracture mechanics, that dedicated to studying the crack's behavior under dynamic loading using LEFM concepts. In this discipline, the effect of inertia forces and reflected stress waves are taken into consideration. In the other hand, it ignore the plastic zone effect when it is still confined around the crack tip. Research studies such as [45, 46, 47, 48, 49, 50, 51] are typical examples from this discipline. Recently, many researches [52, 53, 54, 55, 56, 57] extended and enhanced the concept of J-integral to take into account inertia effect and viscoplasticity behavior of materials . It is clearly shown from the literature, that the dynamic fracture problems are divided into two categories: crack initiation and rapid crack propagation. From the behavioral side, the crack under quasi-static (fatigue) or rapid dynamic load has three possible behaviors; initiation, propagation and crack arrest. The rest of this chapter is dedicated to the characterization of these behaviours.

1.5.1 Dynamic stress intensity factors for stationary and dynamic cracks

Dynamic load has many forms, one of them is the fast or rapid dynamic. As example, the impact or explosive loading. To analyze the effect of this type of loading on the crack behavior, many experiments were done such as the most popular dynamic mechanical test known as the Charpy's test [58], in which a pendulum dropped from a given height on a specimen initially cracked. This type of load can take many curves during the time as shown in Figure 1.17. To compute the maximum hoop stress intensity factor and analyze dynamic fracture

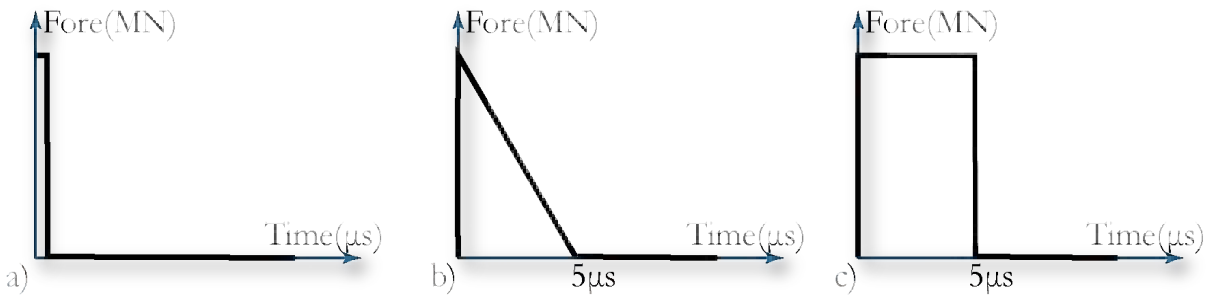

Figure 1.17: Some types of rapid dynamic load.

propagation properties, dynamic stress intensity factors are used. Freund [54] calculated an

accurate dynamic stress intensity factors for a stationary crack subject to normal and shear incidence plane stress pulses with magnitudes of σ_0 and τ_0, as described by the equation bellow:

$$K_I(0,t) = \frac{2\sigma_0}{1-\nu}\sqrt{\frac{c_l t(1-2\nu)}{\pi}} \tag{1.48}$$

$$K_{II}(0,t) = 2\tau_0\sqrt{\frac{c_s t}{\pi(1-\nu)}} \tag{1.49}$$

Where c_l and c_s are the longitudinal and shear wave speeds of the material. ν is the Poisson's ratio. For the moving crack-tip (propagation case), the formula of dynamic stress intensity factors [54] are:

$$K_I(v_c,t) = f_I^d(v_c)K_I(0,t) \tag{1.50}$$

$$K_{II}(v_c,t) = f_{II}^d(v_c)K_{II}(0,t) \tag{1.51}$$

with f_I^d and f_{II}^d are functions of the propagation velocity of crack v_c. Their approximated expressions for an isotropic material are given by:

$$f_I^d(v_c) = \frac{1-v_c/c_R}{\sqrt{1-v_c/c_l}} \tag{1.52}$$

$$f_{II}^d(v_c) = \frac{1-v_c/c_R}{\sqrt{1-v_c/c_s}} \tag{1.53}$$

with c_R the Rayleigh wave speed.

1.5.2 Dynamic fracture criteria

Based on the tested material type, the dynamic propagation criterion is defined. Mainly, this criterion should describe, for one hand, the stability state of the crack, and on the other hand, if the crack is unstable it should predict the direction and the velocity of the crack [59]. Therefore, the stability state is defined by the comparison of the current stress intensity factor with the dynamic crack initiation toughness K_{Ic}^d which is an intrinsic property of a material. If the current stress intensity factor is greater than dynamic crack initiation toughness, the crack propagates according to the direction of propagation determined by a given criterion such as the maximum hoop stress [60]. The crack propagation speed vary in such manner that the maximum hoop stress intensity factor equals the dynamic crack growth toughness. In this context, the criterion of dynamic crack growth is [59, 60, 61, 62]:

$$K_{tt} < K_{Ic}^d \tag{1.54}$$

$$K_{tt}(t,0) = K_{Ic}^{d} \tag{1.55}$$

$$K_{tt}(t,v_c) = K_{Ic}^{D}(v_c) >= K_{Ic}^{d} \tag{1.56}$$

where K_{tt} is the dynamic maximum hoop stress intensity factor, K_{Ic}^{d} the dynamic crack initiation toughness and K_{Ic}^{D} the dynamic crack growth toughness.

$$K_{Ic}^{D}(v_c) = \frac{K_{Ic}^{d}}{(1 - v_c/c_R)} \tag{1.57}$$

The propagation velocity v_c is:

$$v_c = c_R \left(1 - \frac{K_{Ic}^{d}}{K_{tt}}\right) \tag{1.58}$$

The propagation angle is defined when the strain energy density is at its minimum value.

1.6 Fatigue crack growth

Fatigue crack growth occurs as a result of repetitive cycle loading at stress levels much below those that would normally induce failure. Fatigue is defined by a differential equation that expresses the rate of crack growth as a function of material attributes and the stress intensity factor. A sudden, catastrophic collapse can be caused by fatigue fracture. This last is induced by repeated cyclic loading much below the material's yield stress. The applied stress is related to the number of cycles to failure and can typically given by the S-N curve. As example we can mention the Wohler S-N curve given by Figure 1.18. For a fatigue failure, once a small

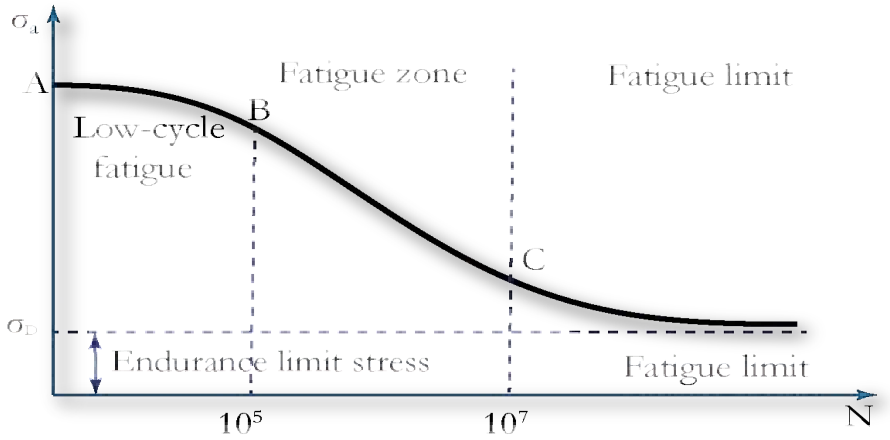

Figure 1.18: Example of Wohler S-N curve.

crack has formed it grows very slowly, even on nano-scale from cycle to cycle. The crack grows over time until the crack reaches a critical length a_c to attain the sudden collapse.

Fatigue crack growth is generally simulated by empirical models and fitting the results using the following function.

$$\frac{da}{dN} = f(\Delta K) \tag{1.59}$$

where da/dN is the crack growth rate and ΔK is the stress intensity factor range given by:

$$\Delta K = K_{max} - K_{min} \tag{1.60}$$

with K_{max} and K_{min} are the stress intensity factors, respectively, at the maximum and minimum stress values for each loading cycle.

Among these models, there is the classical Paris model [63] expressed as:

$$\frac{da}{dN} = C\Delta K^m \tag{1.61}$$

with C the Paris model constant and m the Paris model exponent that depend on material properties and loading conditions. The only information needed to calculate the increment of growth da is the stress intensity factor range ΔK_i for the current crack geometry. The growth increment in each cycle Δa_i is given by:

$$\Delta a_i = \Delta N[C(\Delta K_i)^m] \tag{1.62}$$

This estimated growth increment Δa_i has an orientation angle that need to be calculated. This angle is key element for the prediction of the crack behaviour and to anticipate its propagation hence to avoid the catastrophe. Many methods tend to give this angle, such as the maximum strain energy density criterion[64], the critical plane approach[65], the maximum energy release rate[66], and the maximum circumferential stress[67, 68]. The last criterion is the most used for modeling the crack growth with finite elements and, hence, estimating better the growth direction θ by:

$$\theta = -\arccos\left(\frac{2K_{II}^2 + K_I\sqrt{K_I^2 + 8K_{II}^2}}{K_I^2 + 9K_{II}^2}\right) \tag{1.63}$$

Another equivalent formulas are developed in [69, 70] and given by:

$$\theta = 2\arctan\left(\frac{-2(K_{II}/K_I)}{1 + \sqrt{1 + 8(K_{II}/K_I)^2}}\right) \tag{1.64}$$

$$\theta = 2\arctan\left[\frac{1}{4}\left(\frac{K_{II}}{K_I} - sign(K_{II}\sqrt{\left(\frac{K_I}{K_{II}}\right)^2 + 8}\right)\right] \tag{1.65}$$

The expressions (1.63), (1.64) and (1.65) demonstrate the crucial role of the crack orientation in the fatigue propagation.

1.7 Conclusion

In this chapter, we offered to the reader a brief historical review on the fracture mechanics. We described, after that, the three mean disciplines of the fracture mechanics related to the type of the material behaviors (linear elastic, elasto-plastic, dynamic). We focused our attention on the most important parameters of each discipline and theirs relation with geometric parameters of the crack. A particular attention is given to the crack orientation angle that play a crucial role in the crack behaviour analysis. Indeed, the accurate detection of this angle helps on anticipating the crack behaviour and prevent the catastrophe as soon as possible. From this angle of view, our contributions in this manuscript are dealing with this objective. Indeed, the next chapter, will be devoted to non destructive testing techniques that serve, after, as tools for accurate estimation of the crack orientation.

Chapter 2

Non-destructive testing

2.1 Introduction

Before offering a product to the consumer, there are two methods to check that the final product meets the standards: The destructive method that render the product useless after testing and the non destructive method.
The Non-Destructive Testing (NDT) is a method of analyzing the changes in a system's characteristics without harming it or stopping its functionality. The NDT is used, practically, in all industries. However, its major application remains in petrochemical, pipeline, aerospace, power generation, automotive, rail, civil structures, transport infrastructure (bridge, tunnel, airports) and in medical devices. NDT includes a large variety of technique from a wide range of disciplines.
Many efforts are deployed over years to discuss certain norms that have been created to ensure the reliability of NDT tests and to minimize possible mistakes. The objective is to reduce to the minimum the effect of equipment's deficiencies, wrong use of procedures and incompetence of the expertise. As a result, an effective NDT leads to the adequate identification of faults and the accurate analysis of material properties.
After we introduced the crack problem in the previous chapter, we discuss in this chapter the selected NDT method for the resolution. Indeed, in our case some tools are borrowed from the NDT domain to analyze the crack behaviour. To this end, this chapter is structured as follows: it begins with a historical review of the existing NDT techniques. It allows mastering the necessary NDT background and provides a better understanding of this domain. Following that, we'll go through a description of the most prevalent NDT techniques, including their benefits and drawbacks, as well as their application domains. Lastly, we highlight in

details the chosen method to solve the proposed problem and give the reason for selecting such a method.

2.2 Historical review

Although there is no definite beginning date for NDT, it has been used for many years. During the Roman era, wheat and oil were supposed to be employed to locate fractures in marble slabs. For centuries, blacksmiths utilized sonic NDT to listen to the ring of various metals while they were hammered into shape; an early bell maker also used this approach [71].

Before going into detail about the history of NDT methods, it's important to remind the definition of an NDT method, which is the use of physical phenomena for passive testing of a product or substance. With this broad concept of NDT in mind, visual testing is by far the most ancient NDT approach, dating back to the visual inspection of blades for cutting meat and spears for hunting [72].

Acoustics is the second-oldest approach, having been utilized for testing since man began to build the first ceramic vessels in ancient times. The first documented ceramic jars were probably created by people in China some 20,000 years ago [73]. The acoustics were very certainly employed for glassware testing much later. During the middle ages, the same procedure was used to test brass castings, such as a massive church bell. However, this was only a test with an audible sound.

Magnetic flux testing of rifle barrels is the third oldest traditional procedure. Magnetism was first discovered by Thales of Miletus, according to Aristotle, and was used for compasses in the middle ages. In 1868, Englishman S.H. Saxby used the magnetic properties of a compass to identify cracks in cannon barrels, which was one of the first known uses of NDT [71]. This technique of inspection was among the most efficient procedures for obtaining a realistic and quick results in oil and gas industries [74, 75].

Although the origins of modern non-destructive testing and Non-Destructive Evaluation (NDE) date back before the 1920s. Magnetic particle testing and radiographic testing were well-known at that period, particularly in the medical industry [71].

W.E.Hooke, operating for quality gage blocks at the American Bureau of Standards, created a method for magnetizing an object, producing a leakage field, and using iron powder to detect cracks unseen to the human eye. This invention was patented in the United States in 1922 [71, 76].

The first traditional NDT approach was the radiographic testing before the discovery of the magnetic testing. After discovering X-rays in 1896, Professor Wilhelm Conrad Roentgen took a radiograph of four soldered pieces of zinc and one of his personal hunting guns. The rifle's radiograph identified minor cast faults in the metal, marking the beginning of the industrial radiography [77, 71].

A procedure known as the "oil and whiting test" was employed in the early days of the railroad to prepare the surface and named today's by Penetrant Test (PT). In 1948, F. B. Duane was obtained a patent for his luminous penetrant method [78]. At the turn of the twentieth century, this approach was employed to test the massive cast elements of enormous trains. They utilized a black pigmented oil that contained dirt and whiting. It was basically a water-based chalk-slurry that dried to a white coating served as developer [71].

The foundation for ultrasonic testing was laid in 1940, when F.A. Firestone received a license for his flaw detection device design. Then, in 1942, Firestone became the first person to employ his sonar approach [79]. Two physicists brothers Herbert and Josef Krautkrämer, who had studied Firestone's publications and made significant contributions to the development of the ultrasonic method [80]. Since then, the approach has gone through various stages of development and has achieved huge success, and it still has a lot of capacity for more applications.

Eddy Current Testing (ECT) is another traditional procedure. At the turn of the twentieth century, this strategy was mainly developed in the United States. Although were some practical applications of the ECT, even there was no working theory behind the process. Then, in the 1950s, it was the German F. Foerster who formalized the ECT theory and established the essential formulas [81, 82]. The ECT is now widely used in various domains for production testing for example in austenitic tubes and in-service testing of heat exchanger tubes.

2.3 Types of nondestructive testing techniques

During the second world war, the application of NDT procedures made a breakthrough, beginning with submarine and airplane testing. Over the last fifty years, the examination of nuclear power plant equipment, pressure vessels, bridges, elevators, and car parts. is done mainly by NDT techniques [71].

2.3.1 Visual and optical inspection

One of the most old and common non-destructive evaluation procedures is the visual inspection. It was usually considered subjective inspection due to many factors such as the purity of the tested specimens, the illumination level, the operators skills and the optical equipment's quality. Indeed, efficient visual examination should be ensured by acceptable physical standards to inspecting surface flaws and performing various measurements. To increase the test quality, many devices should be add to the main optical instrument like, spectrometers, real-time photography, particular sensors and computer processing. A visual inspection is a useful tool, whether it is assisted or unassisted, direct or indirect, to identify flaws locations in large areas. Once located the flaws, other NDT techniques can be used to deal with the flaws. In the case of corrosion, the visual examination gives significant information about its severity and the remains lifetime of the tested structure. These information are collected through the color of the corroded zones. Although, the visual inspections cannot be utilized to verify test results or to replace other evaluation techniques[83]. The equipment used for this kind of inspection are illustrated in Figure 2.1.

Figure 2.1: Equipment for visual testing: a)magnifying glasses, b)phoropter, c)pipe inspection robot, d)metallurgical microscope, e)endoscope, f)scanning-electron-microscope.

To justify the choice of a such technique, we can list the following benefits of this NDT:

- Affordable, i.e. the cheapest available NDT.
- Ensures detection while avoiding of potential discontinuities in the case of welding process.
- Provides for the spotting of discontinuity zones in large tested areas.
- Simple to practice.
- Portable and can used for difficult and tight zones unreachable by other equipment.
- Needs less pre-processing for the tested area and the equipment.

In the other hand, the following are some of the limits and drawbacks of this technique:

- Inspection only for surface flaws.
- Possibility of misdiagnosis.
- Inability to operate in small scale.

2.3.2 Liquid penetrant testing

The liquid penetrant inspection technique is the operation of checking material surface flaws by pouring a very thin liquid into the flaw and then pulling the liquid out with a chalk-like developer. Commonly used for any type of structures like plates, bars, pipelines, castings, forgings and especially for wielding zones. The liquid penetrant examination has been referred to by a variety of names over the years, including dye penetrant testing, penetrant testing and liquid penetrant testing. Among the most frequently applied nondestructive evaluation techniques is liquid penetrant inspection due to two key aspects: its relative simplicity and versatility [84].
The surfaces to be examined must be clean from any coverings, paint, grease, dirt, or dust. During the cleaning process, extra caution should be exercised to avoid causing more damage to the surface subject to examination. With additional interference of the surface features, generated during the cleaning process, the original nature of the surface could be affected and, thus, the results become incorrect. The operation steps depicted in Figure 2.2 are summarized as follows:

1. Clean carefully the tested area and let it dry (Figure 2.2a).

2. Apply the liquid penetrant spray (usually has red color) to the cleaned area and rub it for better penetration and wait about 20 minutes (Figure 2.2b).

3. Clean and erase any leftover remains on the surface with a remover spray/clean textile and dry it for few minutes (Figure 2.2c).

4. Spray, from a distance of 30cm, the area with the developer spray. The developer liquid will drain the penetrant liquid that has infiltrated the surface flaws and react with it to produce clearly the geometric shape of the surface flaws (Figure 2.2d) .

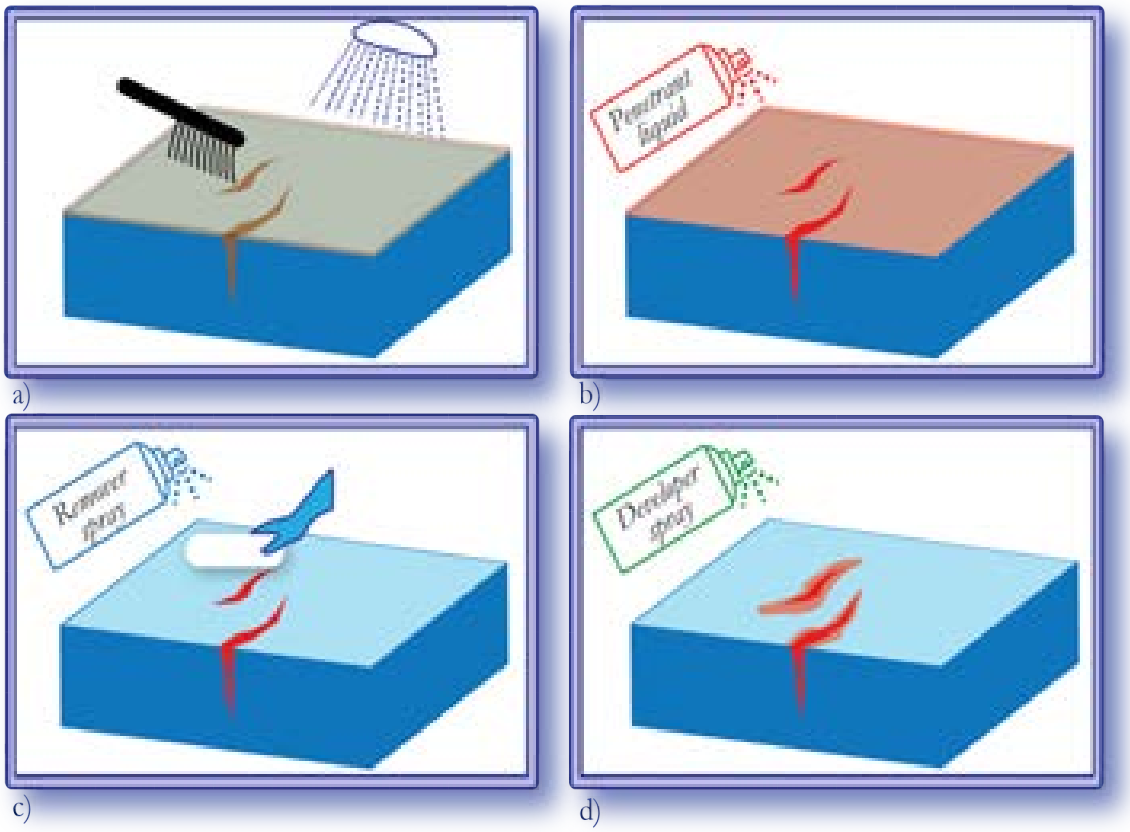

Figure 2.2: Liquid penetrant procedure: a)cleaning the surface, b)applying the penetrant spray, c)cleaning the remains penetrant liquid, d)applying the developer spray.

The advantages of this technique are:

- Inexpensive technique.
- Appropriate, quick and effective for large areas.

- Useful for large variety of materials (metallic, nonmetallic, conductive, non-conductive, magnetic, nonmagnetic)
- Easy to use for structures with complex geometry .
- Simple to practice.
- Few equipment can be carried to any work site.
- Excellent sensitivity to minor surface flaws and cracks.
- Direct indication of position and shape of the flaws.

and the disadvantages of this technique are:

- Can not examine the inside surfaces.
- Can not examine porous surfaces.
- Without sufficient airflow, vapors can be harmful and burning.
- Detects only flaws open to the surface.

2.3.2.1 Magnetic particle testing

In this technique we apply magnetic fields on tiny ferromagnetic particles, to detect surface flaws. The inspected material should have, of course, a ferromagnetic properties to interact with the applied magnetic fields. An magnetic bracket is put on the surface of the specimen to be inspected, a kerosene-iron filling mixture is sprayed over the surface and the electromagnetic field will be disrupted if there is any flaw or any discontinuity on the surface. A new magnetic pole will appear at the end of the discontinuity allowing the detection of the flaw.
Magnetic particle examination is based on the fact that this concentration of particles around the flaws makes it more clear for inspection and identification. For best effectiveness of the technique, the magnetic bracket should be perpendicular to the defect [85]. The magnetic powder is used in this experiment to create the sufficient magnetic field at the investigated location and a powerful U-shaped magnet will be employed.
As shown in Figure 2.3, the technique includes the following stages:

1. Polishing the inspected surface by a sheet of cloth.

2. Spraying the fluorescent magnetic powder on the surface.
3. Applying a magnetic field on the surface using a powerful magnet.
4. Examination, under UV light, of the places where the fluorescent magnetic particles are gathered.

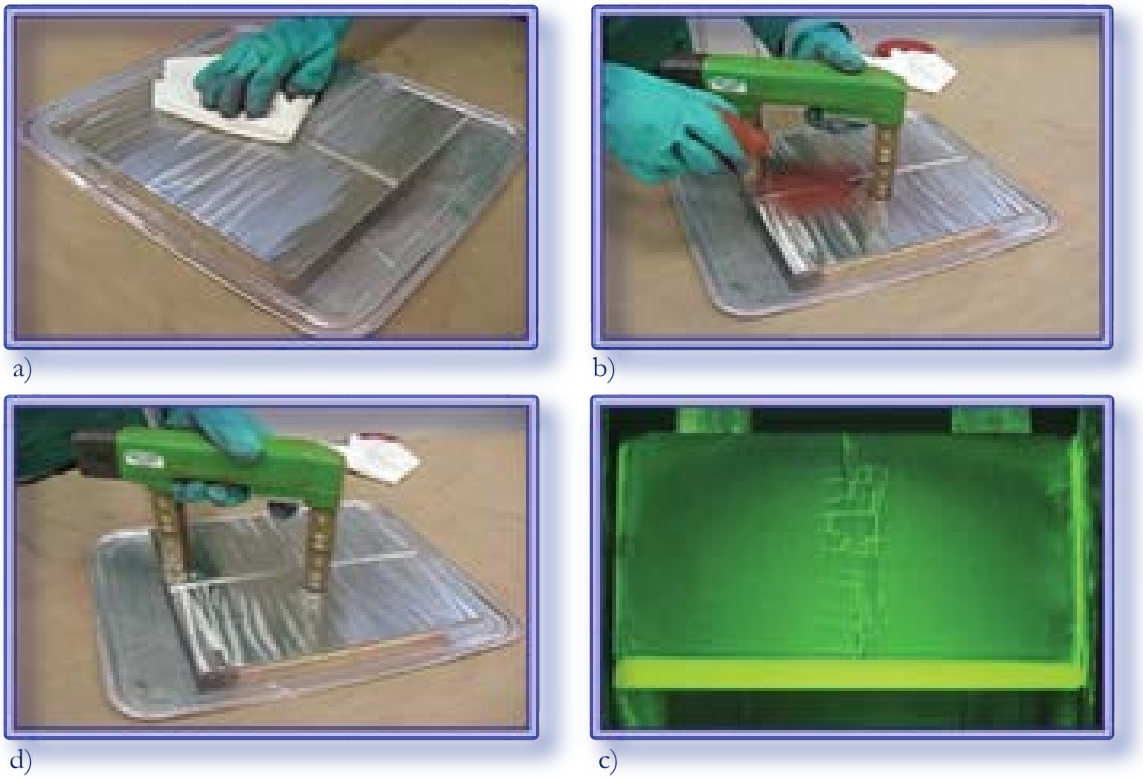

Figure 2.3: Magnetic particle testing: a)cleaning the surface, b)applying the ferromagnetic powder, c)applying a magnetic flux, d)investigation under UV light.

The Magnetic particle technique has the following advantages:

- Simple and quick.
- Relatively inexpensive.
- Portability, the technique may be used in sites or in workshops.
- Ease of inspection for irregular or complex shape of surfaces.
- Ease of use regardless of the surface size.

- Instantaneous indication of flaws.

In the other side, it has the following cons:

- Effective only on open flaws.
- Ineffective in presence of a heavy paint layer on the surface.
- Used only on ferromagnetic materials.
- Demagnetization needed in some cases.
- Professional inspector is needed to avoid fake or irrelevant signs.

2.3.3 Radiography testing

Radiography Testing (RT) is one of these methods that can give information about the interior soundness of the spacemen. Radiography is the process of emitting Gamma ray or x-ray to penetrate inside the inspected metallic component. If the component being radiographed has flaws, more x-rays will flow through the flaws and the film under the component intercept more rays from the flaws as depicted in Figure 2.4.

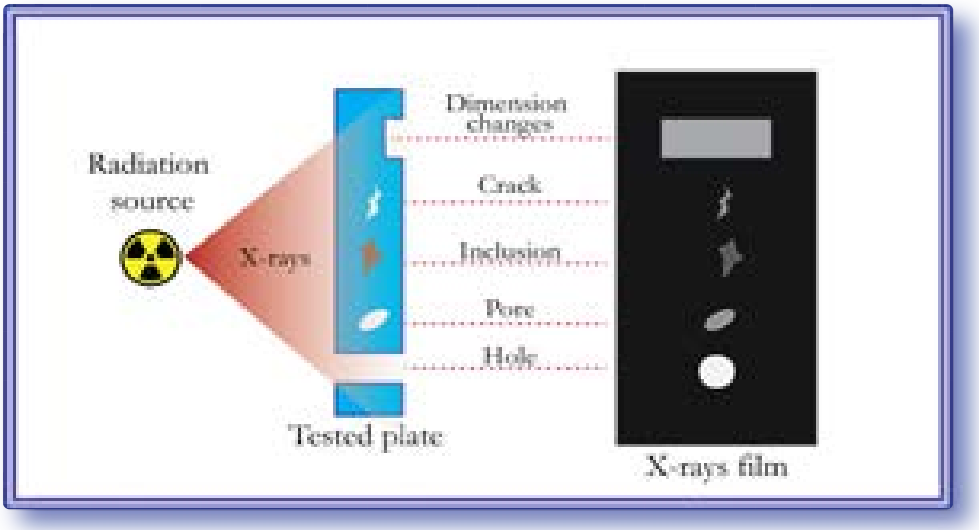

Figure 2.4: Radiographic testing

The sensitivity of x-rays is nominally 2% of the material thickness; therefore as example, the smallest flaw that could be inspected in a component with a thickness of 25mm is 0.5mm

[86]. As a consequence, the components are generally radiographed in many planes, because a thin fault will not be seen until the x-rays are taken parallel to the crack's surface. This technique is effective in many domains; however, due to the danger of dealing with radioactive substances, this technique become less common.

One of the most important industries that remains using this technique is the pipeline welding. It used to detect many type of flaws and avoid catastrophic problems. Figure 2.5 illustrates possible flaws can be detected by this tech like longitudinal and transversal crack appearing in the radiographic image as crooked line with light color. The inclusions of Slag (nonmetallic substance) appears like black rough of irregular forms while the porosity appears as dark round dots and the lack of penetration appears as a dark straight line.

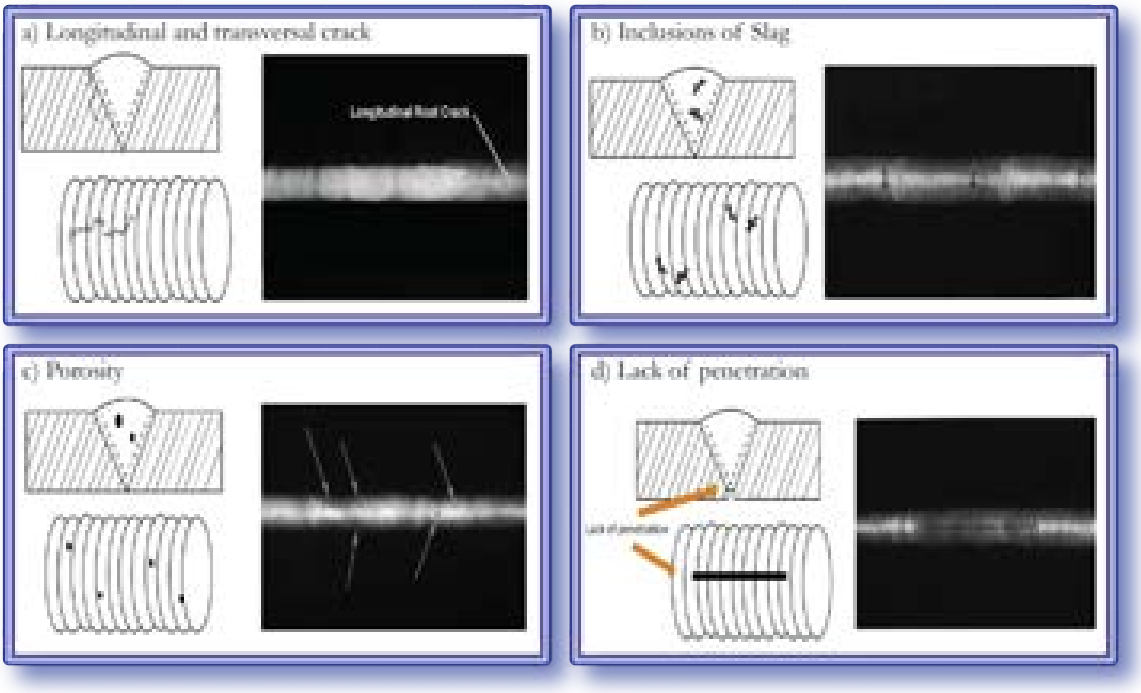

Figure 2.5: Flaws inspected by radiographic testing.

The main pros of radiographic testing are

- Possibility to record the results of inspection as images files.
- Minimal requirement for surface preparation .
- Detect all geometric parameters of flaw (position, size and shape).
- Surface and internal flaws can be inspected.

- Examination of complexes and assembled components is simple.
- High portability.
- Wide range of materials can be inspect by this technique.

The disadvantages of radiographic testing are:

- Harmful exposure to radiation.
- Necessity of high level knowledge and experience.
- Need of expensive devices.
- Inaccessibility to both sides of the component.
- Slow procedure of inspection.

2.3.4 Ultrasonic testing

Ultrasonic Testing (UT) is a non destructive technique that applies a high-frequency sound wave on the tested material to detect flaws or to evaluate many geometric characteristics based on the reflected waves.
The UT inspection system includes many equipments such as the pulser/receiver, the transducer and the display device shown in Figure 2.6. The pulser/receiver produces a high voltage pulses and the transducer produces accordingly high-frequency ultrasonic waves using a piezoelectric emitter. Generally, the used frequency is within the band of 1MHz to 25MHz and for an efficient use of the technique, the target surface should be covered by water, oil, glycerin or grease.
The ultrasound waves are transmitted and spread through the materials and are reflected from the opposing surface. An interior flaw reflect less the received waves and this fact allows us detecting the flaws regions. Indeed, the wave's amplitude, length and the time it takes to the reflected waves gives much information about the existence, the position and the dimension of the flaws [87].
Due to the high level of penetrating and sensitivity of this technique, it may be used to inspect faults in huge structure like railroad wheels, pressure containers and gas pipeline. For good inspection and accurate analyze of results this technique needs skilled inspector. The UT is considered as a versatile and effective NDT method, because of the following advantages:

- Deals with wide range of materials.

Figure 2.6: Ultrasonic testing device.

- Sensitivity to internal and surface flaws.
- Accurate technique for detecting position, size and shape of flaws.
- Minimal pre-processing of the target and immediate results on screen.
- Multiple use of the technique for flaws detection and estimation of many geometric and physical properties of the material.
- Portability of the technique.

However, it have some limitations like:

- Requirement for great knowledge and experience.
- Need for direct contact to ensure the good transmission of waves.
- Inappropriate for use with porous materials.
- Standards are only for both devices calibration and flaws characterization.
- Linear flaws can not be detected unless they are parallel to the ultrasound source.

2.3.5 Thermographic testing

Thermographic testing also termed as infrared inspection, is a remote technique to inspects flaws, system overloads and degraded insulation in electrical or mechanical components.

Using a highly sensitive infrared camera, the infrared thermography technique find the areas of excess heat that can be a flaw or an overload zone as illustrated in Figure 2.7. The thermal camera is utilized throughout a scanning to select traces of heat that not visible to the naked eye. It allows the examiner to distinguish the flaws based on their color in the spectrogram. A thermographic inspection is more efficient in closed places where no moving air. In mechanical structures the thermograms indicates the heat generated by high friction. As result, this technique makes anomalous thermal patterns visible to the user and indicate the presence of probable flaws, voids, or other deficiencies of the system [88].

Figure 2.7: Thermographic testing.

Among the advantages of the thermographic technique we may mention:

- Safe and efficient technique.
- Possible remote measurements.
- Simple and accurate identification of flaws.
- Easily adaptable to the needs of the user.
- Accurate examination of dangerous and unreachable objects as high-altitude/high voltage wires, nuclear reactors.
- Use for wide range of materials.

- Possibility of inspection of structures during normal operating conditions.

and concerning the disadvantages of this technique we can mention:

- Requirement for experience to interpret results.
- Limitation of use to thin materials.
- Results depend on the radiative properties of the surface.
- Requirement of stationary air between the thermal camera and the tested component to obtain accurate results.
- Need for direct view of the inspected components.
- Underwater structures can not examined.
- Components with fluctuating temperatures are difficult to inspect.

2.3.6 Eddy current testing

Eddy current testing (EDT) is one of the most widely used non-destructive fast procedures for examining electrically conductive materials. It does not require a direct contact between the target and the sensor. The physical distance between the sensor coil and the target component is within the range of some millimeters. The test device is composed of sensor and a display screen as illustrates the Figure 2.8.

Figure 2.8: Eddy current testing device.

2.4 Eddy current testing approach

A wide range of problems can be inspected by the eddy current testing, such as crack, void, inclusion, corrosion, physical and geometric characteristics of a material. In this context, there are many kinds of sensors, such as differential sensors and array sensors that will be described later.

2.4.1 Physical principal

Eddy currents are an induced currents by applying electromagnetic fields on the inspected material. The magnetic field is generated using a copper coil supplied by an alternating current as depicted in Figure 2.9. The induced currents are affected by the target material nature, the existence of flaws and their geometry. Thus, this technique gives information about the flaws in the tested structures through the received eddy current signal. The induced currents produce a secondary magnetic field, which in its turn affect the impedance of the coil [89]. So, we use the coil impedance as an inspection parameter. In this case, the coil is called an absolute sensor because it is considered, at the same time, as an excitation element and as sensor.

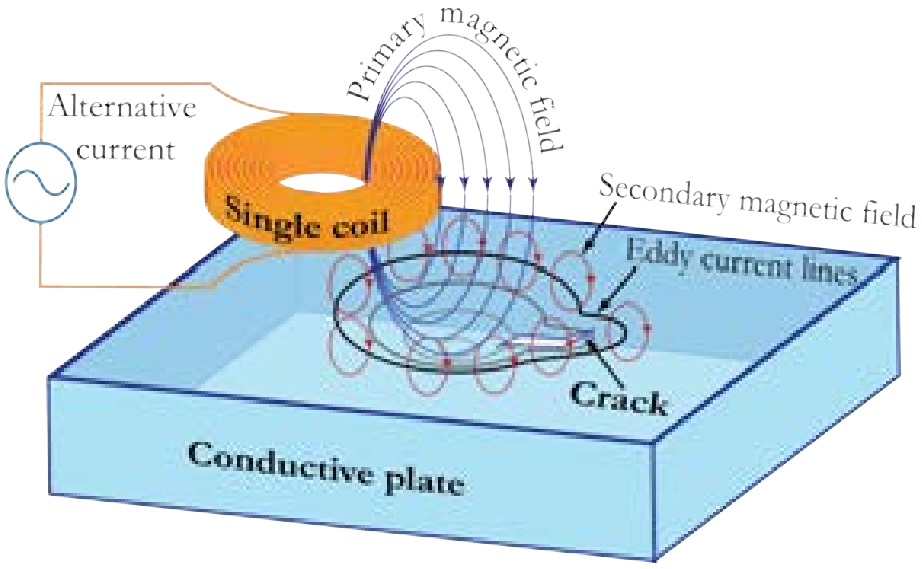

Figure 2.9: Eddy current testing principle.

2.4.2 Classification of sensors

Several criteria are taken into account when classifying sensors. The configuration of the sensors differs according to their geometries, their functions and their control modes. Figure 2.10 summarizes the criteria of classification.

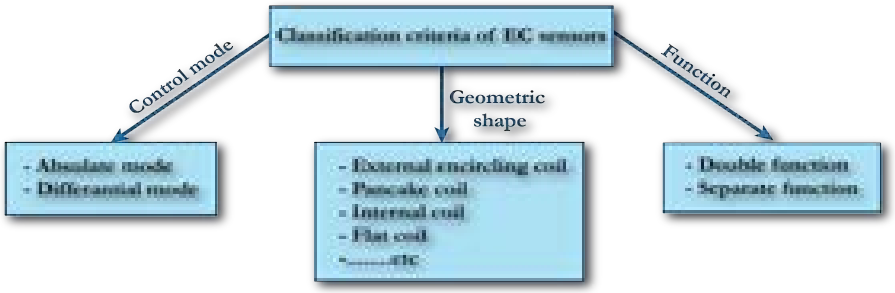

Figure 2.10: Classification criteria of eddy current sensors.

2.4.2.1 Operation modes

There are two common modes of operation:

Absolute mode

In the absolute mode and as illustrated in Figure 2.11a, the single coil creates eddy current and receives changes in the eddy current field as can be seen in Figure 2.11b. The absolute sensor identify long cracks or gradual dimensional changes in pipes and bars. The absolute change in impedance of the coil gives more details about the tested material properties including grain size, hardness, stress and existence of cracks [90].

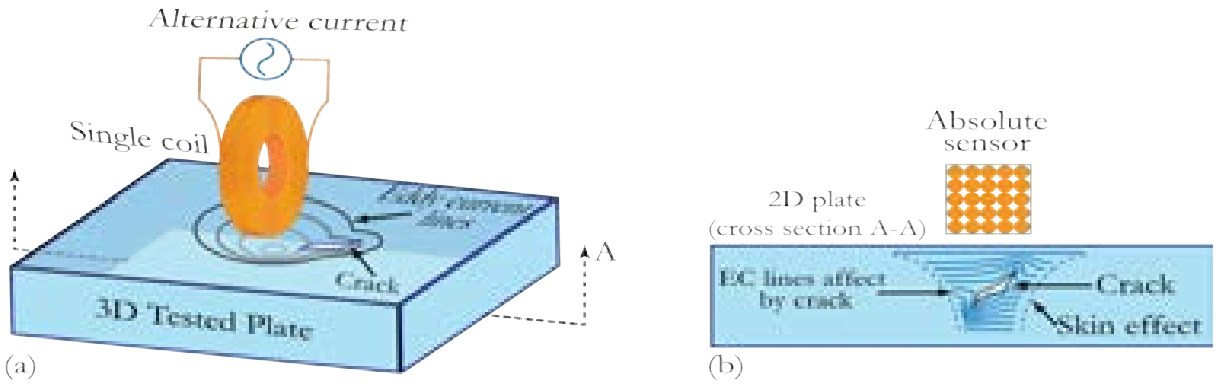

Figure 2.11: Absolute sensor configuration.

Differential mode

Differential probes consist of two coils, the wire is wrapped in the two coils in opposite directions in order to equalize the induced voltages generated by the excitation coils as shown in Figure 2.12. The output voltage of the differential coil probe is affected by the existence of a crack in the tested plate.

Differential sensors are efficient for inspection of very small flaws, but on the other hand, cannot identify progressive dimensions changes in the tested structures because the coils are often quite close [91].

Numerous researchers tried to enhance the sensitivity of differential sensors like the study of Peng et al.[92] where authors developed a new design of the differential sensors based on the use of double gradient winding coils. Another enhancement was introduced on the differential prob to deal with the problem of hot wire testing [93].

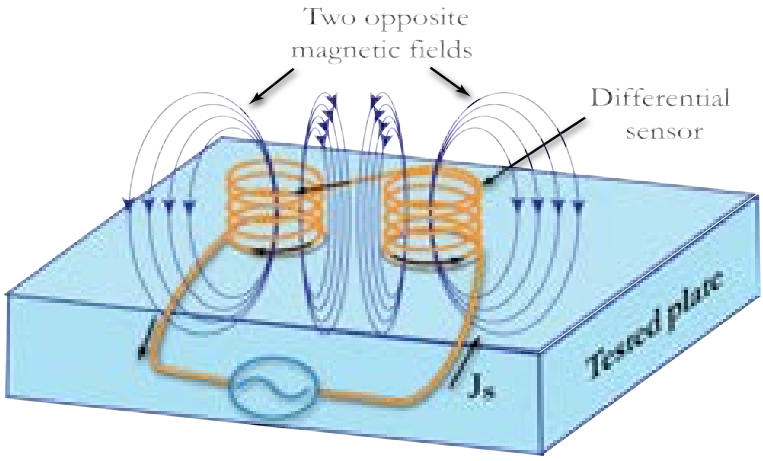

Figure 2.12: Differential sensor configuration.

2.4.2.2 Sensor geometry

Many forms of sensors are designed for several reasons. One of these reasons is to deal adequately with tested material geometry. Indeed, the sensor design should take into account the target surface. For example, the inspection of the component with cylindrical shape, like pipeline, needs an internal encircling coil as illustrated in Figure 2.13a. If there is no possibility to access inside the pipeline, the inspection could be done by an external encircling sensors like the one depicted in Figure 2.13b. For flat components, the inspection requires one of the illustrated sensors in Figures 2.13c and 2.13d.

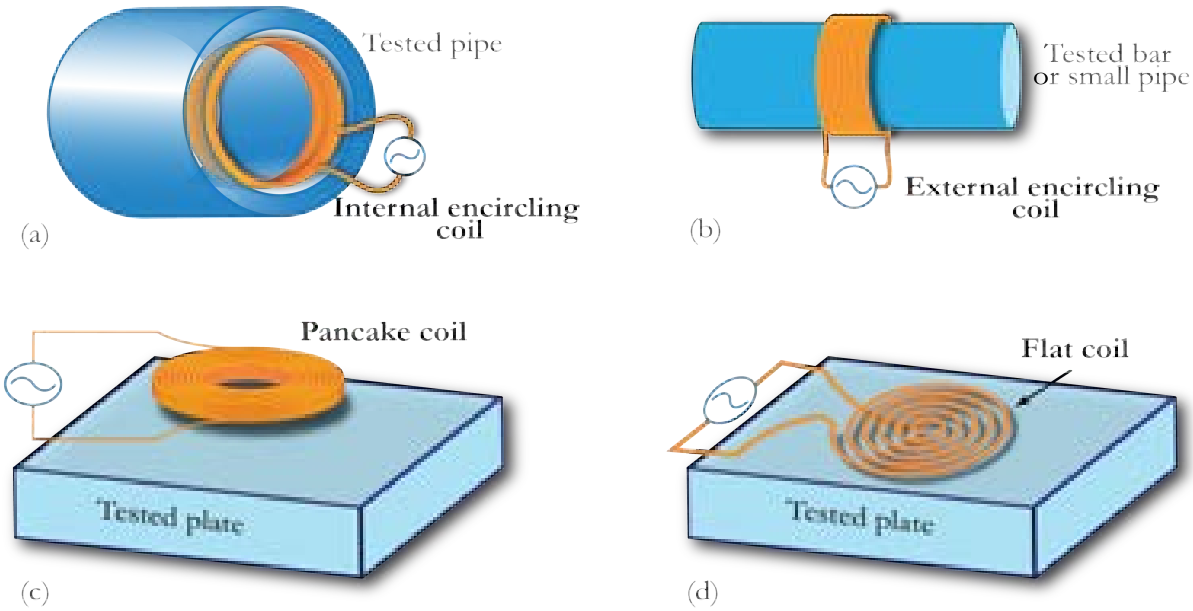

Figure 2.13: Some common sensor shapes.

2.4.2.3 Function type

Based on the number of the used coils and the values of alternative current supplying each coil, we can distinguish two types the sensor.

Double function sensors

Double-function sensor or reflection probe, means one coil used to create eddy excitation current and receive the induced reflected magnetic field as illustrated in Figure 2.14

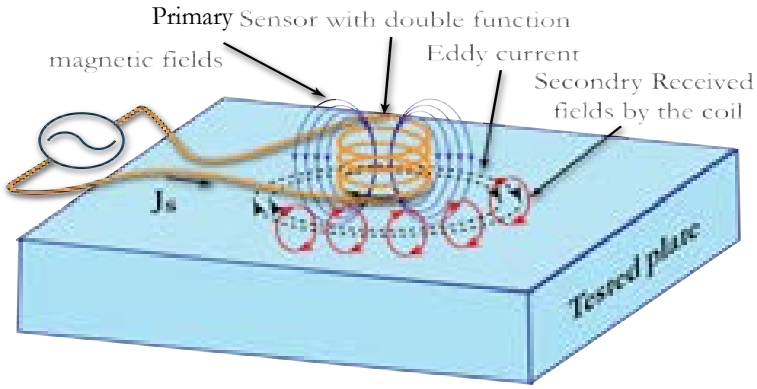

Figure 2.14: Double function sensor.

Separate-function sensors

Separate function sensor mean there two coils, one is used to create the excitation eddy current and the other to receive the induced magnetic field as shown in Figure 2.15. The eddy current is created by customizing the primary coil, and to receive the reflected magnetic field, with sufficient sensitivity, the secondary coil should be smaller than the primary one [94]. Such a type of sensor has the benefit to adjust the coil configuration. A regular and high primary magnetic field can be obtained by adjusting of primary coil diameter, wire diameter and the number of turns. To maximize the reflected field we should adjust the secondary coil dimension according to the crack dimension.

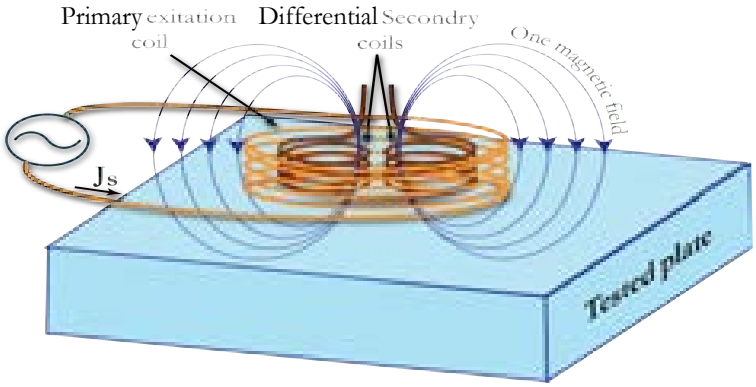

Figure 2.15: Separate function sensor.

2.4.3 Skin effect

In all conductive materials traversed by an alternative current or subjected to a variable electromagnetic field generates induced currents that decrease exponentially from the surface to the inside as shown in Figure 2.16. This effect is called the Skin effect and is governed by the following equations:

$$J_z = J_0 \quad e^{(-z/\delta)} = J_s \quad e^{\left(\frac{-z}{\sqrt{\pi f \sigma \mu}}\right)} \tag{2.1}$$

where:

z: The depth of the tested plate.

J_z: The current density at the depth z.

J_s: The current density on the surface ($z = 0$).

f: The excitation frequency.

μ_r: The relative magnetic permeability of the plate.

μ_0: The magnetic permeability of the vacuum.

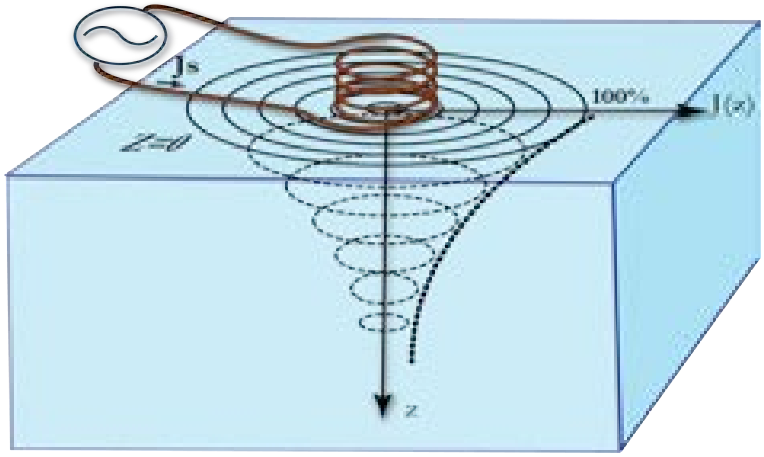

Figure 2.16: Induced current in terms of penetration depth.

σ: The electrical conductivity of the plate.

δ_z: The penetration depth given by:

$$\delta_z = \frac{1}{\sqrt{(\pi f \mu_0 \mu_r \sigma)}} \tag{2.2}$$

The skin effect is mainly characterized by the penetration depth δ_z.

2.4.4 Eddy current testing procedure

According the standard of experimentation "*Magnefest ED-51 0 type*" [71], we use a pencil type probe supplied by an alternative current to inspect a normalized plate. Based on the calibration settings, the inspection is performed at 2 MHz and the test plate should be previously prepared for this experiment. Any coverings or oils on the surface of the examined specimens should be removed carefully without damaging the surface. During the investigation, the next steps should be followed:

1. The surface to be tested must be clean, smooth, and clear of any arbitrary or irregular paint, dust particles, oil,... etc.

2. At first visual inspection should be done if there is any damage or visible discontinuity.

3. The probe will be positioned near the inspection area and the lift-off (distance between the probe an the tested plate) and zero will be adjusted as needed during the inspection procedure.

4. The inspection will be carried out by scanning the surface using the pencil probe at the adequate angle.
5. All indication on the screen should be evaluated.
6. All evaluated indications of deflections will be declared as cracks and registered for post-processing.

This sophisticated technique has many advantages and we can mention among them:

- Detection of any kind of flaws (internal or external).
- Examination of components with complex shapes.
- Minimal pre-processing of the target to be inspected.
- Sensitivity to small cracks.
- Portability of the test device.

Limitation and drawbacks of the eddy current inspection are:

- Limitation to conductive and ferromagnetic materials.
- Requirement for reference standards.
- Limitation of the eddy current penetration.
- Left-off should minimum as can as possible.
- Requirement for skilled and well-trained inspector.
- Inefficiency to detect parallel flaw to the eddy current flow.
- Slow procedure in the case of large structures.

2.4.5 Other applications of eddy current

The eddy current is not limited to NDT and inspection of flaws, but thanks to its powerful features it is useful for the following industrial applications:

2.4.5.1 Eddy current brakes

Eddy current appears in a rotating conductor disk when a stationary magnetic field was generated near it. The braking force is produced by the interaction between the eddy current and the magnetic field as illustrated in Figure 2.19. Such force has been used in many applications like the electromagnetic brakes in heavy-duty vehicles[95]. The eddy current linear brakes are used for high-speed railways[96].

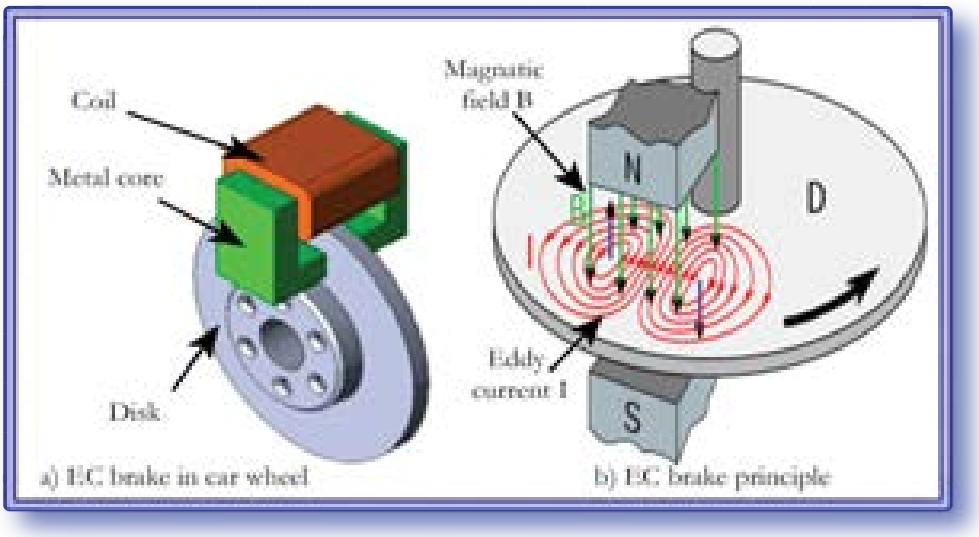

Figure 2.17: Eddy current brake device.

2.4.5.2 Eddy current dampers

Eddy current dampers are promising devices for vibration control of dynamic systems. An example of application is the car suspension system shown in Figure 2.18. Recently, this concept is used in bridge engineering for damping the vibrations that can destroy the whole system. Indeed, in [97] a Laboratory experiments and numerical simulations are carried out to show that an eddy current torque generator can be used as vibrations damper in large scale applications. Obtained results showed that the developed eddy current based damper can achieve a high damping density at a low frequency of the bridge movement.

2.4.5.3 Eddy current heating

Induction heating or eddy current heating, is the process of heating a material inside a coil. When this last is supplied by an high-frequency alternative current, the eddy currents are

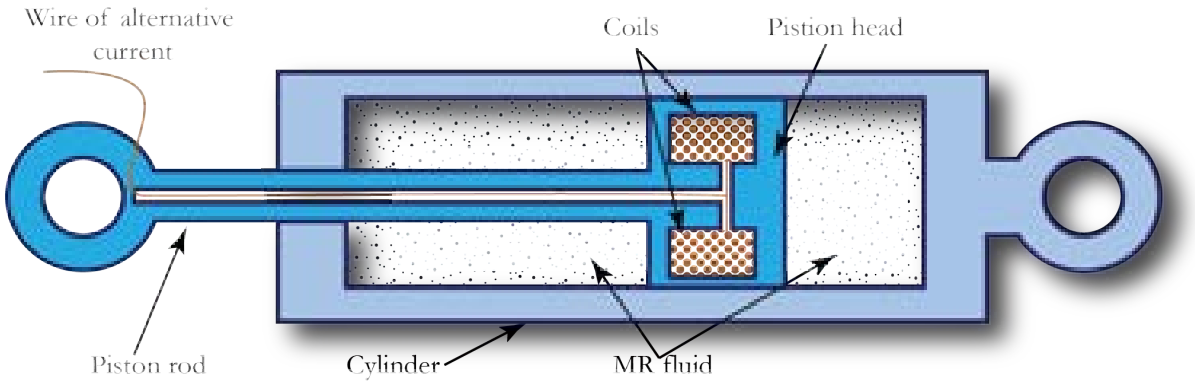

Figure 2.18: Eddy current damping in car suspension.

generated and produce the heat in the target material. Unlike external heating sources, the eddy current heaters produce the heat inside the object. This fact, makes the heating process safe and quick. Furthermore, no direct contact is required for the heating operation. Induction heating is utilized in a variety of industrial applications including cooking machines, metallurgical sector of Figure 2.19, semiconductor refining and melting refractory of metals.

Figure 2.19: Induction heating device.

2.5 Conclusion

In this chapter, we presented briefly some definitions and concepts in the domain of non-destructive testing, followed by a historical review of NDT techniques. Then we described principles of the most popular techniques of non-destructive testing used in the industrial sector namely: visual examination, liquid penetrant testing, magnetic particle testing, ultrasonic testing, radiography, ultrasonic inspection, thermographic testing, and lastly eddy current testing. It goes without saying that each inspection technique has benefits and drawbacks that should be highlighted. We devoted the major part of this chapter to describe in details the eddy current testing technique. We showed its principle, the different types of sensors used in this technique as well as its experimental procedure. Due to its multiple advantages, its programability, its simplicity and its theoretical foundation, we select the eddy current testing to use, in the next chapter, as a tool for crack orientation detection and characterization.

Chapter 3

Mathematical formulation and numerical implementation

3.1 Introduction

The design procedure of any product must passes at first by a simulation step using a numerical model. This last allows study, analysis and even prediction of the different characteristics of the future product (geometric configuration, choice of materials, .. etc.) without the need for a prototype. The modeling step is, therefore, of obvious economic interest. However, any modeling tool must be handled carefully knowing the simplifying assumptions used [98].
The modeling of a magneto-dynamic system with eddy current is based, mainly, on the resolution of the Maxwell's equations. The electromagnetic components of the system change in both space and time. To calculate these components, the accurate method is to integrate the equations governing the system behaviour over time to obtain their values at any point in the space [99].
One of the best methods to solve a such physical problem governed by partial differential equations, is the use of finite elements approach. It is an ideal technique to deal with the resolution of electromagnetic difficulties. For this reason, this approach will be adopted to characterise the cracked materials in our work. Indeed, the first part of this chapter presents the fundamental formulations of electromagnetism obtained from by Maxwell equations and used to build both axisymmetric model and 3Dmodel. In the second part, the finite element method is applied for the simulation of nondestructive testing eddy current approach in two and three-dimensional problems. The impedance of an absolute sensor is, then, determined by a direct method and an energy based one. This chapter is devoted to the theoretical

foundations and the numerical implementation of our main contribution to characterize and to analyze the crack behaviour and its orientation.

3.2 Electromagnetic laws

The fundamental object of electromagnetism is to describe the interactions inside a charged particle system. In a Galilean reference, the force applied on a charge particle q with speed V, is named the Lorentz force and given by [100]:

$$F_l = q(E + V \wedge B) \tag{3.1}$$

Where E, B are respectively the electric and magnetic fields.
The general problem of electromagnetism is solved if we know how to calculate the electric and magnetic fields from the electric load distribution ρ and the current j. We give below the so called Maxwell's equations to calculate the fields E and B from their sources ρ and j.

Ampere's law

The electric field and the induced magnetic field in space around an electric current are proportional to the electric current source of the phenomenon. According to Ampere's Law, the sum of the length elements times the magnetic field in the direction of the length element is equal to the permeability times the electric current traversing any closed loop path as shown by Figure 3.1 [101].

$$\sum B_t \Delta l = \mu_0 I \tag{3.2}$$

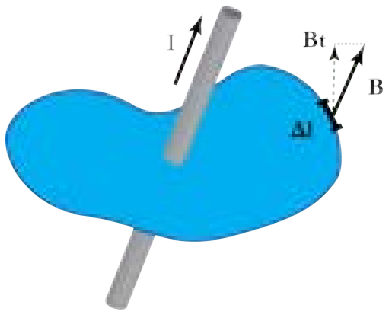

Figure 3.1: Induced magnetic field around an electric current.

In the case of coil in Figure 3.2, the Ampere's law is given as:

$$\int_L \overrightarrow{B}\,\overrightarrow{dl} = \mu_0 \sum_{i=1}^{n} I_i \tag{3.3}$$

with:

B: The induced magnetic field.

dl: Small portion of the coil wire.

I_i: The electric current in turn i.

n: The number of turns.

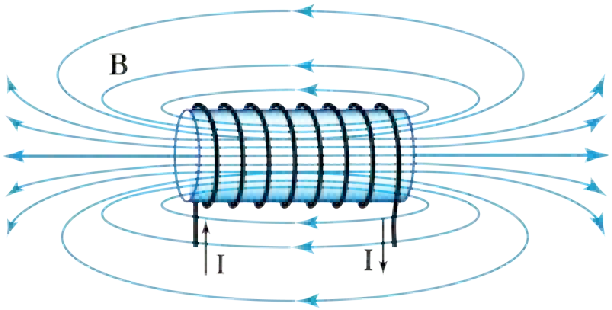

Figure 3.2: Magnetic field induced by a coil.

Faraday's law

Faraday's law is a consequence of the experimental finding by Michael Faraday in 1831. It consist of a time-varying magnetic field that gives rise to an electric field. Specifically, the electromotive force around a closed path C is equal to the negative of the magnetic field increase rate in C [102]; that is:

$$\oint Edl = -\frac{d}{dt}\int_S BdS \tag{3.4}$$

where S is any surface bounded by C as shown, for example, in Figure 3.3.

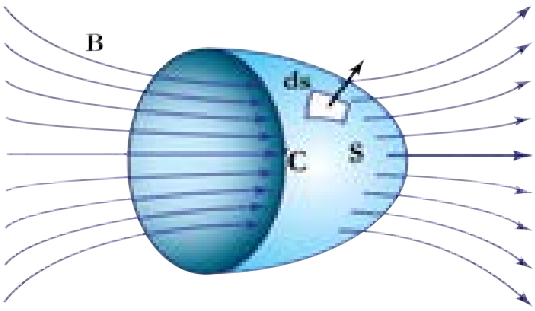

Figure 3.3: Illustration of Faraday's law.

Lenz law

The sign (−) in Faraday's law has the specific meaning given explicitly by Lenz's law. This law was formulated by Heinrich Friedrich Emil Lenz to clarify the phenomenon of induction that Faraday had observed in 1831. It indicates that the direction of an induced current, during an electromagnetic induction phenomenon, is opposite to the variation of the initial flow. In another words, the induced electromotive force opposes the action that gave its birth[102]. Lenz's law applications are plenty and some of them are: eddy current balances, metal detectors, eddy current dynamometers, braking systems, AC generators, card readers, microphones,...etc.

Biot-Savart law

The Biot-Savart law relates magnetic fields to their currents sources. By a similar manner, Coulomb's law relates electric fields to their sources (point charges). Finding the magnetic field, resulting from a current distribution, involves the vector product concept, and it is inherently a calculus problem when the distance from the current to the field point is continuously changing [102]. According to Biot–Savart law, the magnetic flux density is produced

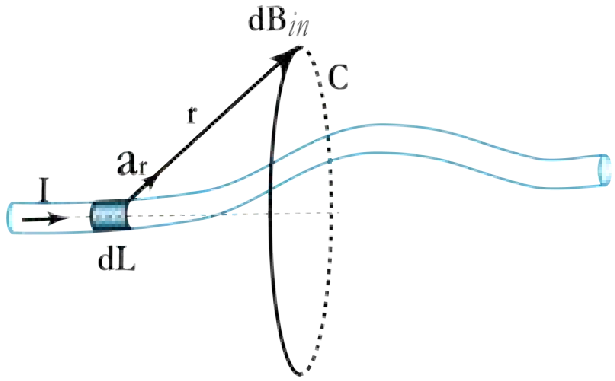

Figure 3.4: Magnetic field of infinitesimal current element.

by current-carrying conductor and is given by:

$$B = \frac{\mu_0}{4\pi} \oint_C \frac{IdL \times a_r}{r^2} \tag{3.5}$$

where μ_0 is the permeability of vacuum and a_r the unit vector directed from the source point.

3.3 Maxwell's equations

Maxwell collected the four differential equations relating the electric vector field $\overrightarrow{E}$ and the magnetic vector field $\overrightarrow{H}$, listed below, and solved them to derive the electromagnetic waves [102]:

$$div(\overrightarrow{B}) = 0 \qquad \textit{(Gauss' Law for Magnetic Fields)} \tag{3.6}$$

$$rot(\overrightarrow{E}) = -\frac{\partial \overrightarrow{B}}{\partial t} \qquad \textit{(Faraday's law of magnetic induction)} \tag{3.7}$$

$$div(\overrightarrow{D}) = \rho \qquad \textit{(Coulomb's law)} \tag{3.8}$$

$$rot(\overrightarrow{H}) = \frac{\partial \overrightarrow{D}}{\partial t} + \overrightarrow{J} \qquad \textit{(Ampere's and Maxwell's law)} \tag{3.9}$$

With the magnetic vector parameters are: $\overrightarrow{B}$ the magnetic induction (Tesla)[T] and $\overrightarrow{H}$ the magnetic field $(Amperes/m)[A/m]$
and the electric vector parameters are: $\overrightarrow{D}$: the electric induction $(Coulomb/m^2)[C/m^2]$, $\overrightarrow{E}$ the electric field $(Volts/m)[V/m]$, $\overrightarrow{J}$ the total current density $(Amperes/m^2)[A/m^2]$ and ρ the volumetric charge density $(Coulomb/m^3)[C/m^3]$.
Notice that expressions (3.6) and (3.8) are called conservation equations while (3.7) and (3.9) are called coupling electromagnetic equations. Additional relationships characterizing the other materials must be added to the previous equations. Indeed, for isotropic materials, we have the following equations called constitutive relations [102]:

$$\overrightarrow{B} = \mu \overrightarrow{H} \tag{3.10}$$

$$\overrightarrow{J} = \sigma \overrightarrow{E} \tag{3.11}$$

$$\overrightarrow{D} = \epsilon \overrightarrow{E} \tag{3.12}$$

$\overrightarrow{E}, \overrightarrow{B}, \overrightarrow{H}, \overrightarrow{D}$ and $\overrightarrow{J}$ are complex vectors. $\overrightarrow{E}$ and $\overrightarrow{H}$ are respectively the electric and magnetic field strengths, $\overrightarrow{B}$ is the magnetic flux density, $\overrightarrow{D}$ is the electric displacement field, $\overrightarrow{J}$ is the current density and ρ is the electric charge density.
Furthermore, μ is the magnetic permeability $(Henries/meter)[H/m]$, ϵ the electric permittivity $(Farad/meter)[F/m]$ and σ the electric conductivity $(Siemens/m)[S/m)]$.
The magnetic permeability of a magnetic material is:

$$\mu = \mu_0 \mu_r \tag{3.13}$$

Where $\mu_0 = 4\pi 10^{-}7 H/m$ the magnetic permeability of vacuum [103]. The relative magnetic permeability for non-magnetic material (studied material) is $\mu_r = 1$.

Materials with a high relative permeability value $\mu_r >> 1$ are called ferromagnetic materials due the fact they own innate ability to exhibit magnetic effects. Ferromagnetic materials are magnetized easily and in strong magnetic fields the magnetization does not return to its original value.

The electric permittivity of a magnetic material is:

$$\epsilon = \epsilon_0 \epsilon_r \tag{3.14}$$

$$\epsilon_0 = \frac{1}{\mu_0 C^2} \tag{3.15}$$

With $\epsilon_0 = 8.8419 \quad 10^{-12}(F/m)$ the electric permittivity of vacuum [103], ϵ_r the relative electric permittivity of studied material and $C = 3 \quad 10^8 m/s$ the light speed.

Table 3.1 summarizes the relative permeability, electric permittivity and electric conductivity of some commonly used materials [104].

material	μ_r	ϵ_r	$\sigma(s/m)$
Vacuum	1	1	0
Air	1.00000037	1.000589	$10^{-9} - 10^{-15}$
Wood(dry)	1.00000043	1.5-4	$10^{-14} - 10^{-16}$
Concrete(dry)	1	4.5-8	0.065[105]
Aluminum	1.000022	2.2-3.4	37.710^6
Copper	0.999994	1	58.1310^6
Carbon steel	100	...	...
Stainless steel	750-950	...	....
Iron (99.8 pure)	100	...	58.1310^6

Table 3.1: Relative permeability, permittivity and electric conductivity of some materials.

For a conductive material, the current density is given by the generalized Ohm law:

$$\overrightarrow{J} = \overrightarrow{J}_s + \overrightarrow{J}_{ind} \tag{3.16}$$

$$\overrightarrow{J}_{ind} = \sigma(E + u \wedge B) \tag{3.17}$$

with $\overrightarrow{J}_s[A/m^2]$ the current density imposed to the inductor(coil), $\overrightarrow{J}_{ind}[A/m^2]$ the induced current density, $\sigma E[A/m^2]$ the density of induced currents by variation of the electric field E and $\sigma u \wedge B[A/m^2]$ the current resulting from the movement of coil at speed of scan $u[m/s]$.

3.4 Simplifying hypotheses

The equations presented above describe, generally, all electromagnetic phenomena; however they are, in most cases, difficult to solve directly. Depending on the geometric form of the studied system, the effect of some parameters become negligible and as a result, the equations can be reduced to simpler form [106]. Indeed, the following simplifying hypotheses can be considered:

- The volumetric density of charge is considered zero ($\rho = 0$).
- The supply currents are assumed created by a perfect current generator.
- The term $\frac{\partial \vec{D}}{\partial t}$ is generally negligible in low frequency scale.
- The remanent magnetic induction is considered zero ($Br = 0$).
- The superficial current density in the interface between two domains is zero ($\vec{J}_s = 0$).

Using these hypotheses, the Maxwell's equations become:

$$rot(\vec{E}) = -\frac{\partial \vec{B}}{\partial t} \tag{3.18}$$

$$rot(\vec{H}) = \vec{J} \tag{3.19}$$

$$div(\vec{B}) = 0 \tag{3.20}$$

$$div(\vec{D}) = 0 \tag{3.21}$$

with the Ohm's law:

$$\vec{J} = \vec{J}_s + \sigma E + \sigma(u \wedge B) \tag{3.22}$$

3.5 Magnetodynamic formulations

The resolution of Maxwell's equations can be achieved by considering fields as unknown. However, it is often preferred to express the electric and magnetic fields according to the potential. Indeed, it has been shown that the obtained system, under unknown fields ($\vec{E}, \vec{H}$), converges less well than if we work with potential[107].

The formulation of Maxwell's equations in simpler form is necessary in order to reduce the number of unknown parameters and simplify, hence, the resolution procedure. There are a large number of Maxwell's equations formulations and, in our case, we present the frequently used one in order to study the inductive sensor and the associated eddy current. The problem

formulation can be done using either: field variables ($\overrightarrow{E}, \overrightarrow{H}.$) or potential variables ($\overrightarrow{T} - \phi, \overrightarrow{A} - V$) [107].

3.5.1 Formulation based on electric field

The formulation in an electric field is obtained by making the time derivative of the Maxwell-Ampere equation (3.9) while assuming that the permeability is time invariant (case of linear materials). The obtained expression is [106]:

$$rot\left[\frac{1}{\mu} rot\overrightarrow{E}\right] + \sigma\frac{\partial\overrightarrow{E}}{\partial t} = 0 \tag{3.23}$$

3.5.2 Formulation based on electrical vector potential

Since the induced current density divergent is zero ($div\,\overrightarrow{J} = 0$), an electrical vector potential, named T, can be introduced [100]:

$$\overrightarrow{J} = rot\overrightarrow{T} \tag{3.24}$$

As for all other formulations, the uniqueness of the solution requires the introduction of a gauge (coulomb gauge for example); which gives the expression below:

$$rot\left[\frac{1}{\sigma} rot\overrightarrow{T}\right] + \mu\frac{\partial}{\partial t}[\overrightarrow{T} - grad\phi] = 0 \tag{3.25}$$

The choice of a formulation is mostly determined by computer resources, implementation, and precision, depending on the size and complexity of the problem to be solved.
The dual formulations ($\overrightarrow{E}, \overrightarrow{H}$) of the Maxwell's equations do not require a gauge for the solution uniqueness because it admits a single solution in given situations with acceptable boundary limitations [108].

3.5.3 Formulation based on magnetic vector potential

This formulation applies to electrotechnical devices in which current or voltage sources are time varying. In this case, the term $\frac{\partial\overrightarrow{B}}{\partial t}$ is not null and the electric and magnetic fields are coupled by induced currents [109].
In what follows, we are interested in the formulation $\overrightarrow{A} - V$ in the general case and we rewrite the Maxwell's equations as:

$$rot(\overrightarrow{E}) = -\frac{\partial\overrightarrow{B}}{\partial t} \tag{3.26}$$

$$div(\overrightarrow{B}) = 0 \tag{3.27}$$

According to the flux conservation equation (3.27),the magnetic induction $\overrightarrow{B}$ given by:

$$\overrightarrow{B} = rot\,\overrightarrow{A} \tag{3.28}$$

where $\overrightarrow{A}$ is the magnetic vector potential.
Combining (3.28) with (3.26) gives :

$$rot\left(\overrightarrow{E} + \frac{\partial \overrightarrow{A}}{\partial t}\right) = 0 \tag{3.29}$$

This means that the field $\left(\overrightarrow{E} + \frac{\partial \overrightarrow{A}}{\partial t}\right)$ is a conservative field which leads to:

$$\left(\overrightarrow{E} + \frac{\partial \overrightarrow{A}}{\partial t}\right) = -gradV \tag{3.30}$$

So, the electric field $\overrightarrow{E}$ is given by:

$$\overrightarrow{E} = -\left(\frac{\partial \overrightarrow{A}}{\partial t} + gradV\right) \tag{3.31}$$

Replacing equation (3.10) in (3.19) leads to:

$$rot\left(\frac{\overrightarrow{B}}{\mu}\right) = \overrightarrow{J} \tag{3.32}$$

Considering equations (3.28) and (3.22) in (3.32) to obtain:

$$rot\left(\frac{1}{\mu} rot\,\overrightarrow{A}\right) = \overrightarrow{J}_s + \sigma\overrightarrow{E} + \sigma(u \wedge \overrightarrow{B}) \tag{3.33}$$

and replacing $\overrightarrow{E}$ by its expression (3.31) in equation (3.33) gives:

$$rot\left(\frac{1}{\mu} rot\,\overrightarrow{A}\right) = \overrightarrow{J}_s - \sigma\left(\frac{\partial \overrightarrow{A}}{\partial t} + gradV\right) + \sigma(u \wedge \overrightarrow{B}) \tag{3.34}$$

By another way:

$$rot\left(\frac{1}{\mu} rot A\right) + \sigma\left(\frac{\partial A}{\partial t}\right) + \sigma gradV - \sigma(u \wedge B) = \overrightarrow{J}_s \tag{3.35}$$

In order to solve this equation with the two unknowns ($\overrightarrow{A}$, V), the divergence of the potential must be ensure the uniqueness of the solution. We then add the condition $div\,\overrightarrow{A} = 0$ called Coulomb gauge, to obtain:

$$\begin{cases} rot\left(\frac{1}{\mu} rot\,\overrightarrow{A}\right) + \sigma\left(\frac{\partial \overrightarrow{A}}{\partial t}\right) + \sigma gradV - \sigma(\overrightarrow{u} \wedge \overrightarrow{B}) = \overrightarrow{J}_s \\ div\,\overrightarrow{A} = 0 \end{cases} \tag{3.36}$$

This gauge hypothesis is naturally checked in the case of axisymmetric configuration. The term $gradV$ in axisymmetric is zero. For low speeds of scan displacement, we can neglect the term $\sigma(\overrightarrow{u} \wedge \overrightarrow{B})$ and the system (3.36) becomes:

$$rot\left(\frac{1}{\mu} rot\overrightarrow{A}\right) + \sigma\left(\frac{\partial \overrightarrow{A}}{\partial t}\right) = \overrightarrow{J}_s \tag{3.37}$$

If the type of the source current is sinusoidal, the term $\sigma\left(\frac{\partial \overrightarrow{A}}{\partial t}\right)$ can be replaced by $jw\sigma\overrightarrow{A}$ with w the pulsation of the sources and $j^2 = -1$. Thus, the equation (3.37) becomes:

$$rot\left(\frac{1}{\mu} rot\overrightarrow{A}\right) + jw\sigma\overrightarrow{A} = \overrightarrow{J}_s \tag{3.38}$$

This is the magnetodynamic equation that translates the phenomenon of penetration of induced currents and the behavior of the transitional regime of electrical machines [109]. The usage of a such formulation is extremely helpful in resolving non-destructive testing-eddy current problems.

Axisymmetric model

The modeling of devices with symmetrical evolution along an axis allows reducing the three-dimensional model to a two-dimensional axisymmetric model as shown in Figure 3.5. The

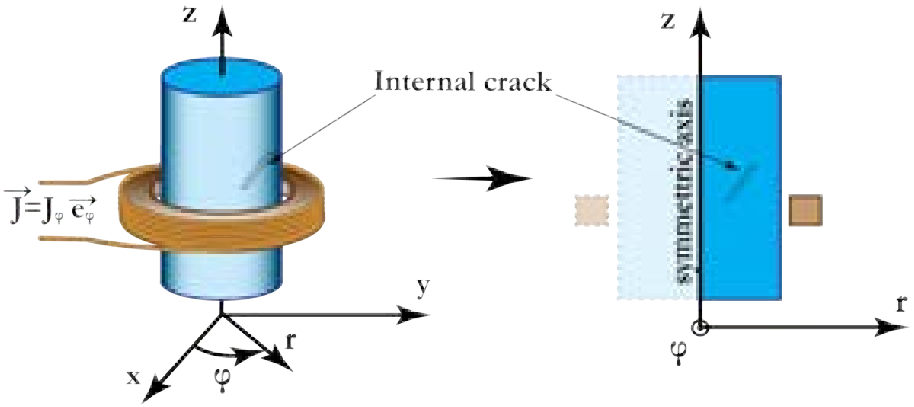

Figure 3.5: Axisymmetric device charged according to the direction φ.

direction of $\overrightarrow{J}s = J_s \quad \overrightarrow{e}_\varphi$ according to φ, leads to the direction of $\vec{E}, \vec{A}, \vec{B}, \vec{H}$ in the base $\vec{e_r}, \vec{e_\varphi}, \vec{e_z}$ as fellows:

$$\overrightarrow{E} = \begin{Bmatrix} 0 \\ E_\varphi \\ 0 \end{Bmatrix}; \qquad \overrightarrow{A} = \begin{Bmatrix} 0 \\ A_\varphi \\ 0 \end{Bmatrix}; \qquad \overrightarrow{B} = \begin{Bmatrix} B_r \\ 0 \\ B_z \end{Bmatrix}; \qquad \overrightarrow{H} = \begin{Bmatrix} H_r \\ 0 \\ H_z \end{Bmatrix} \tag{3.39}$$

In cylindrical coordinates, we have:

$$\overrightarrow{rot}\,\overrightarrow{A} = \frac{1}{r}\begin{vmatrix} \vec{e_r} & \vec{e_\varphi} & \vec{e_z} \\ \frac{\partial}{\partial r} & \frac{\partial}{\partial \varphi} & \frac{\partial}{\partial z} \\ A_r & A_\varphi & A_z \end{vmatrix} \tag{3.40}$$

With

$$\overrightarrow{rot}\,\overrightarrow{A} = \frac{1}{r}\left[-\frac{\partial r A_\varphi}{\partial z}\right]\overrightarrow{e_r} + \frac{1}{r}\left[-\frac{\partial r A_\varphi}{\partial r}\right]\overrightarrow{e_z} \tag{3.41}$$

After that, we obtain:

$$\overrightarrow{rot}\left(\frac{1}{\mu}\overrightarrow{rot}\,\overrightarrow{A}\right) = \left[-\frac{\partial}{\partial r}\left(\frac{1}{\mu r}\frac{\partial (rA_\varphi)}{\partial r}\right) - \frac{\partial}{\partial z}\left(\frac{1}{\mu}\frac{\partial A_\varphi}{\partial z}\right)\right]\overrightarrow{e_z} \tag{3.42}$$

Replacing the term rA_φ by A^*, the equation (3.38) becomes:

$$-\frac{\partial}{\partial r}\left(\frac{1}{\mu r}\frac{\partial (A^*)}{\partial r}\right) - \frac{\partial}{\partial z}\left(\frac{1}{\mu r}\frac{\partial A^*}{\partial z}\right) + \frac{\sigma j w \sigma A^*}{r} = J_{s\varphi} \tag{3.43}$$

This last equation represents the magnetic vector potential formulation of the magneto-dynamic problem in the axisymmetric case.

2D-Cartesian model

The source current J_s is oriented in the direction z as depicted in Figure 3.6. This resulting in a single component z for the magnetic vector potential and two components x and y for the magnetic field H and the magnetic field density B as shows the expression (3.44) in the base $\vec{i}, \vec{j}, \vec{k}$.

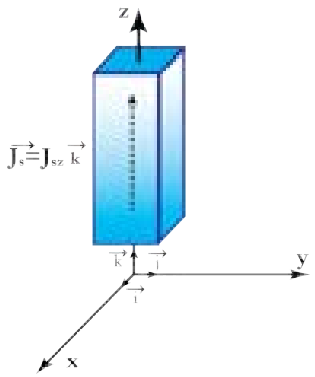

Figure 3.6: 2D device with source current oriented to the direction Z.

$$A = \begin{Bmatrix} 0 \\ 0 \\ A_z \end{Bmatrix}; \qquad H = \begin{Bmatrix} H_x \\ H_y \\ 0 \end{Bmatrix}; \qquad B = \begin{Bmatrix} B_x \\ B_y \\ 0 \end{Bmatrix} \tag{3.44}$$

In Cartesian coordinates, we have:

$$\overrightarrow{rot}\overrightarrow{A} = \begin{vmatrix} \vec{i} & \vec{j} & \vec{k} \\ \frac{\partial}{\partial x} & \frac{\partial}{\partial y} & \frac{\partial}{\partial z} \\ 0 & 0 & A_z \end{vmatrix} \tag{3.45}$$

Hence,

$$\overrightarrow{rot}\overrightarrow{A} = \left[\frac{\partial A_z}{\partial x}\right]\overrightarrow{j} + \left[\frac{\partial A_z}{\partial y}\right]\overrightarrow{i} \tag{3.46}$$

And

$$\overrightarrow{rot}\left(\frac{1}{\mu}\overrightarrow{rot}\overrightarrow{A}\right) = -\frac{\partial}{\partial x}\left(\frac{1}{\mu}\frac{\partial A_z}{\partial x}\right) - \frac{\partial}{\partial y}\left(\frac{1}{\mu}\frac{\partial A_z}{\partial y}\right) \tag{3.47}$$

The equation (3.38) in cartesian coordinates becomes:

$$-\frac{\partial}{\partial x}\left(\frac{1}{\mu}\frac{\partial A_z}{\partial x}\right) - \frac{\partial}{\partial y}\left(\frac{1}{\mu}\frac{\partial A_z}{\partial y}\right) + jw\sigma A_z = J_{sz} \tag{3.48}$$

In 2D-Cartesian coordinates, this equation represents the magnetic vector potential formulation of the magnetodynamic problem.

Specifications of the model regions

This developed model is used to perform simulations of the set: sensor (coils Ω_i), tested metal plate Ω_c shown in Figure 3.7. The tested plate contains external or internal flaws. The model includes the air Ω_a around the sensor and the plate. the distance (Lift-off) between the sensor and the plate chosen by default as $L_f = 0.5mm$. The sensor is made by a coil of copper wire and can be formed of two coils in case of differential mode. The bi-dimensional model can substitute the axisymmetric model of the 3D problem will treat in the next chapter. The model being axisymmetric means that it remains unchanged by rotating it around the vertical axis z and is, therefore, sufficient to limit the study to a two-dimensional model.
The presented model consists of three regions:

- **Inductor(coils Ω_i):** formed of a coil or two mounted in series but with reversed winding to ensure two opposing flows. Two cases can be considered:

  1. Coils powered by a voltage source, the scalar potential is the voltage of the source V and the Equation (3.38) becomes:

$$\overrightarrow{rot}(\frac{1}{\mu}\overrightarrow{rot}\overrightarrow{A}) = -grad(V) \tag{3.49}$$

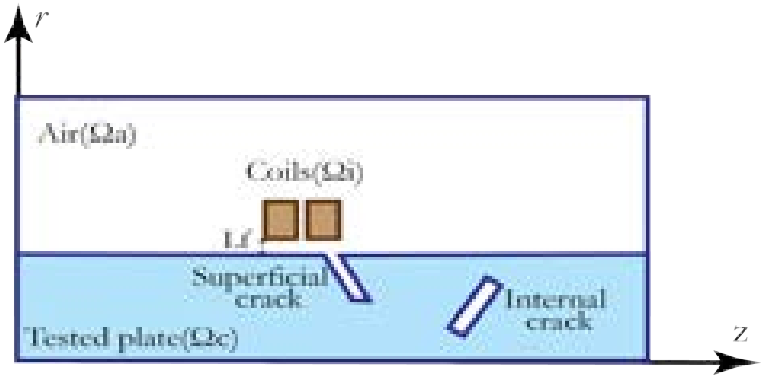

Figure 3.7: Illustration of different regions of axisymmetric model.

2. Coils supplied by a known J_s density current source with a uniform distribution in the conductor portion and the equation (3.38) becomes:

$$\overrightarrow{rot}(\frac{1}{\mu}\overrightarrow{rot}\,\overrightarrow{A}) = \overrightarrow{J_s} \tag{3.50}$$

- **Non-conductive region (air Ω_a):** In our case, this region consists of an air around the coils and the plate and the equation (3.38) becomes:

$$\overrightarrow{rot}(\frac{1}{\mu}\overrightarrow{rot}\,\overrightarrow{A}) = \overrightarrow{0} \tag{3.51}$$

- **Conductive region (tested plate Ω_c):** tested conductive plate either electrically (as aluminum) or magnetically (as steel). The dynamic regime appear in this region and the equation (3.38) becomes :

$$\overrightarrow{rot}(\frac{1}{\mu}\overrightarrow{rot}\,\overrightarrow{A}) = \sigma\frac{\partial\overrightarrow{A}}{\partial t} \tag{3.52}$$

with

$$-\sigma grad(V) = 0 \tag{3.53}$$

Some factors, related to the material atomic structure, can influence its electrical conductivity such as temperature, flaws and residual stresses. For this reason, we consider defects or heterogeneities as an area with modified electrical conductivity. Given the relationship between the size of these defects and the induced currents, the NDT-EC technique is exploited for the detection of defects, where the representational equation of the existence of these defects is given by equation (3.52).

3.6 Boundary and interface conditions

According to the electromagnetic nature of the problem, the electromagnetic wave propagates to infinite space. However, it can be limited to the studied domain by sufficient boundary conditions. In addition, this studied domain has many regions that need interface conditions between them to ensure the continuity of electromagnetic wave propagation.

3.6.1 Boundary conditions

The equation (3.38) with the boundary conditions allows the determination of the magnetic vector potential $\overrightarrow{A}$ in its field of resolution. Generally, the boundary conditions are:

- **Dirichlet condition:** the value of the vector potential is imposed on the boundary of the studied domain Γ_a as shown in Figure 3.8 and expressed as:

$$\overrightarrow{A}|_{\Gamma a} = A_0 \tag{3.54}$$

  for a natural condition of Dirichlet $A_0 = 0$ along the boundary Γ_a.

- **Condition of Neumann:** The derivative of the vector potential with respect to the normal to the surface Γ_s, shown in Figure 3.8, is imposed as given in (3.55).

$$\left.\frac{\partial A}{\partial n}\right|_{\Gamma_s} = A_n \tag{3.55}$$

  This condition is used for problems that have a symmetry of the geometry and current excitation ($\frac{\partial \overrightarrow{A}}{\partial n}|_{\Gamma s} = 0$). We can also use this condition for an interface with an infinite permeability material.

- **Mixed condition:** Named alternatively Dirichlet Neumann condition given by:

$$\left|aA + b\frac{\partial A}{\partial n}\right|_{\Gamma m} = c \tag{3.56}$$

  with a, b, c constants.

3.6.2 Interface conditions

The electromagnetic fields undergo discontinuities when it is moving between different materials and it needs conditions for the passage between those materials. The two domains Ωa and Ωc having different physical properties separated by an interface Σ as illustrated in

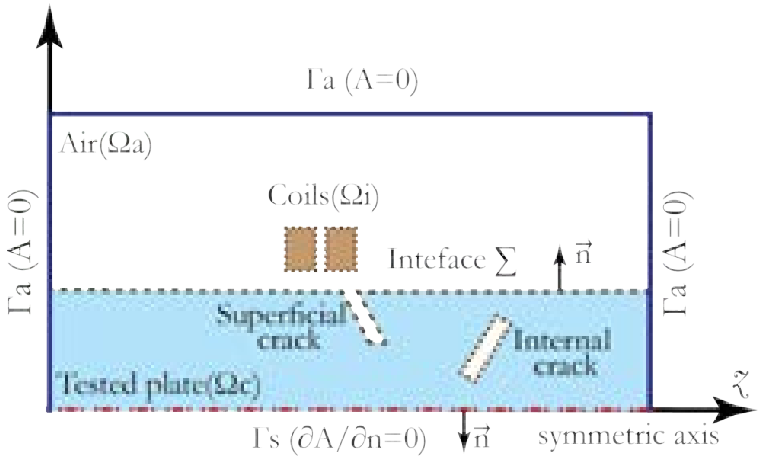

Figure 3.8: Boundary conditions on the interface.

Figure 3.8. In our case, there is a change of domain represented by a strong variation of the conductivity between the air and the studied metal plate. By calling $\overrightarrow{n}$, the normal vector to the air/metal interface Σ, the governing equations (3.37) are valid at any point in the continuous domain. At the interface between air and plate of indices 1 and 2 respectively, there are the following conditions[110]:

- Continuity of the tangential component of the electric field $\overrightarrow{E}$.

$$\overrightarrow{E}_1 \wedge \overrightarrow{n} = \overrightarrow{E}_2 \wedge \overrightarrow{n} \tag{3.57}$$

- Continuity of the normal component of the magnetic induction $\overrightarrow{B}$.

$$\overrightarrow{B}_1 \cdot \overrightarrow{n} = B_2 \cdot \overrightarrow{n} \tag{3.58}$$

- Discontinuity of the tangential component of the magnetic field $\overrightarrow{H}$.

$$\overrightarrow{n} \wedge (\overrightarrow{H}_2 - \overrightarrow{H}_1) = \overrightarrow{J}_s \tag{3.59}$$

- Discontinuity of the normal component of the electric induction $\overrightarrow{D}$, in presence of a superficial charge ρ_s

$$\overrightarrow{n} \cdot (\overrightarrow{D}_2 - \overrightarrow{D}_1) = \rho_s \tag{3.60}$$

with $\vec{n}$ the normal at the interface Σ between two domains.
These passage conditions indicate that the tangential component of the electric field $\vec{E}$ (3.57) and the normal component of the magnetic induction $\vec{B}$ (3.58) are continuous. On the other hand, if superficial density of charge ρ_s and current $\overrightarrow{J}_s$ are present at the interface Σ, the tangential component of the magnetic field $\vec{H}$ (3.59) and the normal component of the electrical induction $\vec{D}$ (3.60) are discontinuous.

3.7 Different methods of resolution

The partial derivative equation (3.38), previously established, is describing the electromagnetic systems. The resolution of this equation by analytical methods is impossible, in the general case, due to the complex geometry of the studied device or the nonlinear magnetic properties of the materials. In this case, only numerical methods can be used. Indeed, instead of solving the equations analytically, the vector potential is discretisized in a finite number of points [106]. Then, several numerical methods can be used for the resolution of partial derivative equations. In this context , the most known are the integral method, the finite difference method, the finite volume method and the finite element method. In recent years, a combination of these numerical methods or a combination with analytical ones are adopted for resolution of certain types of problems [111].

3.7.1 Boundary element method

This method is based on a subdivision of nodes distributed on the boundaries of the device regions. From the values on borders, it is possible, in some cases, to calculate the fields, if necessary, within the resolution domain. Among the disadvantage of this method is its difficulty to take into consideration the saturation concept, the need for a memory space and the requirement for a significant calculation time. This is due to the involved matrices in the method [106]. Generally, in magnetostatic we use the integral boundary method or a combination with the finite elements to calculate the electromagnetic fields in linear and non-conductive material [112].

3.7.2 Finite difference method

Historically speaking, it is the first simple numerical method used for the resolution of partial derivative equations. It was, firstly, used for simple geometries, particularly those of the electromagnetic fields. Its 2D version consists of meshing the target areas using rectangular elements. It can be seen as a discretizing process of the studied domain by a network of connected nodes that in their turn create a rectangular meshes. This procedure allows replacing the differential operator with difference one between the values of the unknown neighboring points. After taking into account the boundary conditions and the interface conditions, between the different parts of the model, an algebraic system is achieved.
The major disadvantages of the finite difference method is the difficulty to mesh and studying complex geometries. In addition, it only succeeds in the nodal values of the magnetic vector

potential, which requires an additional process of interpolation to determine the values of the magnetic vector potential in the other points of the resolution domain [109, 113].

3.7.3 Finite volume method

The finite volume method was developed by Spalding and Patankar [114]. It is a method of weighted residues, for which the weight functions are equal to the unit of the finite volume. It consists of discretizing the partial derivative equations by integrating finite volumes surrounding the mesh nodes rather than the node itself (as the finite difference method do). Indeed, in the case of this method, the integration domain is subdivided into control volumes for each mesh node. Unlike the finite element method, here the global matrix is constructed by each side of the finite volume [115]. The finite volume method is a process of discretization and numerical resolution used, particularly, in fluid mechanics and in significant progress in other branches of engineering like thermal transfer, electromagnetism ... etc.[110]. This method involves subdividing the field of study in elementary volumes that each one surrounds a node. The partial differential equation, of the problem, is integrated on an elementary volume. To calculate the integral on each elementary volume, the unknown function is expressed by an approximation between the two consecutive nodes. Then, the integral form is discretized in the target field. Compared to the finite elements, the discretization by the finite volume method leads to a linear system with a larger matrix and this allows faster convergence of the iterative solvers [115].

3.7.4 Coupled circuits method

The principle of coupled circuits is to make the analogy between electrical quantities and the studied quantities (magnetism quantities in our case). The process consists in subdividing the target area into elementary circuits. By application of the laws of Kirchhoff to these elementary circuits, we can calculate the distribution of the elementary variables [106]. Since the appearance of this method, it still extending its spectre to applications in the electromagnetism domain including induction heating and non-destructive testing by eddy currents. Indeed, authors of [116]proposed this method in the field of induction heating and modeled an inductor with a ferrite pot using the fictitious currents. In [111], the objective was to extend this method to the case of NDT-EC systems.

3.7.5 Analytical methods

The analytical solution of Maxwell's equations allows obtaining an exact mathematical solution of the problem. Nevertheless, it remains limited to simple systems. Among these analytical methods the one based on separating the variables of the system. We can use this method to find an analytical solution for the problem of the axisymmetric coil in Figure 3.9a. We can use it also for a coil surrounding an infinitely long circular conducting rod with a uniformly thick coating of another conductor as the one shown in Figure 3.9b and studied in [117]. In this last study, the authors proposed an analytical solution to the differential equations governing the system, and the solution is obtained based on a technique of integration with variables separation of the problem shown in Figure 3.9a. In [117] authors are interested

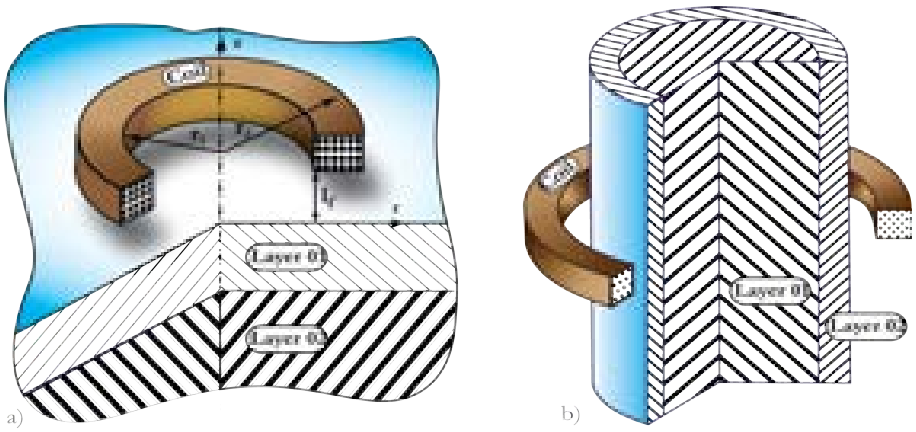

Figure 3.9: Geometry of the treated problem by Dodd et al.[33]

in an isotropic, linear, and homogeneous material and solving the following equation:

$$\nabla \wedge (\nabla \wedge \overrightarrow{A}) - \nabla^2 \overrightarrow{A} = -\mu\sigma \frac{\partial \overrightarrow{A}}{\partial t} + \mu \overrightarrow{J}_s \tag{3.61}$$

where $\overrightarrow{A}$ is the magnetic vector potential and $\overrightarrow{J}_s$ the excitation current density. For axisymmetric problem, it is more comfortable to work in a cylindrical coordinate; hence, the magnetic vector potential $\overrightarrow{A}$ and the current density $\overrightarrow{J}_s$ can be written as:

$$\overrightarrow{A} = A(r,z)\overrightarrow{e}_\theta \tag{3.62}$$

$$\overrightarrow{J}_s = J_s(r,z)\overrightarrow{e}_\theta \tag{3.63}$$

By picking an appropriate gauge condition such as $\nabla \overrightarrow{A} = 0$ and considering a sinusoidal excitation current, we may reformulate the equation (3.61) as follows:

$$\frac{\partial^2 A(r,z)}{\partial r^2} + \frac{1}{r}\frac{\partial A(r,z)}{\partial t} + \frac{\partial^2 A(r,z)}{\partial z^2} - \frac{A(r,z)}{r^2} = -\mu J_s(r,z) + j\omega\sigma\mu A(r,z) \tag{3.64}$$

For all areas except the coil, the general solution of equation(3.64) is [98] :

$$A(r,z) = \int_0^\infty \left[A_i e^{\alpha_i z} + B_i e^{-\alpha_i z}\right] [C_i J_1(\alpha r) + D_i Y_1(\alpha r)] d\alpha \tag{3.65}$$

with

$$\alpha_i = \sqrt{\alpha^2 + j\omega\sigma_i\mu_i} \tag{3.66}$$

with μ_i the magnetic permeability and $\sigma_i$the electric conductivity in region i. J_1 and Y_1 represent the functions of first and second species, respectively, of the first order Bessel. $A_i, B_i, C_i and D_i$ are constants that can be determined by the boundary and interface conditions.

Other works developed, in the context of analytical solution for problems of coil with a magnetic core and a flat plate, are those presented in [116, 118]. It consists, in [116] of a half-conductor plate excited by a cylindrical coil and the calculation are made to detect a flaw in the board of the plate. The work carried out by Sabbagh et al. [118] is around the modeling of the interaction between a coil surrounding a ferrite core and a conductive half-plane. The resolution was made analytically where the integrals are calculated by the method of the moments. It is absolutely true that the analytical or semi-analytic solutions are very advantageous in precision and in calculation time, but they are not an easy task for complex geometries.

3.7.6 Extended finite element method

This method was developed mainly to deal with two problems of the finite elements method which are the strong refinement of the mesh in the regions of concentration, and the divergence of the nonlinear models. It is used, especially, for the treatment of crack in static loading [119], and the evaluation of some parameters of fracture mechanics like the estimation of stress intensity factors and the J-integral of the cracked plate under dynamic load [120, 121].

3.7.7 Finite element method

For the numerical resolution of partial differential equations, the finite element method is one of the most popular methods. It can be used for a wide range of real problems (linear, nonlinear, stationary, or time-variant) in any geometric domain with one, two ,or three dimensions[106]. Unlike the other methods, this approach occupies a large place in modeling and is well adapted for complex geometries. It enhances, considerably, the calculation accuracy by taking into account the different types of interpolation functions. It was applied,

in the beginning, to structural mechanics and has experienced significant developments in different scientific and industrial areas in recent decades.

The finite element method is based on the transformation of partial differential equations into a system of algebraic equations [122]. In general, the resolution by this method includes the following steps:

1. **Integral formulation:** the method is not, directly, applied to partial deferential equations but through an integral formulation equivalent to the given problem. The commonly used methods to obtain the integral formulation and the definition of the functional spaces, of eligible solutions, are the variational formulation technique and the weighted residues method.

   The variational technique of Ritz is based on an integral that depends on the unknown function and its derivatives. Often, this formulation represents the energy of the system. On the other hand, the weighted residue method makes it possible to solve, directly, the partial differential equation without having to go through a variational principle. It consists in projecting the equation to be solved on a function basis. Galerkin's method is a special case where the projection functions ψ_i are identical to the interpolation functions α_i for each element i.

   $$\psi_i(x, y, z) = \alpha_i(x, y, z) \tag{3.67}$$

   The functional of the equation f is, therefore, rewritten as:

   $$\Delta(f) = g(p_o) \tag{3.68}$$

   where Δ is the differential operator and $g(p_o)$ the known function that depends on the sources placed at point p_0 [106].

   $$R_i = \int\int_{\Omega} \alpha_i(x, y, z) \left[\Delta \left(\sum_{j=1}^{nn} \alpha_i(x, y, z) f_i \right) - g \right] d\Omega \tag{3.69}$$

   The $\alpha_i(x, y, z)$ calculated for R_i are nulls.

   In each finite element e, R_i is given by the following equation:

   $$R_i^e = \int\int_{\Omega}^{e} \alpha_i(x, y, z) \left[\Delta \left(\sum_{j=1}^{nn} \alpha_i(x, y, z) f_i \right) - g \right] d\Omega^e \tag{3.70}$$

   The global residue is given by:

   $$R_i = \sum_{e=1}^{ne} R_i^e \tag{3.71}$$

   with ne the number of finite elements on the domain Ω.

2. **Elementary matrix form:** The design of a mesh corresponds to the discretization of the field in elements on which the fields are written in terms of a finite number of freedom degrees and basic functions with local reference.
   Construction of elementary matrices for each finite element Ω_e is based on the integral forms of equation (3.70) and the elementary residue takes the following form:
   $$R_e = [K]^e(A)^e - (F)^e \tag{3.72}$$

3. **Assembly and resolution of algebraic system:** After assembly of elementary matrices, the global matrix becomes:
   $$R = [K](A) - (F) = \sum_{e=1}^{ne}[K]^e(A)^e - (F)^e = 0 \tag{3.73}$$
   with $[K]$ the discretized global matrix that contains all characteristic of the studied domain. In our case, the global unknown vector A is the magnetic vector potential and F is the global vector of source current.
   The resolution of the algebraic system (3.73) is done after introducing the boundary and the interface conditions.

3.8 Numerical implementation

We focus our study on two problems, the first one is the axisymmetric model and the second deals with the 3D modelling technique using the finite element method. In order to analyse the effect of crack angle on many electromagnetic parameters such as the magnetic vector potential and eddy current and the impedance.

3.8.1 Axisymmetric model

Many axisymmetric problems in the industrial machines can be treated. As example, Figure 3.5a shows a rod with an internal and oriented crack, inspected by coil with rectangular section. Due to the symmetric nature of this problem, we can limit our study on the axisymmetric plan rz illustrated in Figure 3.5b.

3.8.1.1 Integral formulation

In the axisymmetric case, we apply the Galerkin's method to equation (3.43) and we introduce the following new variables [109]:

$$A = rA_0; \quad \psi_i = \alpha_i/r \tag{3.74}$$

In harmonic regime $\frac{\partial}{\partial t} = jw$, the governing equation becomes:

$$\int_{\Omega} \left(\frac{\alpha_i}{r} \left[-\frac{\partial}{\partial r} \left(\frac{1}{\mu r} \frac{\partial A}{\partial r} \right) - \frac{\partial}{\partial z} \left(\frac{1}{\mu r} \frac{\partial A}{\partial z} \right) + jw\sigma \frac{A}{r} - J_s \right] \right) d\Omega = 0 \tag{3.75}$$

with $d\Omega = 2\pi r dr dz$

Or:

$$-\int_{\Omega} \left[\frac{\alpha_i}{r} \frac{\partial}{\partial r} \left(\frac{1}{\mu r} \frac{\partial A}{\partial r} \right) \right] d\Omega - \int_{\Omega} \left[\frac{\alpha_i}{r} \frac{\partial}{\partial z} \left(\frac{1}{\mu r} \frac{\partial A}{\partial z} \right) \right] d\Omega + \int_{\Omega} \left[\frac{\alpha_i}{r} jw\sigma \frac{A}{r} \right] d\Omega - \int_{\Omega} \left[\frac{\alpha_i}{r} J_s \right] d\Omega = 0 \tag{3.76}$$

The integration by parts generates a simpler form that has integral boundaries and explain the natural boundary conditions:

$$\begin{aligned} &\frac{1}{\mu} \int_{\Omega} \left[\frac{\partial \alpha_i}{\partial r} \frac{\partial A}{\partial r} \right] \frac{dr dz}{r} + \frac{1}{\mu} \int_{\Omega} \left[\frac{\partial \alpha_i}{\partial r} \frac{\partial A}{\partial z} \right] \frac{dr dz}{r} - \frac{1}{\mu} \int_{\Gamma} \left[\frac{\partial A}{\partial r} \alpha_i cos(n,r) \right] \frac{d\Gamma}{r} \\ &- \frac{1}{\mu} \int_{\Gamma} \left[\frac{\partial A}{\partial z} \alpha_i cos(n,z) \right] \frac{d\Gamma}{r} + \int_{\Omega} \alpha_i jw\sigma A \frac{dr dz}{r} - \int_{\Omega} \alpha_i J_s dr dz = 0 \end{aligned} \tag{3.77}$$

$$\begin{aligned} &\frac{1}{\mu} \int_{\Omega} \left[\frac{\partial \alpha_i}{\partial r} \frac{\partial A}{\partial r} + \frac{\partial \alpha_i}{\partial r} \frac{\partial A}{\partial z} \right] \frac{dr dz}{r} - \frac{1}{\mu} \int_{\Gamma} \left[\frac{\partial A}{\partial r} \alpha_i cos(n,r) \right] \frac{d\Gamma}{r} \\ &- \frac{1}{\mu} \int_{\Gamma} \left[\frac{\partial A}{\partial z} \alpha_i cos(n,z) \right] \frac{d\Gamma}{r} + \int_{\Omega} \alpha_i jw\sigma A \frac{dr dz}{r} - \int_{\Omega} [\alpha_i J_s] dr dz = 0 \end{aligned} \tag{3.78}$$

with $Cos(n,r)$ and $Cos(n,z)$ the cosine directors at each point of the boundary or the interface between regions of the studied system. We can rewrite the equation (3.78) in the following form:

$$\frac{1}{\mu} \int_{\Omega} [grad(\alpha_i) grad(A)] \frac{dr dz}{r} - \frac{1}{\mu} \int_{\Gamma} [(grad(A)n)\alpha_i] \frac{d\Gamma}{r} + \int_{\Omega} [\alpha_i jw\sigma A] \frac{dr dz}{r} - \int_{\Omega} [\alpha_i J_s] dr dz = 0 \tag{3.79}$$

where n is the normal unit vector at the considered point from the boundary Γ.

In the discretization process, the interpolation function, of the first order triangular element, is:

$$\alpha_i = \frac{1}{2\Delta^e} (a_i + b_i r + c_i z) \tag{3.80}$$

with $i = 1, 2, 3$ the node index of an element e and Δ^e the area of that element.

Boundary conditions: The term $\frac{1}{\mu} \int_{\Gamma} [(grad(A)n)\alpha_i] \frac{d\Gamma}{r}$ expresses the natural boundary condition of Neumann type. In the case of Dirichlet conditions ($A = C^{te}$) or homogeneous Neumann this term is canceled in the symmetric axis.

3.8.1.2 Matrix formulation

Using the interpolation functions and the discretization of the magnetic potential vector A, the governing equation of the electromagnetic system becomes:

$$\sum_{j=1}^{n} \frac{1}{\mu} \int_{\Omega} \left(grad(\alpha_i) grad(\alpha_j A_j) + jw\sigma\alpha_i\alpha_j A_j \right) \frac{drdz}{r} = \int_{\Omega} [\alpha_i J_s] drdz \tag{3.81}$$

with $i = 1, ..., n$ and n the total number of nodes.
By extending the equation (3.76) for all nodes, we obtain the following global algebraic equation:

$$([M] + jw[L])\,(A) = (F) \tag{3.82}$$

with the elementary matrices and vectors given as:

$$M_{ij} = \frac{1}{\mu} \int_{\Omega} grad(\alpha_i) grad(\alpha_j) \frac{1}{r} drdz = \frac{1}{\mu R_{eq}} \int_{\Omega} grad(\alpha_i) grad(\alpha_j) drdz \tag{3.83}$$

$$L_{ij} = \int_{\Omega} \sigma\alpha_i\alpha_j \frac{1}{r} drdz = \frac{1}{R_{eq}} \int_{\Omega} \sigma\alpha_i\alpha_j drdz \tag{3.84}$$

$$F_i = \int_{\Omega} \alpha_i J_s \frac{1}{r} drdz \tag{3.85}$$

R_{eq} is the average radius of the element e given by:

$$R_{eq} = \frac{r_1 + r_2 + r_3}{3} \tag{3.86}$$

with r_1, r_2, r_3 the distances between the three nodes of an element e and its center.
After determining the magnetic vector potential A for all the nodes, the other parameters such as the magnetic flux density B, magnetic field H, the eddy current J and the sensor impedance Z can be determined. The eddy current testing depends on the change in the sensor impedance when a fault is occurred. The calculation of this impedance is made in two ways either from the vector potential or from a voltage source. In our case, we prefer to calculate the impedance from the vector potential due to the fact that the system is supplied by a current source.

3.8.2 3D model

A 3D numerical simulation of non-destructive testing using eddy current based on finite elements is developed in this section. The simulation is based on an example of a crack occurred in a plate supposed to be composed of homogeneous materials. This is the investigated situation to validate the proposed approach. An illustration, of this situation, is given in Figure

3.10 where the exciting current circulating in the coil produces an electromagnetic field that leads in its turn to two electromagnetic phenomena; the dynamic magnetic fields and the induced current.

The magneto-dynamic equations, to be solved, are based on the formulation $\overrightarrow{A}-V$ obtained

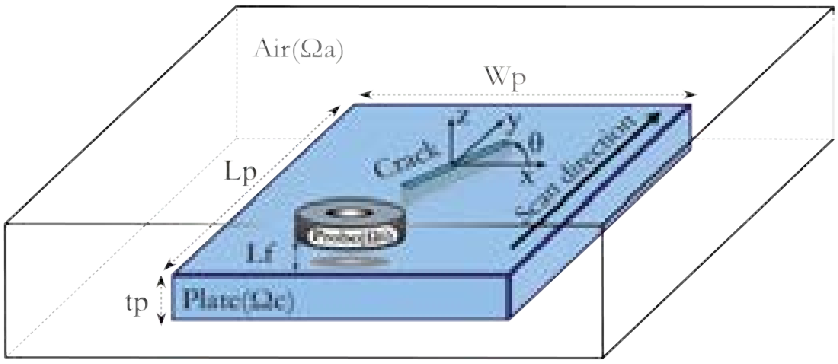

Figure 3.10: Cracked plate with multi-turn excitation coil.

as follow [123, 107]:

$$\nabla(\frac{1}{\mu}\nabla\overrightarrow{A})-\nabla(\upsilon_p\nabla\overrightarrow{A})=\begin{cases}0 & in \quad \Omega_a\\ \overrightarrow{J}_s & in \quad \Omega_i\\ j\omega\sigma(\overrightarrow{A}+\nabla V) & in \quad \Omega_c\end{cases} \tag{3.87}$$

$$\nabla\cdot(j\omega\sigma(\overrightarrow{A}+\nabla V))=0 \tag{3.88}$$

where,

υ_p is the penalty term with the same dimension as the magnetic reluctivity($\frac{1}{\mu}$), it is used as a term to include the Coulomb gauge ($\nabla\overrightarrow{A}=0$) in the aim to fix the scalar function and the unicity of the solution. Ω_i is the inductor region (probe), Ω_c the studied plate, Ω_a the non-conductive region(air), $j\omega$ the derivative operator replacing the term $\frac{\partial}{\partial t}$, $\overrightarrow{A}$ the magnetic vector potential (Wb/m), V the modified electrical scalar potential obtained from $\nu=j\omega V$, where ν is the electrical scalar potential (Volt) and $\overrightarrow{J}_s$ the source current density (A/m^2). Based on the application of two methods on equations (3.87) and (3.88), the first one is the well know mathematical method of Boris Galerkin which allows converting the continuous operator problem to a discrete one. This is achieved through the linear constraints: the weight functions $\overrightarrow{N}_l^s$, and α_l at node l. The second one, is the weighted residual method developed to obtain approximate solution for the differential equations. These equations can

be transferred to the integral $\overrightarrow{A} - V$ formulation as follows[124, 125, 126]:

$$\int_{\Omega}\left[\frac{1}{\mu}(\nabla\wedge\overrightarrow{N}_l^s)(\nabla\overrightarrow{A})+\upsilon_p(\nabla.\overrightarrow{N}_l^s)(\nabla\overrightarrow{A})\right]d\Omega+\int_{\Omega}\left[j\omega\sigma(\overrightarrow{N}_l^s\overrightarrow{A}+\alpha_l V)\right]d\Omega+ \oint_{\Gamma}\overrightarrow{N}_l^s\frac{1}{\mu}(\nabla\wedge\overrightarrow{A})d\Gamma=\int_{\Omega}(\overrightarrow{N}_l^s\overrightarrow{J}_s)d\Omega \quad (3.89)$$

$$\int_{\Omega}j\omega\sigma\left[\nabla(\overrightarrow{N}_l^s\overrightarrow{A}+\alpha_l\nabla V)\right]d\Omega=0 \quad (3.90)$$

For an element s of the considered model with m nodes and three components $(A_x^s, A_y^s A_z^s)$ of the magnetic vector potential $\overrightarrow{A}$ and the electrical scalar potential V can be calculated, based on nodal approximation functions, as follows [107, 127]:

$$A^s=\sum_{l=1}^{m}N_l^s A_l^s=\begin{bmatrix}N_1^s & N_2^s & \dots N_m^s\end{bmatrix}\begin{bmatrix}A_1^s\\A_2^s\\\vdots\\A_m^s\end{bmatrix} \quad (3.91)$$

where each components of A^s can be obtained as: $A_r^s=\sum_{l=1}^{m}N_{r,l}^s A_{r,l}^s$.

$$V^s=\sum_{l=1}^{m}\alpha_l^s V_l^s \quad (3.92)$$

with, $r=x,y,z$; $N_l^s=[N_{x,l}^s \quad N_{y,l}^s \quad N_{z,l}^s]^T=[1 \quad 1 \quad 1]\alpha_l$ the vector shape function of node l, α_i a scalar shape functions of node l, $l\in[1, \quad m]$ the number of the concerned node in the element s, m the total node in the element s, $A_{r,l}^s$ the magnetic component of vector potential at node l following r coordinate, V_l the electrical scalar potential at node l, V^s the resulting electrical scalar potential of element s, A_r^s the resulting magnetic component of vector potential of element s following r coordinate and A^s the resulting magnetic vector potential of element s. It is worth to say that, these nodal approximation functions associated with each node are entirely defined by the x,y,z coordinates of the corresponding mesh nodes.

By substituting equations(3.92) and (3.91) in (3.90) and (3.89), the elementary algebraic matrix system becomes [128]:

$$[K^s]X^s=F^s \quad (3.93)$$

with,

$$X^s=\begin{bmatrix}A_x^s\\A_y^s\\A_z^s\\V^s\end{bmatrix} \quad (3.94)$$

$$F^s = \begin{bmatrix} F_x^s \\ F_y^s \\ F_z^s \\ F_V^s \end{bmatrix} \tag{3.95}$$

$$[K^s] = \begin{bmatrix} K_{xx} + M & K_{xy} & K_{xy} & G_{xV} \\ K_{yx} & K_{yy} + M & K_{yz} & G_{yV} \\ K_{zx} & K_{zy} & K_{zz} + M & G_{zV} \\ G_{Vx} & G_{Vy} & G_{Vz} & G_{VV} \end{bmatrix} \tag{3.96}$$

The integral terms, in the elementary algebraic system, are given as follows:

$$K_{r,q}^{l,k} = \int_\Omega \left[\frac{1}{\mu} (\nabla \wedge N_l)(\nabla \wedge N_k) + \upsilon_p (\nabla . N_l)(\nabla . N_k) \right] d\Omega \tag{3.97}$$

$$M^{l,k} = \int_\Omega \left[j\omega\sigma (N_l N_k) \right] d\Omega \tag{3.98}$$

$$G_{V,r}^{l,k} = \int_\Omega \left[j\omega\sigma (N_l \nabla \alpha_k) \right] d\Omega \tag{3.99}$$

$$G_{r,V}^{l,k} = \int_\Omega \left[j\omega\sigma (N_k \nabla \alpha_l) \right] d\Omega \tag{3.100}$$

$$G_{V,V}^{l,k} = \int_\Omega \left[j\omega\sigma (\nabla \alpha_l \nabla \alpha_k) \right] d\Omega \tag{3.101}$$

$$F^s = \int_\Omega \left[N_l J_s \right] d\Omega \tag{3.102}$$

with $r \in \{x, y, z\}$ and $q \in \{x, y, z\}$.

After assembling the elementary system (3.93) for all finite elements of the meshed 3D model we obtain the following global algebraic system:

$$[K](X) = (F) \tag{3.103}$$

with X a vector contains the potential magnetic vector A and the electrical scalar potential V for each node of the studied model. The resolution of this system gives the potential magnetic vector A and, thus, the magnetic field density B and the eddy current J.

3.9 Impedance calculation

After calculating the values of the vector potential magnetic in each node of the meshed system, we can calculate the impedance of the coil using one of two commonly used methods: the direct technique or the energy method [99, 128].

Direct method

The impedance of a single turn of coil with radius R powered by an alternative current is given by [99]:

$$Z = \frac{V}{J_s} \tag{3.104}$$

where V is the induced tension in the coil expressed as:

$$V = -\int_L Edl \tag{3.105}$$

with L the length of the turn.
The electric field intensity E is given by:

$$E = -grad(V) - \frac{\partial A}{\partial t} \tag{3.106}$$

In harmonic regime $\frac{\partial}{\partial t} = jw$ and consedring that the induced voltage is independent of the scalar potential $grad(V) = 0$, the last equation becomes:

$$E = -jwA \tag{3.107}$$

By replacing the equation (3.107) into (3.105) we obtain:

$$V = jw\int_L Adl \tag{3.108}$$

From the equations (3.104) and (3.108), the impedance of the coil is given by:

$$Z = \frac{jw}{J_s}\int_L Adl \tag{3.109}$$

and for a single turn of radius r, the impedance is:

$$Z = R + jX = j\frac{2\pi wrA}{J_s} \tag{3.110}$$

The impedance of the sensor(coil) is composed of two parts, real part which is the resistance and an imaginary one which is the reactance. The impedance of the coil is calculated approximately using the finite element method. Indeed, the multi-turn coil region is discretized by small triangular elements where each one includes certain number of turns. For each turn of an element i, the magnetic vector potential is noted by the central value A_{ci} while the radius is noted by the central value R_{ci}.
From the equation (3.110), the impedance for each turn inside the element i is given by [99]:

$$Z = R + jX = j\frac{2\pi wr_{ci}A_{ci}}{I_s} \tag{3.111}$$

If N_t is the total number of the coil turns, N_s the density turns of the element $i(turns/m^2)$ and a_i the area of element i, then the total impedance of an element i is given by:

$$Z = j\frac{2\pi w r_{ci} A_{ci} N_s a_i}{I_s} \tag{3.112}$$

and the impedance of the multi-turn coil is:

$$Z = j\frac{2\pi w N_s}{I_s}\sum_{i=1}^{N_c} a_i r_{ci} A_{ci} \tag{3.113}$$

where N_c is the total number of elements in the coil.

Energetic method

The impedance variation can be determined by calculating the magnetic energy W_m stored in the entire space and the joule losse P_J is [107, 129]:

$$W_m = \frac{1}{2}\int_{space}\frac{1}{\mu}|B|^2 dv \tag{3.114}$$

$$P_J = \frac{1}{2}\int_{coil}\frac{1}{\sigma}|J|^2 dv \tag{3.115}$$

B and μ are respectively the magnetic induction and the magnetic permeability. J and σ denote, respectively, the density of eddy currents and the electrical conductivity.
The integral expressions can be translated in terms of finite elements to the following sums:

$$W_m = \sum_{i=1}^{N}\frac{1}{2}(B_{ri}^2 + B_{zi}^2)V_i \tag{3.116}$$

$$P_J = \sum_{i=1}^{N_c} P_j^i = \sum_{i=1}^{N_c} V_i \omega^2 \sigma A_{ci}^2 \tag{3.117}$$

where V_i is the volume of element i, N the total number of elements in the whole system and N_c the number of elements in the coil. The equivalent expression of the resistance R and the reactance X are given, respectively, by the joule resistance and the magnetic energy [127, 130]. That is:

$$R = \frac{P_J}{J_s^2} \tag{3.118}$$

$$X = \frac{2\omega W_m}{J_s^2} \tag{3.119}$$

$$Z = R + jX \tag{3.120}$$

J_s and ω are, respectively, the excitation current and its pulsation.

Impedance of differential sensor

The differential impedance of a sensor linked to eddy currents can be calculated by the magnetic vector potential at each center of the triangle. Hence, the impedance of a differential sensor is given by:

$$Z = j\frac{2\pi\omega N_t}{J_s}\left[\sum_{i=1}^{N_a} a_i r_{ci} A_{ci} - \sum_{i=1}^{N_b} a_i r_{ci} A_{ci}\right] \tag{3.121}$$

N_a and N_b are, respectively, the number of finite elements of the coils a and b of the differential sensor.

3.10 Conclusion

This chapter is composed of two parts, in the first one the important formulations governing the magneto-dynamic problem that govern the eddy current testing process are presented. After that, the simplifying hypotheses, the boundary and the continuity conditions are given. In the second part, the finite element method is selected and used to implement the proposed magneto-dynamic model for our study. The finite element formulation is established for an axisymmetric model and for a 3D model. This is led to a system of algebraic equations and its resolution gives the main parameter which is the magnetic potential vector which in its turn allows us the calculation of other crucial parameters such as the magnetic flux density, the eddy current and the impedance of the coil.

The validation of the proposed approach and the evaluation of their performance are the main objective of the next chapter. It deals with the simulation results focused on the resolution of the algebraic system and the analysis of the influence of the crack orientation on the impedance of the coil as well as on the other parameters of the system.

Chapter 4

Results and interpretations

4.1 Introduction

The Non-Destructive Testing by Eddy Curren (NDT-EC) uses several types of coils to inspect invisible flaws in the tested component. The scanning is done by moving the coil above the component and receiving the electromagnetic signals. They indicate many information about the flaws like position, length, width and their orientation. The main objective of this chapter is the identification of a crack and its orientation, during the scanning operation, based of the received magnetic flux density B, eddy current J and the impedance Z. As a reminder, the previous studies, in this context, are mentioned in the general introduction to reduce the volume of this chapter and to ensure a minimum equilibrium between chapters. This chapter presents the fruits of our contributions. Indeed, firstly, we study the crack orientation in axisymmetric model of a rod tested by an absolute sensor. This study is done by developing a finite element code under the environment of *"Matlab"*, to prove and to estimate the effect of the crack orientation on the impedance of the absolute sensor. Then, We prove and analyze the effect of crack orientation on the output signals for the 3d model of the benchmark *"TEAM"* given in [131] and for simulation purposes we use the sophisticated software called *"Multi-physic Comsol 5.4"*. Finally, we propose the use of Harris Hawks Optimization (HHO) technique to estimate the best crack angle corresponding to a given value of the impedance. This last contribution is proposed as an alternative method to obtain information about hidden cracks in case of that the direct methods fail to provide this information.

4.2 Axisymmetric model

In this section we study numerically the crack orientation in a portion of rod investigated by an absolute sensor. A finite element code is elaborated in *Matlab* to simulate the non destructive testing by eddy current, and to investigate the crack orientation and to analyze its effect on the electromagnetic signals.

4.2.1 Description of the model

From many axisymetric problems, we choose the quarter symmetric of rod investigated by absolute sensor as illustrated in Figure 4.1. The simulation uses a rectangle of air with the dimensions $La = 10mm, Wa = 6mm$ around the model, in order to modulate the propagation of electromagnetic waves through the air and their effect on the tested plate. The studied

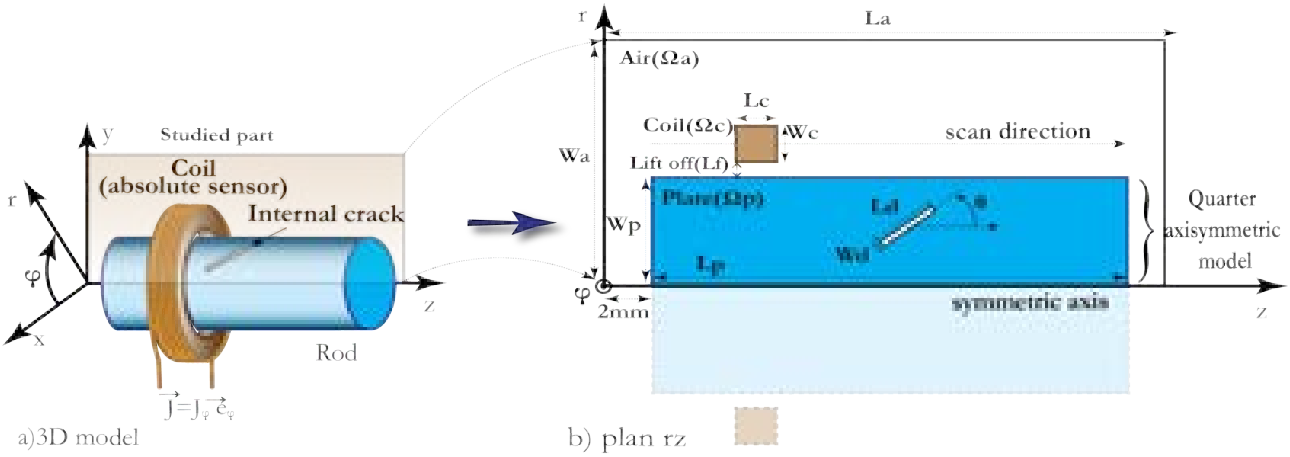

Figure 4.1: Quarter axisymmetric model of the tested rod using zn absolute sensor.

part of the rod is considered as an aluminum plate specimen containing an oriented internal crack with dimensions $Ld = 4mm, Wd = 2mm$ as shown in Figure 4.1b. The parameters of the plate and the coil are presented, respectively, in Table 4.1 and Table 4.2 [99]. To ensure the excitation of the coil, an alternative current is used $J_s = I_0 cos(2\pi f)$, with $I_0 = 1A$ its amplitude and $f = 1kHz$ its frequency.

4.2.2 Flowchart of the developed code

We have developed a code, under the *Matlab* environment to solve the governing equation of the magneto dynamic problem for the aforementioned axisymmetric model. The scan operation is done by moving the coil from $z_i = 40mm$ to $z_f = 60mm$ by step $dz = 0.5mm$. To

Parameter	Value
Length Lp (mm)	60
Width Wp (mm)	5
Electrical conductivity $\sigma(S/m)$	36.710^6
Relative permeability $\mu_r(Unitless)$	1

Table 4.1: Electric parameters and dimensions of the studied part of the rod

Parameter	Value
Length Lc (mm)	4
Width Wc (mm)	3.2
Lift off Lf (mm)	0.5
Wire diameter (mm)	0.1
Number of turns	160

Table 4.2: Parameters of the absolute sensor

analyze the crack orientation we start with $\theta = 0°$ and end with $\theta = 90°$ passing through the angles $\theta = 15°, 30°, 45°, 60°, 75°$. This resolution is done by using the finite element method and the flowchart of Figure 4.2 illustrates all steps of the proposed resolution process.

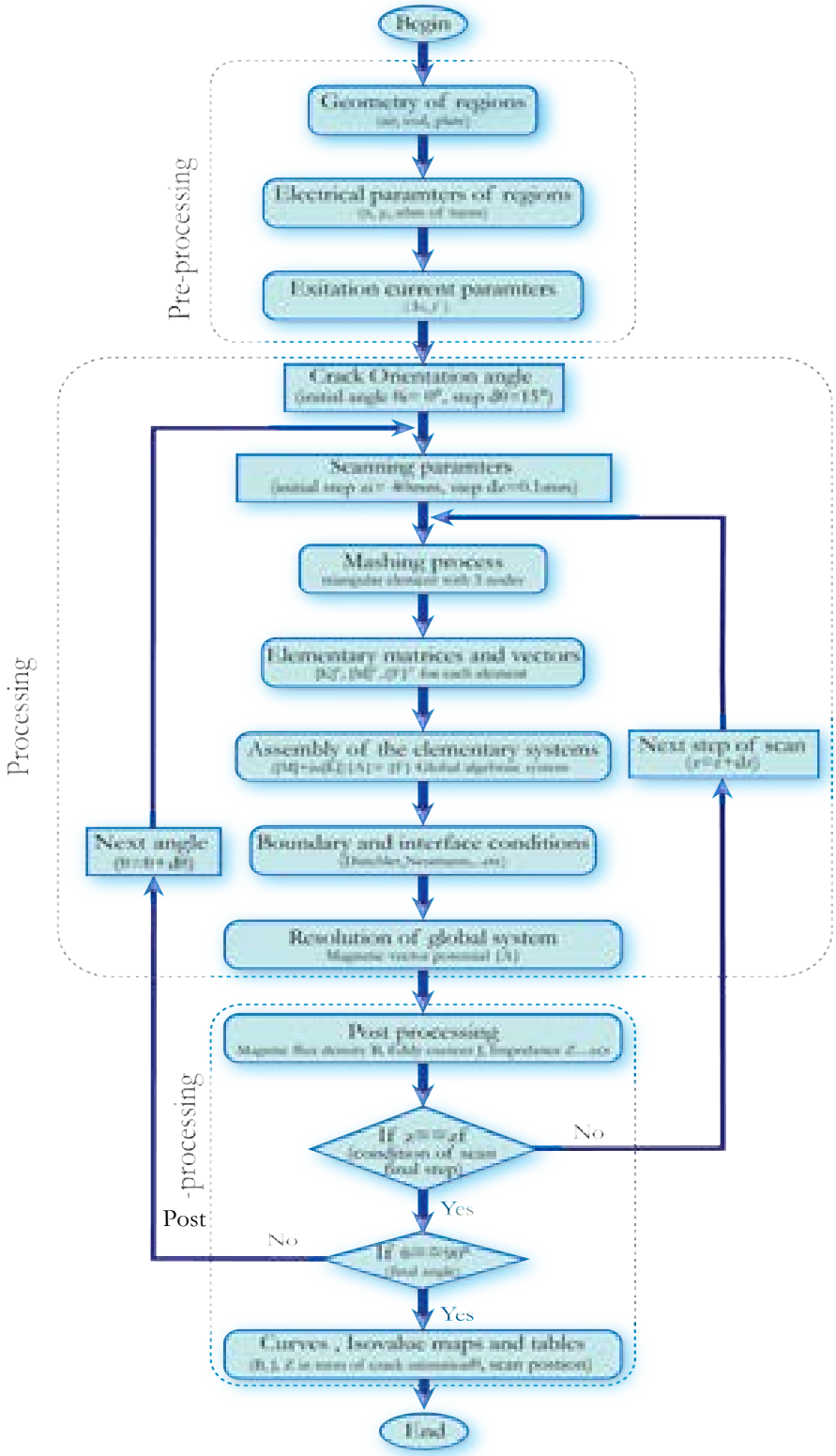

Figure 4.2: Flowchart of the elaborated code for axisymmetric model.

4.2.3 Meshing process

The adopted meshing , in this model, is a triangular element of three nodes as shown in Figure 4.3. This type is the best convenient element for complex geometries, dynamic problems and those containing moving parts (sensor in our case) that needs meshing operation again. The meshing is repeated automatically in each step of scanning using the PDE toolbox built in *Matlab 2015*. The meshing is refined around the probe and the crack; zones with a concentration of magnetic field and with sharp edge.

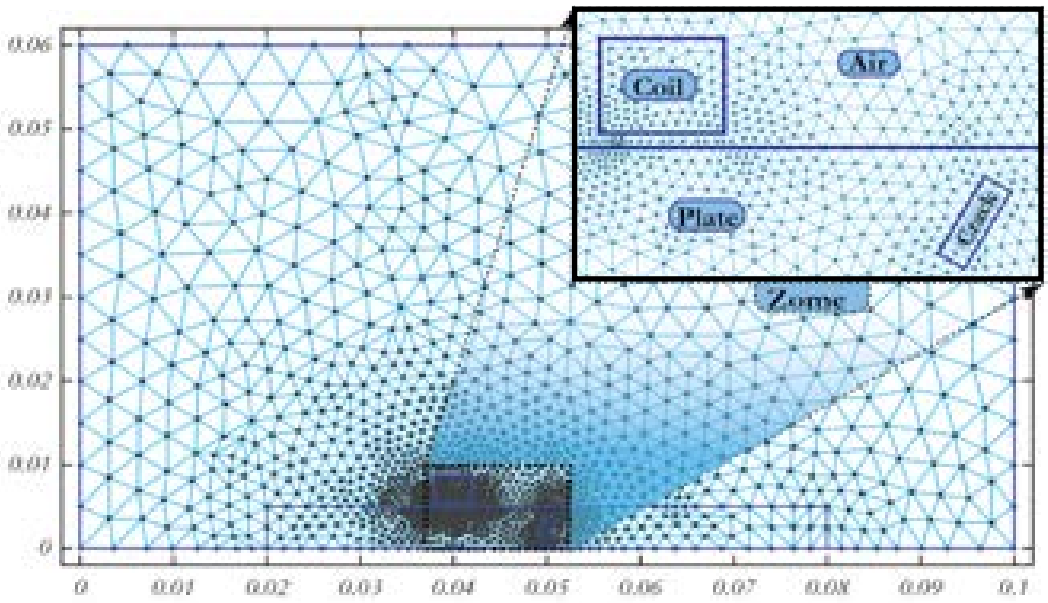

Figure 4.3: Automatic triangular meshing.

4.2.4 Results and interpretations

4.2.4.1 Magnetic potential vector A

The real and the imaginary parts of the magnetic potential vector A, at the middle of the scanned area, are given in Figure 4.4. These results are taken, with coil over the crack, for three orientation angles of the crack $\theta = 0°, 45°, 90°$. Through this isovalue maps, we notice that the imaginary part decreases with the increase of the crack angle while the real part, practically, remains unchanged.

To clarify more accurately the effect of the crack orientation, the Figure 4.5 shows the variation of the maximum value of A in terms of the crack orientation angle. The maximal real and imaginary parts of A respond inversely with crack angle variation. On the angle

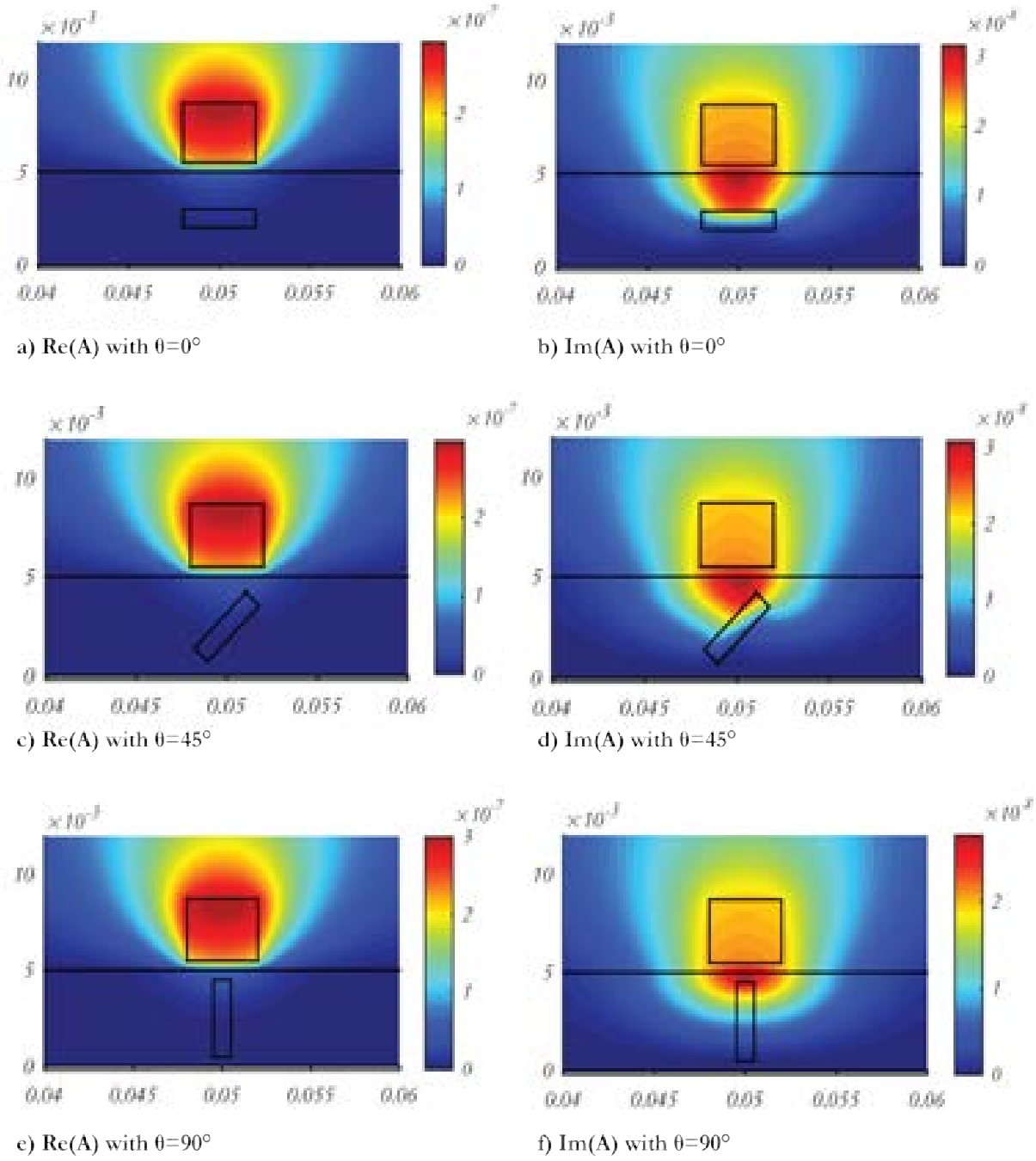

Figure 4.4: Real and imaginary parts of A for $\theta = 0°, 45°, 90°$.

interval $[0°, 90°]$, the $Re(A)$ increases approximately in a linear way while $Im(A)$ decreases relatively by an exponential way, and vice versa for the interval $[90°, 180°]$. All of these facts can explained by the expression of A and the geometry of the model. Indeed, from equation

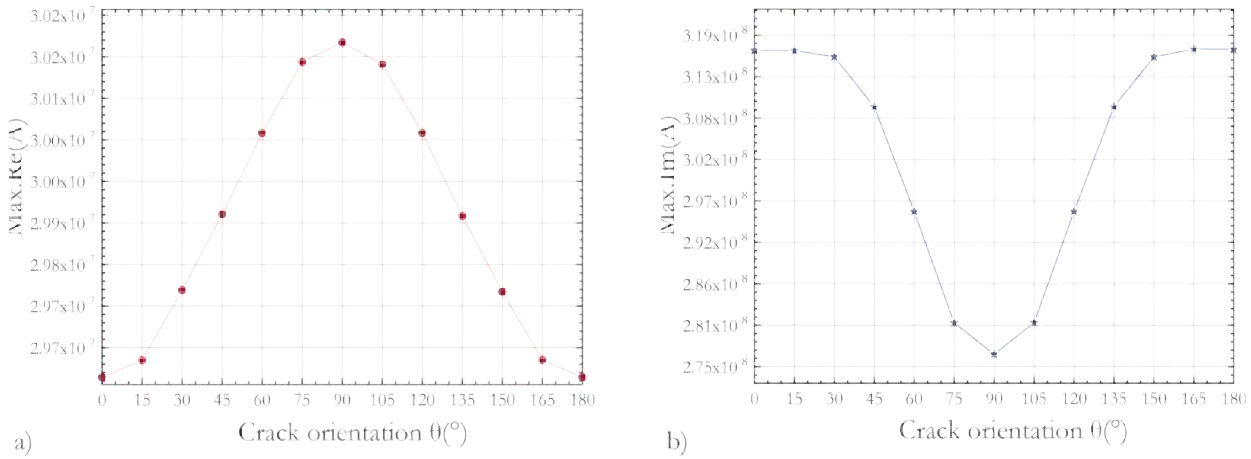

Figure 4.5: Maximum of the magnetic potential vector with crack orientation: a)real part, b)imaginary part.

(3.82) we can get the expression of A as:

$$(A) = \frac{(F)}{[M] + jw[L]} \tag{4.1}$$

According to the expressions of the matrices M, L and F, mentioned in the previous chapter, we can symbolized them as linear functions in term of the inputs of the problem as:

$$A = \frac{g(J_s)}{h(\frac{1}{\mu_{under}}) + jm(f, \sigma_{under})} \tag{4.2}$$

with g, h, m linear functions in terms of the current source J_s, the frequency f, and the inverse of the permeability $\frac{1}{\mu_{under}}$, the conductivity σ_{under} of the plate portion between the sensor and internal crack.

As J_s and f are constants inputs and can not be effected by the geometric change resulting from the crack orientation, the A depends, linearly, only on $\frac{1}{\mu_{under}}$ and σ_{under}. Another approximation of A can be expressed as:

$$A = C_1(\frac{1}{\mu_{under}}) + jC_2\sigma_{under} \tag{4.3}$$

The crack can be considered as absence of material or as region with lower conductivity and permeability than of the plate. Qualitatively speaking, when crack rotate from 0° to 90° that leads to the increase of the permeability μ_{under} and decrease of the conductivity σ_{under} of region between crack and sensor. This means increase of the real part of expression of (4.3) and decrease of its imagery part. It goes without saying that C_1 and C_2 are constants just depend to the interpolation function.

Quantitatively speaking, we can estimate the following relative change of $Im(A)$ and $Re(A)$ on the whole range of the crack orientation area as follows:

$$\Delta Im(A) = (Max.Im(A) - Min.Im(A)) * 100/Min.Im(A) = 14.38\% \tag{4.4}$$

$$\Delta Re(A) = (Max.Re(A) - Min.Re(A)) * 100/Min.Re(A) = 1.96\% \tag{4.5}$$

where values of $Max.Im(A), Min.Im(A)$ and $Max.Re(A), Min.Re(A)$ are taken from the Figure 4.5.

The imaginary part of A is more affected by the crack angle than the real part. That is due to, on one hand, the fact that the imaginary part $Im(A)$ depends on the conductivity of the region between crack and sensor. the conductivity of this region decreases strongly whenever including more finite elements of crack (elements have no conductivity) during the carck rotation. On the another hand, the real part $Re(A)$ depends on the inverse of permeability of the same region. This permeability increases slightly when including more finite elements of the crack during the its rotation.

4.2.4.2 Mesh study

The mesh operation using the PDE toolbox of Matlab, provides, as output, the following matrix:

- $p(2, nn)$: A point matrix that contains two rows for x and y coordinates with nn is the total number of nodes of the mesh.
- $e(6, ned)$: The edge matrix with the indices of the initial and final points in the first and second rows, the initial and final parameter values in the third and fourth rows, the edge segment number in the fifth row and the left- and right-hand side subdomain numbers are in the sixth and seventh rows. ned is the total number of segemnts (edges).
- $t(4, ne)$: A triangle matrix where the first three rows include counter-clockwise numbers of the corner points, the subdomain number is given in the fourth row and ne is the total number of finite elements.

Using four levels for mesh refinement, we get the result of Figure 4.6. This last presents the maximum value of real and imaginary parts of A in terms of the crack angle in the range of $[0°, 180°]$ with step of 15°. From the illustrated curves in the Figure 4.6, it is obvious that the increase of the refinement level leads to more accurate values of the maximal of A. This is due to the fact that the triangular element is more convenient for use in refinement and

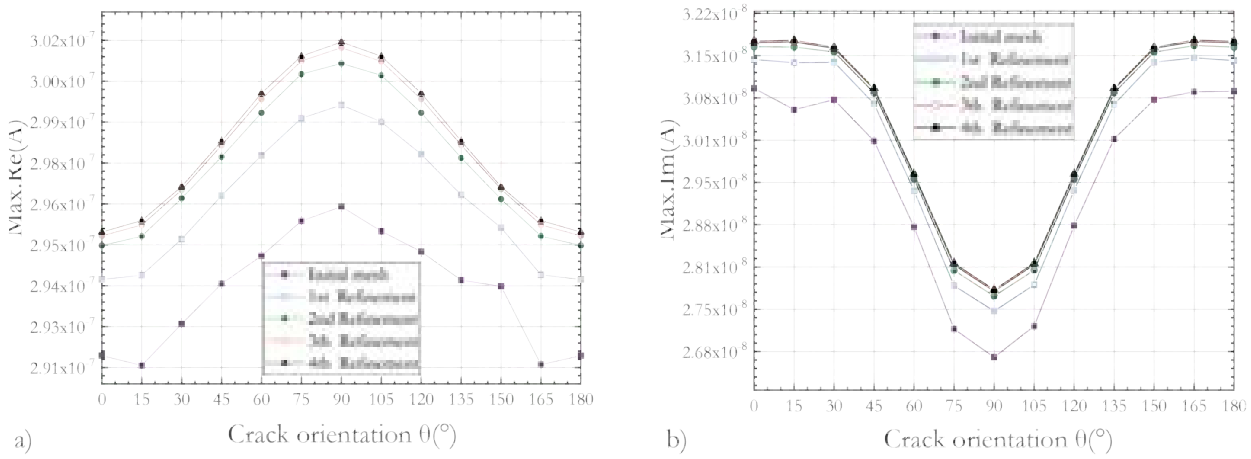

Figure 4.6: Maximum of the magnetic potential vector with four levels of mesh refinement: a)real part, b)imaginary part.

sharp edges. However, the refinement level increase are consuming in terms of computing time and allocated memory size. Thus, it is mandatory to quantify these two parameters for each crack orientation and for each level of mesh refinement. For this purpose, let us consider that the sensor is in the middle scan position (above the crack), and that the crack is oriented to 45°. In this situation, the Figure 4.7 illustrates the computing time and number of nodes according to the initial and the four automatic mesh refinement. Values are obtained from a PC with the following characteristics: *AMD Ryzen 7 2700 Processor (3.2 Ghz) and RAM of 16 Go* . From the Figures 4.6 and 4.7, we can remark that the third level of refinement gives

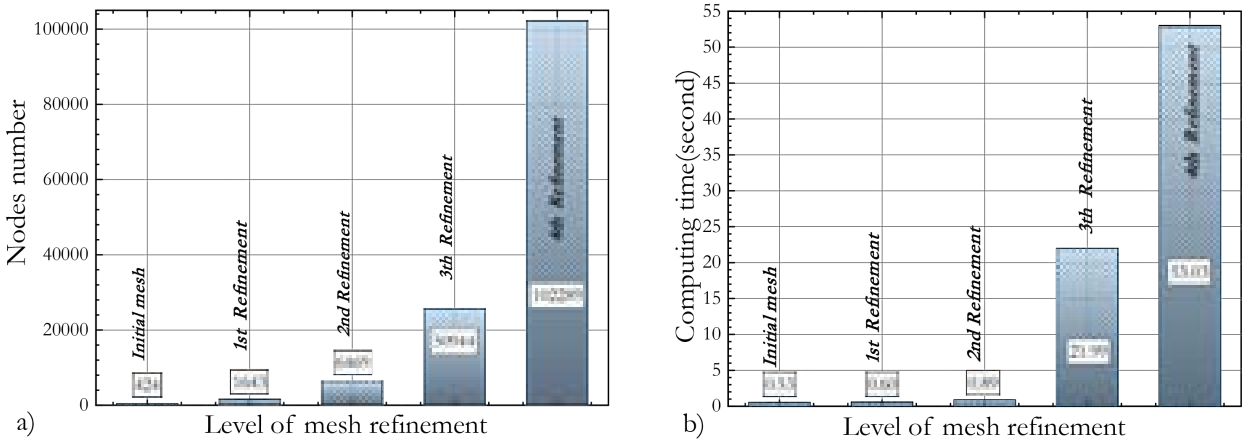

Figure 4.7: Level of refinement with: a)memory size, b)computing time.

closer results to those of the fourth level with less computing time and allocated memory size. Hence, the optimal choice and the best trade-off between accuracy and computing

time/memory size is the third level of refinement.

Using the third refinement level (the optimal choice), the Figure 4.8 presents the number of nodes and the number of elements in term of the crack orientation angle. This figure

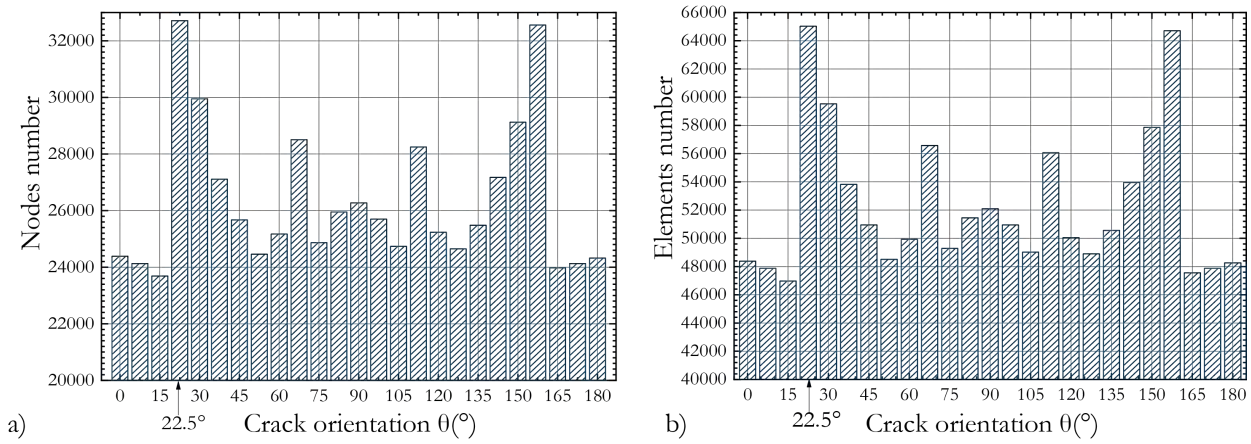

Figure 4.8: Crack orientation effect on: a)number of nodes, b)number of elements.

proves that the automatic mesh of *Matlab* increases the number of nodes and elements in some difficult configurations of the crack. Indeed, for the angle 22.5° the Figures 4.8a and 4.8b indicate that the decimal parts of the geometric parameters are affected by the mesh size under the *Matlab* environment. Hence, to deal with this drawback we developed, in this context, an enhanced version of the mesh generator. This enhanced version is used to generate all the 2D results presented in this manuscript.

4.2.4.3 Impedance plane

The Figure 4.9 shows the variation of the normalized impedance amplitude in terms of the scan step and crack orientation. The frequency is set to $f = 1000Hz$, the conductivity is $10^6 S/m$ and the relative permeability is 1 [106]. The scan begin from $40mm$ to $60mm$ with step of $0.5mm$. Under these conditions, the normalized impedance is given by:

$$|\Delta Z| = |Z| - |Z0| \tag{4.6}$$

with $Z = R+jX$ the impedance of each crack orientation and $Z0 = R0+jX0 = 0.042+j14.18$ is impedance of the perfect plate (without crack).

Interpretation notes, from the Figure 4.9, and their justifications are summarized as follows:

- The impedance increases when the sensor is near the crack position regardless of its orientation is a good indicator of the efficiency of the proposed approach. The impedance increase is due to the conductivity variation caused by the crack.

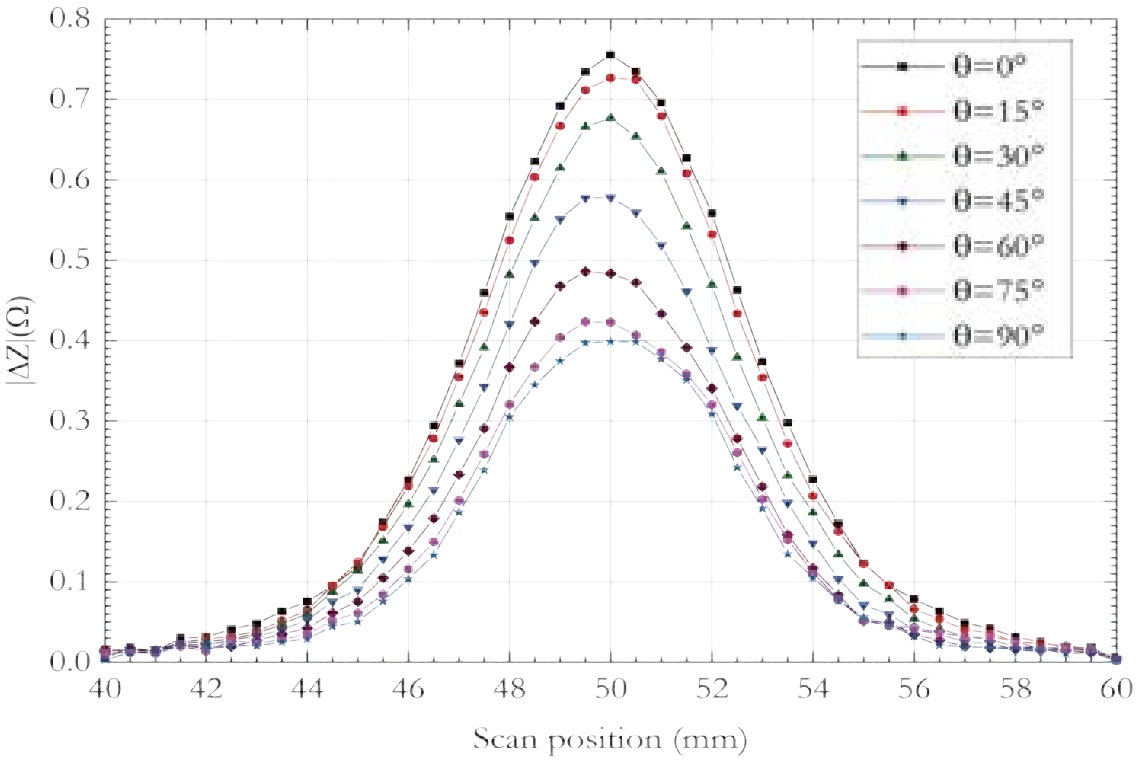

Figure 4.9: Normalized impedance amplitude in terms of crack orientation

- Almost all maximum values of the impedance are situated in the middle of the plate, which confirm the proposed approach ability to locate accurately the crack.
- The orientation angle of the crack has a significant effect on the impedance in terms of peak value and its position in the scan range. This fact is our main and important result. Indeed, the more the orientation angle increase the more the impedance peak value decrease. The reason for that, is the more the angle increase, the more the crack is approaching the sensor. Consequently, the conductivity decrease leads to the decreases the magnetic vector potential according to its expression(4.3), and its turn decrease the impedance relating to the equation (3.113).
- The peak positions are not the same due to the plate asymmetric geometry caused by crack angles except the 0° and 90° where we have a symmetric geometry based on the crack center.

The Figures 4.10 and 4.11 illustrate, respectively, the normalized resistance and reactance in terms of the crack orientation.
Results depicted in Figures 4.10 and 4.11 are fully adequate with those given in Figure 4.9 at the difference that we have, here, the resistance range is smaller nearly 20 times than the

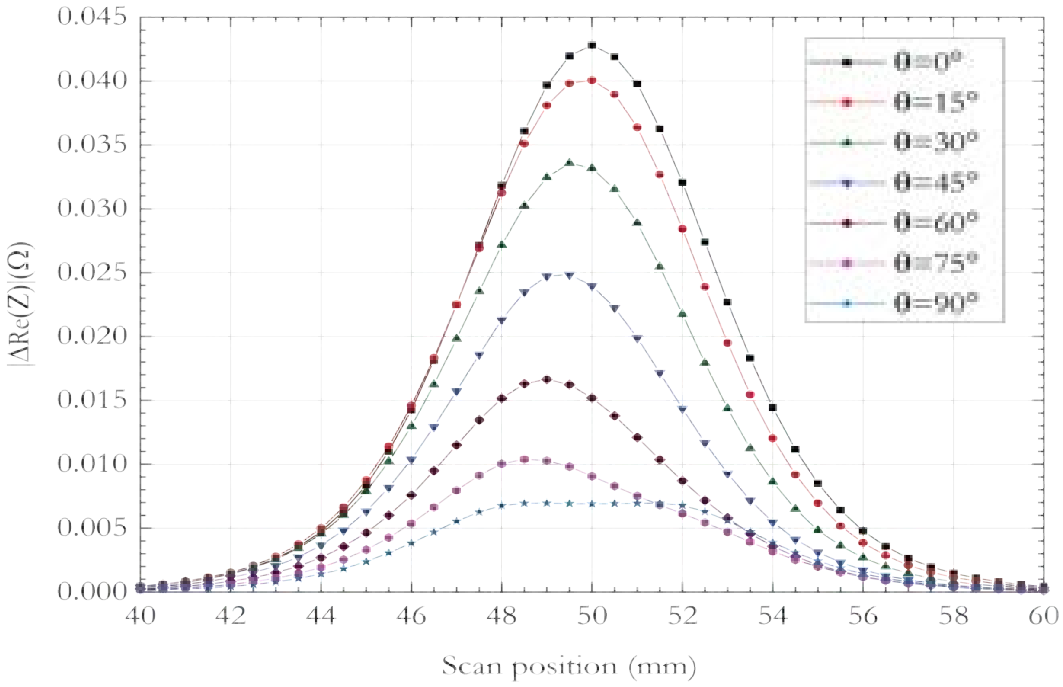

Figure 4.10: Normalized resistance in terms of the crack orientation.

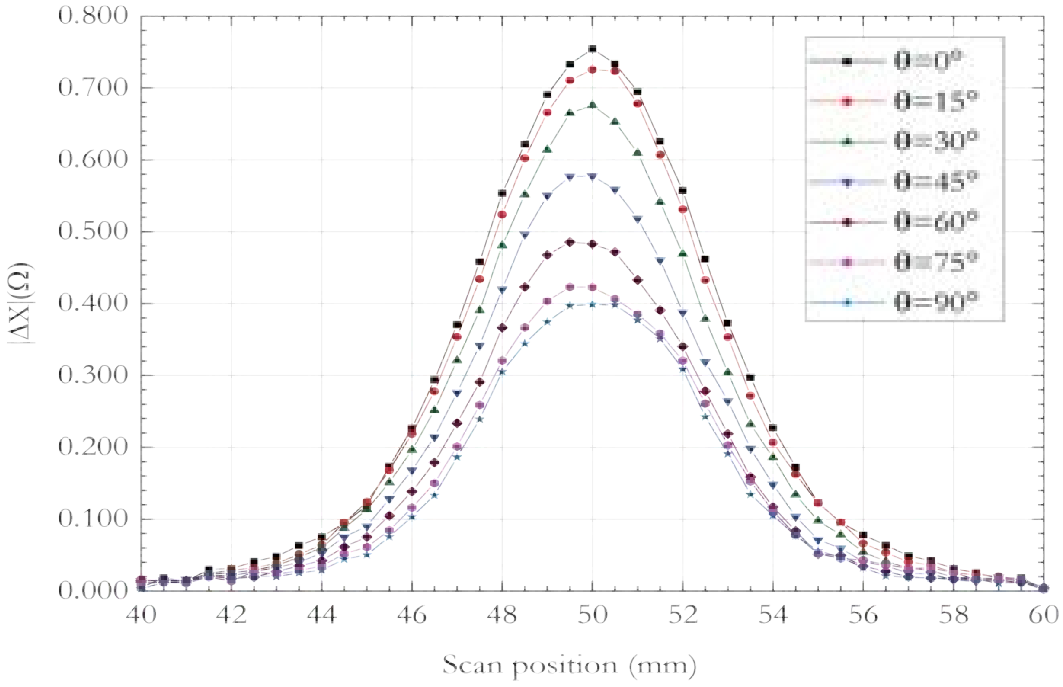

Figure 4.11: Normalized reactance in terms of the crack orientation.

reactance range. This fact can be justified by the relationship between resistance/reactance and conductivity/permeability mentioned in the previous chapter.

The signature of the absolute sensor for each crack orientation is shown in Figure 4.12.

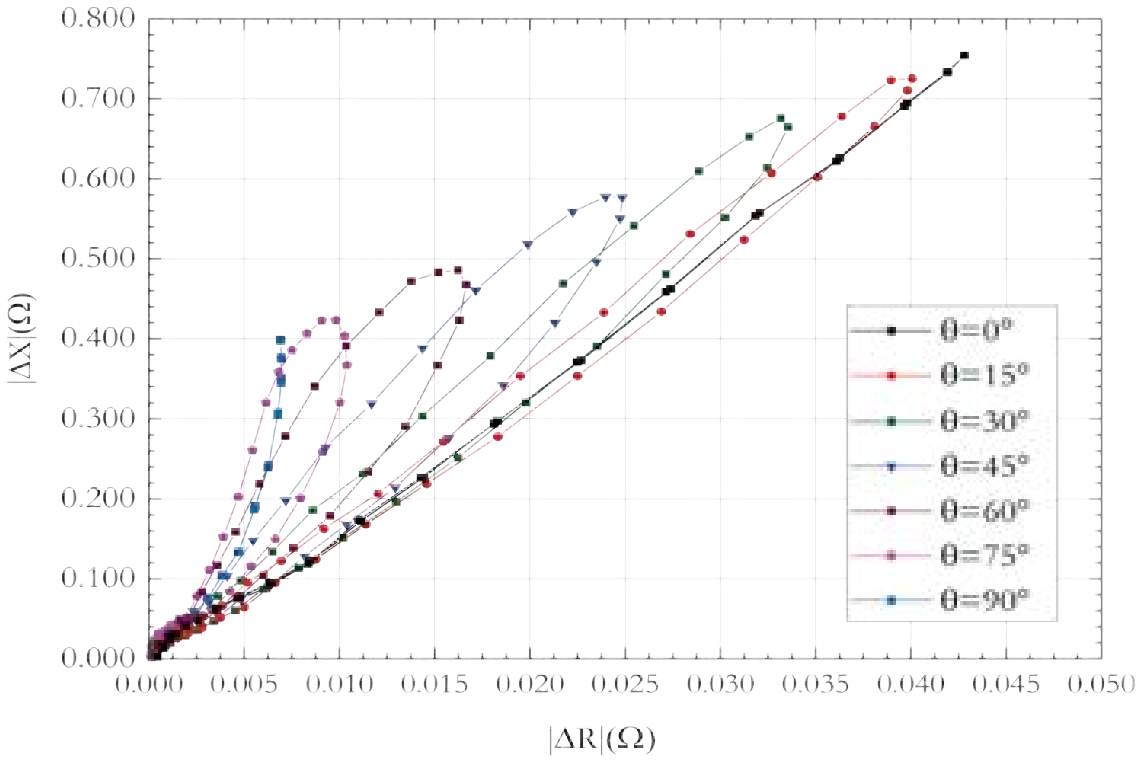

Figure 4.12: Signature of the absolute sensor for each crack orientation.

Some of the remarks, that can be extracted from this signature, are:

- The more the orientation angle is small, the more the signature is larger, linear and flattened. It is worthy to note, that the angle 0° has the biggest linear variation of the signature. This observation can be explained by the fact that for the angle 0°, the cracked plate has the more symmetric geometry. The other angles cause an asymmetric geometric and create the signatures shapes shown in Figure 4.12
- When the orientation angle goes higher, the reactance is affected more than the resistance. This is due to the relationship between reactance and permeability that is affected more by the crack than the conductivity.

4.3 3D model

This section is dedicated to the validation of the proposed approach based on the aforementioned formulation in the previous chapter. We start by a description of the model, then we give the simulation parameters and the meshing process to end with the results and their interpretations.

4.3.1 Description of the model

The proposed model is based on aluminum plate containing an arbitrarily oriented external crack which is scanned by a multi-turn excitation coil probe. To take account the real effect of the magnetic field, the proposed model is placed inside inside box of air with dimensions ($500x500x100mm$). The dimensions of the crack are defined by the length L_c, the thickness t_c, the width W_c which are taken equal to 12mm, 5mm and 0.3mm respectively as shown in Figure 4.13.

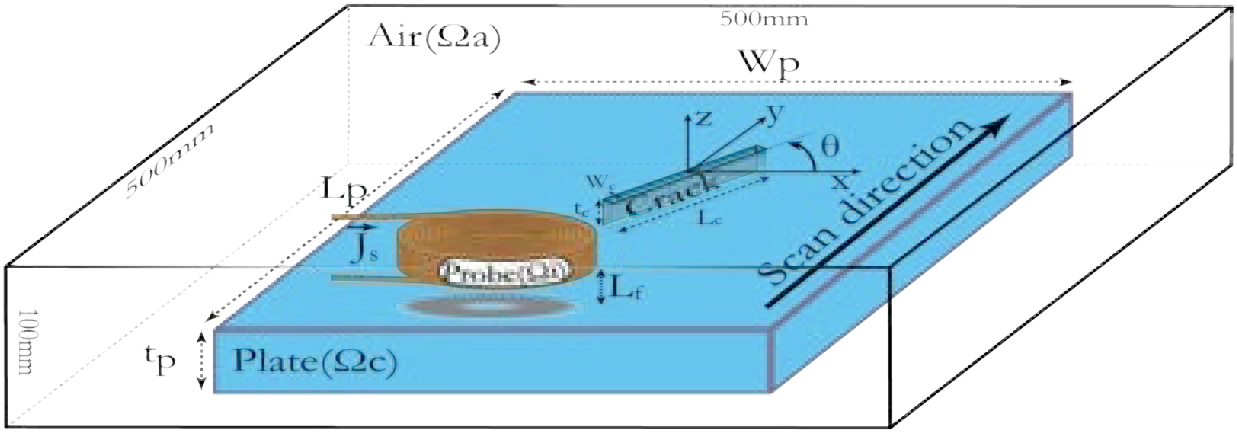

Figure 4.13: Cracked plate investigated under multi-turn excitation coil probe.

The model of this probe coil is the same model which has been used in several previous studies of many authors as a standard benchmark such as in the references [132, 133, 134]. Indeed, this model was proposed for the first time in 1988 within the famous publication of S. K. Burke from the Aeronautical Research Laboratory of the Defence Science and Technology Organisation (DSTO), Australia [131].
The characteristics of this benchmark model is presented in Table 4.3. On the other side, the plate which contains the studied crack has the characteristics presented in Table 4.4

To obtain the best choice of the probe topology, deep investigations on many existing probe topologies have been checked previously by some authors such as the figure-8-shaped probe which induces a strong Near Unidirectional Eddy Current (NUEC) area between the two coils. Unfortunately, it has not enough sensitive to the crack orientation as reported in [135]. On the other side, it has been found that the tangential and normal rectangular coil topologies induce a weak unidirectional eddy current under the coils which cannot be used for the crack orientation detection [136]. In our case, we choose the coil topology proposed

Parameter	Value
Inner radius r1 (mm)	6.15
Outer radius r2 (mm)	12.4
Height h (mm)	6.15
Lift-off Lf (mm)	1
Number of turns	3790

Table 4.3: Benchmark coil parameters proposed by S. K. Burke.

Parameter	Value
Length Lp (mm)	100
Width Wp (mm)	100
Thickness tp (mm)	12.22
Electric conductivity (S.m-1)	30.610^6
Relative permeability(unitless)	1

Table 4.4: Parameters of the cracked plate under investigation.

by S. K. Burke to validate the proposed approach.

A 3D finite element simulation of this model is used to determine the potential magnetic vector A from which the magnetic field density B and the eddy current J, in the studied materials, can be calculated. As it has been mentioned, the detection of the crack and its orientation angle can be achieved based on the calculated components of B and J along the y axis of scanning.

The simulation which has been performed for this model is based on the aforementioned coil topology and the aluminum plate specimen. The used alternative current for is defined as follows:

$$Js = I_0 cos(2\pi\omega ft) \tag{4.7}$$

Where the magnitude I_0 and the frequency f are chosen as $1A$ and $1kHz$ respectively. This frequency has nearly the same value as the one which was used by S. K. Burke and it is equal to the value which was used in the previous work of X. Zhiyunan et al.[135]. I was proved that it can ensure the maximum magnitude of the magnetic flux density. For the identification of the main characteristics of the crack, the scanning operation has been performed by moving the probe with a constant step of $\Delta y = 1mm$ along the y axis, where the crack is located within the range of displacement of the probe which is chosen to be from

the point of $y_i = -30mm$ to the point of $y_f = 30mm$.
The eddy current and the magnetic flux density components following the both axes have been registered for each step. On the other hand, the crack orientation angle in respective to the x axis has been varied gradually from 0° to 90° through the values of 30°, 45° and 60°. For each angle, the operation of the complete scanning has been performed for the measurements of the components of the eddy current and the magnetic flux density following both the x axis and y axis at each scanning step. The measurements can be ensured practically by giant magneto-resistive (GMR) tool, however in this simulation they are obtained via a simple technique in the used software which allows the extraction of eddy current and magnetic flux density components.

4.3.2 Flowchart of the developed code

The flowchart in Figure 4.14 presents the steps sequence of the simulation of 3d model under the software *Multi-physic Comsol 5.4.*. This flowchart explains briefly the main steps to simulate an experiment of non destructive testing by eddy current. Starting by the prepossessing steps, the introduction of geometric and physic parameters, passing to the selection of study type, the meshing and finite element processes to finish by the extraction of the results and curves.

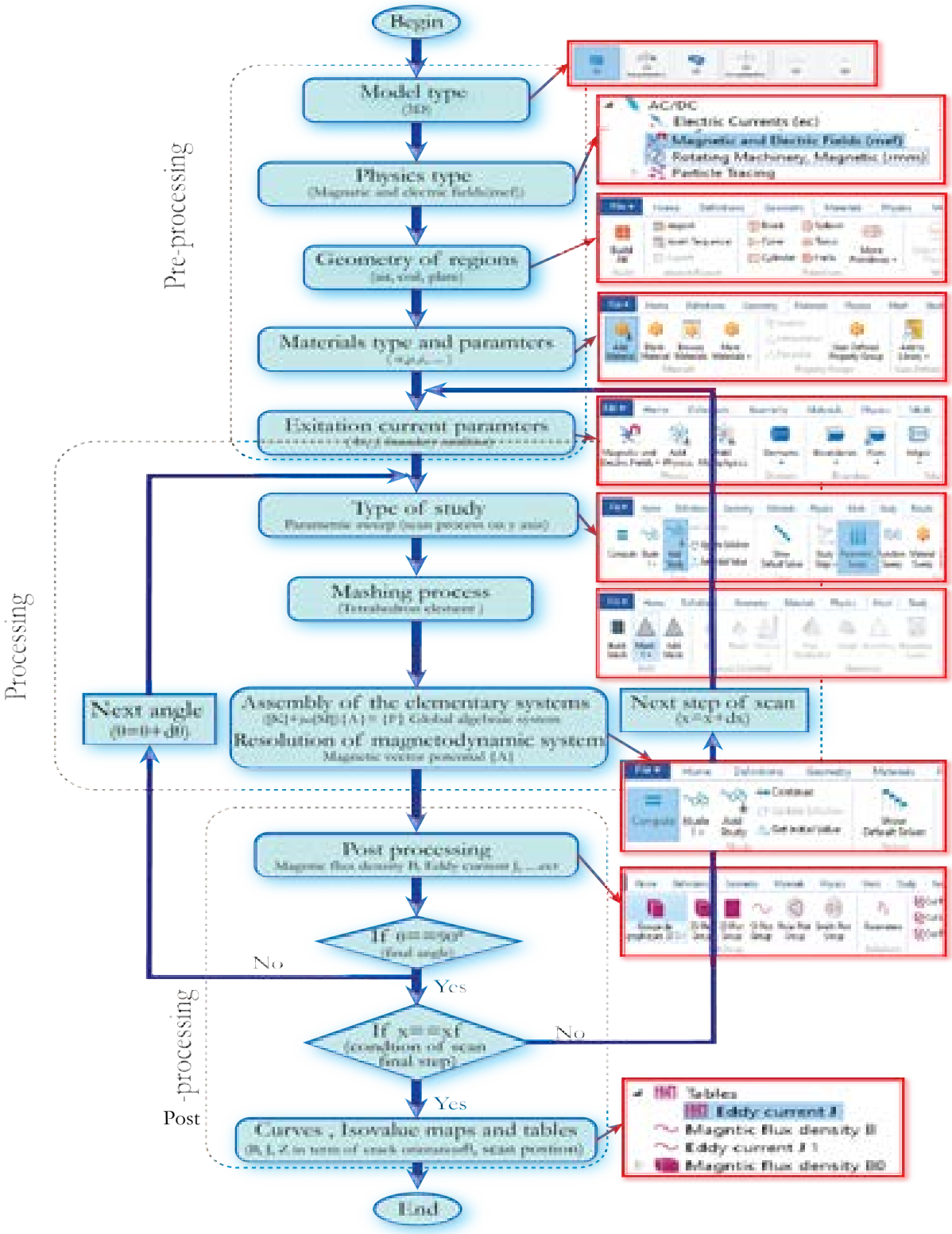

Figure 4.14: Flowchart of 3D model simulation.

4.3.3 Meshing process

The meshing adopted in this paper for the used finite elements technique is the tetrahedron meshing as shown in Figure 4.15. The meshing is redone automatically in each step of scanning, where the meshed zone under the probe is refined when there is a concentration of magnetic field. Furthermore, the meshing around the crack edge is refined due to the sharp edges and the small dimensions of the crack.

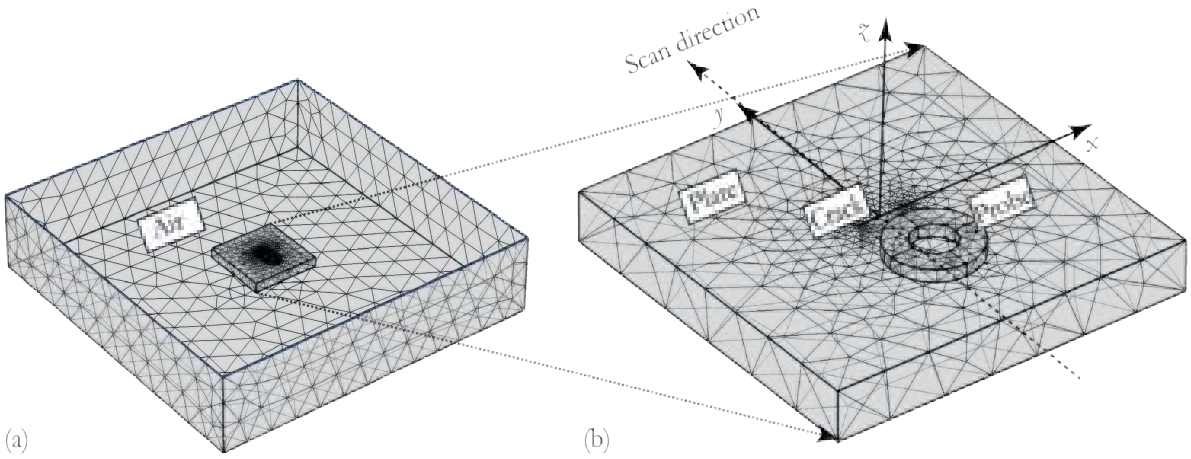

Figure 4.15: Meshing with tetrahedron elements of: a)bounding box containing the air, the probe and the plate, b)probe and plate.

4.3.4 Results and interpretations

The results of the scanning of the considered model along the chosen path for the five orientation angles have been carried out. But initially the coil located exactly above the crack to shows the behaviour of eddy current vectors as presented in Figure 4.16. The obtained two components J_x and J_y of the eddy current for the same position of the coil are depicted in Figure 4.17.

It can be seen clearly that the orientation of the most eddy current vectors at the proximity of the crack follow the crack orientation within the five cases as shown in Figures 4.16a, 4.16b, 4.16c, 4.16d and 4.16e. Indeed, when the crack orientation is parallel to the x axis, the crack orientation angle is $\theta = 0°$ as shown in Figure. 4.16a. It is obvious, in this case, that the most of the eddy current vectors are in parallel to the crack along its length, which leads

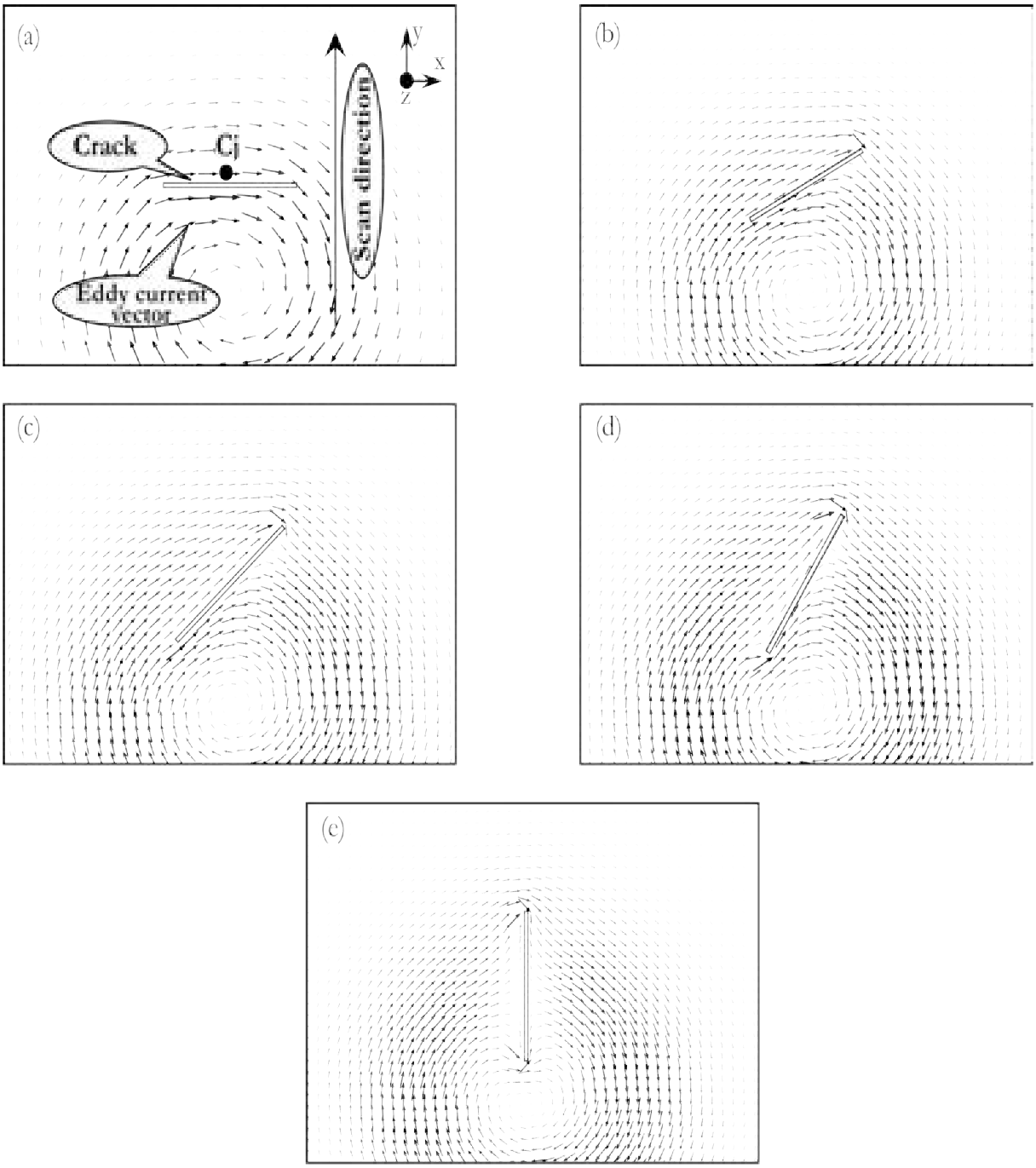

Figure 4.16: Eddy current vectors surrounding the crack with different orientations: a)0°, b)30°, c)45°, d)60°, e)90°.

to the neglected the eddy current component J_y and allows the component J_x to reach its maximum value. This physical behavior can be seen clearly in Figures 4.17a and 4.17b. On the other side, when the crack is parallel to the y axis which corresponds to crack orientation angle $\theta = 90°$, as shown in Figure 4.16e, only the eddy current vectors that are very close to

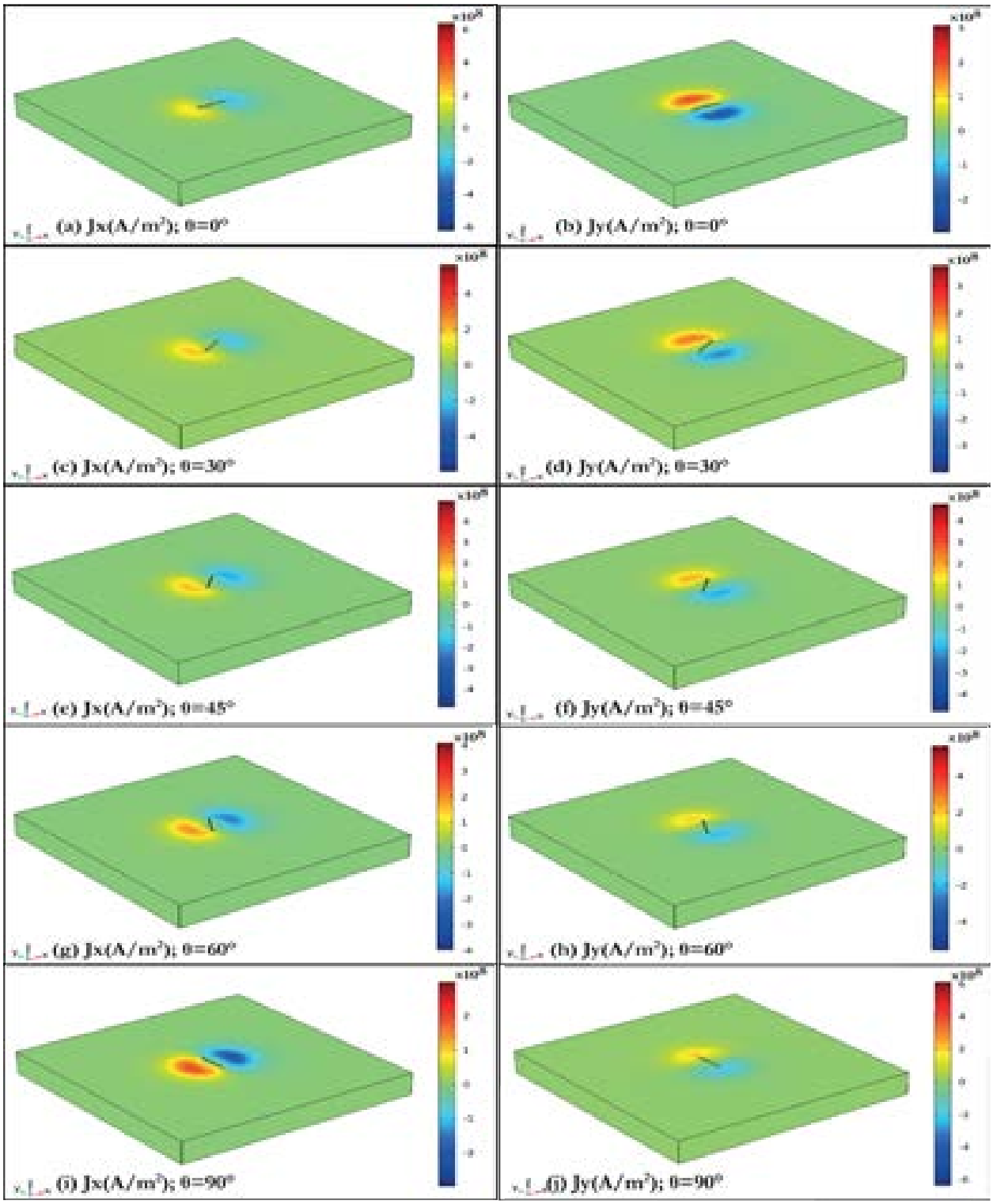

Figure 4.17: Densities of the eddy current components following x-axis and y-axis for the five crack orientation.

the crack follow the same orientation as the crack. Furthermore, as the eddy current vectors are relatively far from the crack, they lose this feature of following the crack orientation. This fact can be seen clearly in Figures 4.16. Indeed, as far as the orientation angle increases the eddy current J_x component decreases and the J_y increases, where J_x component is nearly neglected and the J_y component reaches its maximum value when the crack orientation angle is $\theta = 90°$ as shown in Figures 4.17i, and 4.17j. For the other crack orientation angles $\theta = 30°$, $\theta = 45°$ and $\theta = 60°$ this behavior is clearly depicted in Figures 4.17c to 4.17h.

It is concluded that the eddy current component J_x decreases with the increase of the crack orientation angle, at the same time the eddy current component J_y increases with the increase of the crack orientation angle. This main feature can be used in the exact estimation of the orientation of the crack within the structure of the studied model.

In the present simulation, for detecting the nature of crack orientation, a point C_j near the crack as shown in Figure4.16a is selected for the measurements of the aforementioned components and further for the measurements of the two components of the magnetic flux density. The measurements of two components of the eddy current (J_x , J_x) and the two components of the magnetic flux density (B_x , B_x) at each step of scanning along the y axis for different crack orientation have been carried out. The absolute values of the obtained measurements of (J_x , J_x) and (B_x , B_x) are depicted in Figures 4.18 and 4.19 respectively. It can be observed that the eddy current component J_x and the magnetic flux density component B_y behave similarly in the same way with a difference of scales from the point of view of the shape form of the obtained curve shown in Figures 4.18a and 4.19b. The same observation is valid for the obtained curves of the eddy current component J_y and the magnetic flux density component B_x shown in Figures 4.18b and 4.19a. The cross similarity of these curves can be explained by the fact that each couple of the cross components (J_x , B_y) and (J_y , B_x) are perpendicular to each other.

On the other side, the five obtained curves of the aforementioned components of the eddy current (J_x , J_y) are shown in Figures 4.18a and 4.18b. They are corresponding to the five selected crack orientation angles $0°, 30°, 45°, 60°, 90°$ and show an inverted behaviour according to the crack orientation. Indeed, the order of the curves belonging to J_x is inverted compared to the order of the curves belonging to J_y. It can be said that the values of J_x along the y axis decrease with the increase of the orientation angle following the obtained curves, which means the curve with the highest values is obtained at $\theta = 0°$ while the curve with the lowest values is obtained for $\theta = 90°$. As an example, it can be seen that the J_x curve (in green) which is corresponding to the crack orientation angle $\theta = 0°$ is the curve with the maximum

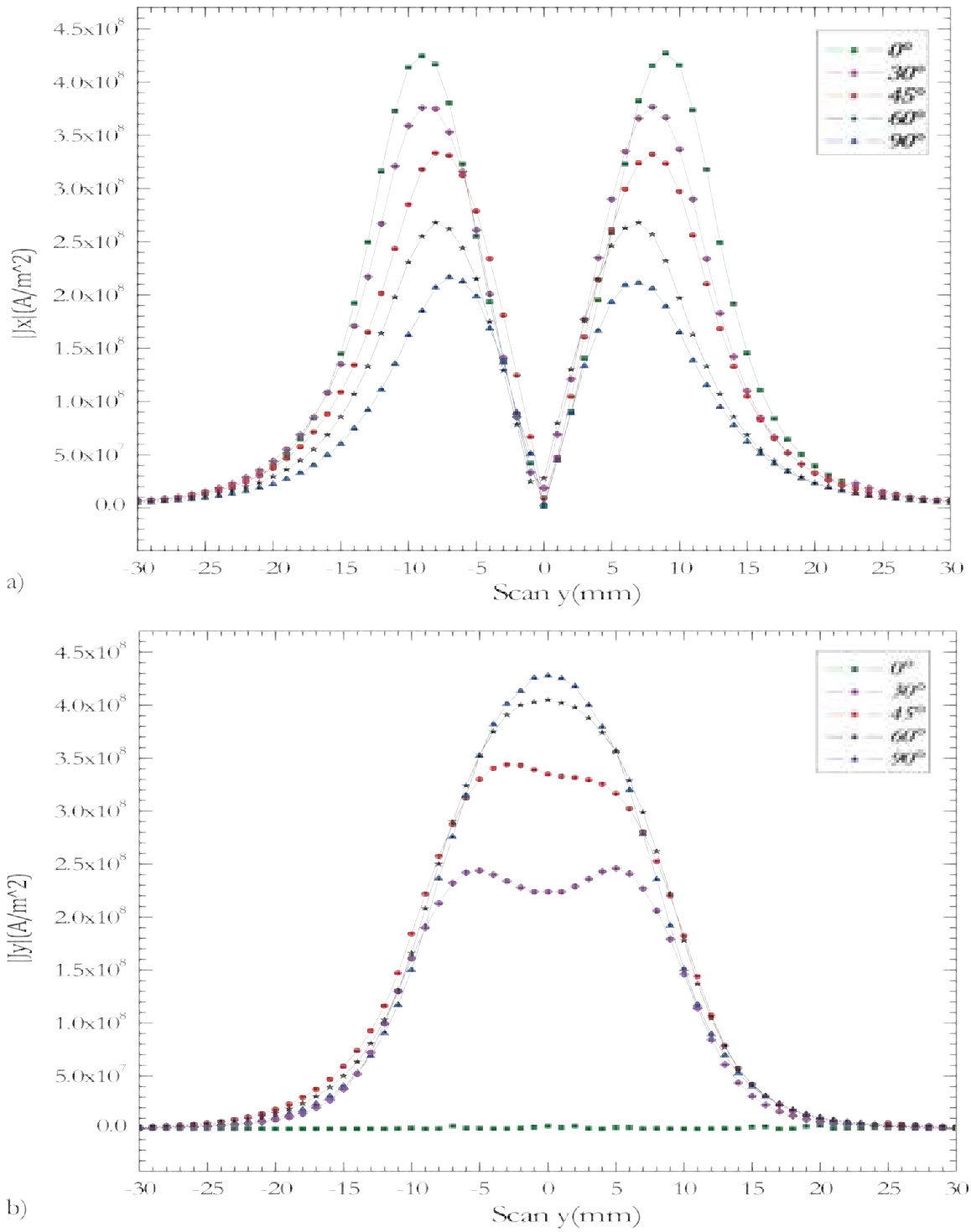

Figure 4.18: Eddy current density for different crack orientation: a)J_x component, b) J_y component.

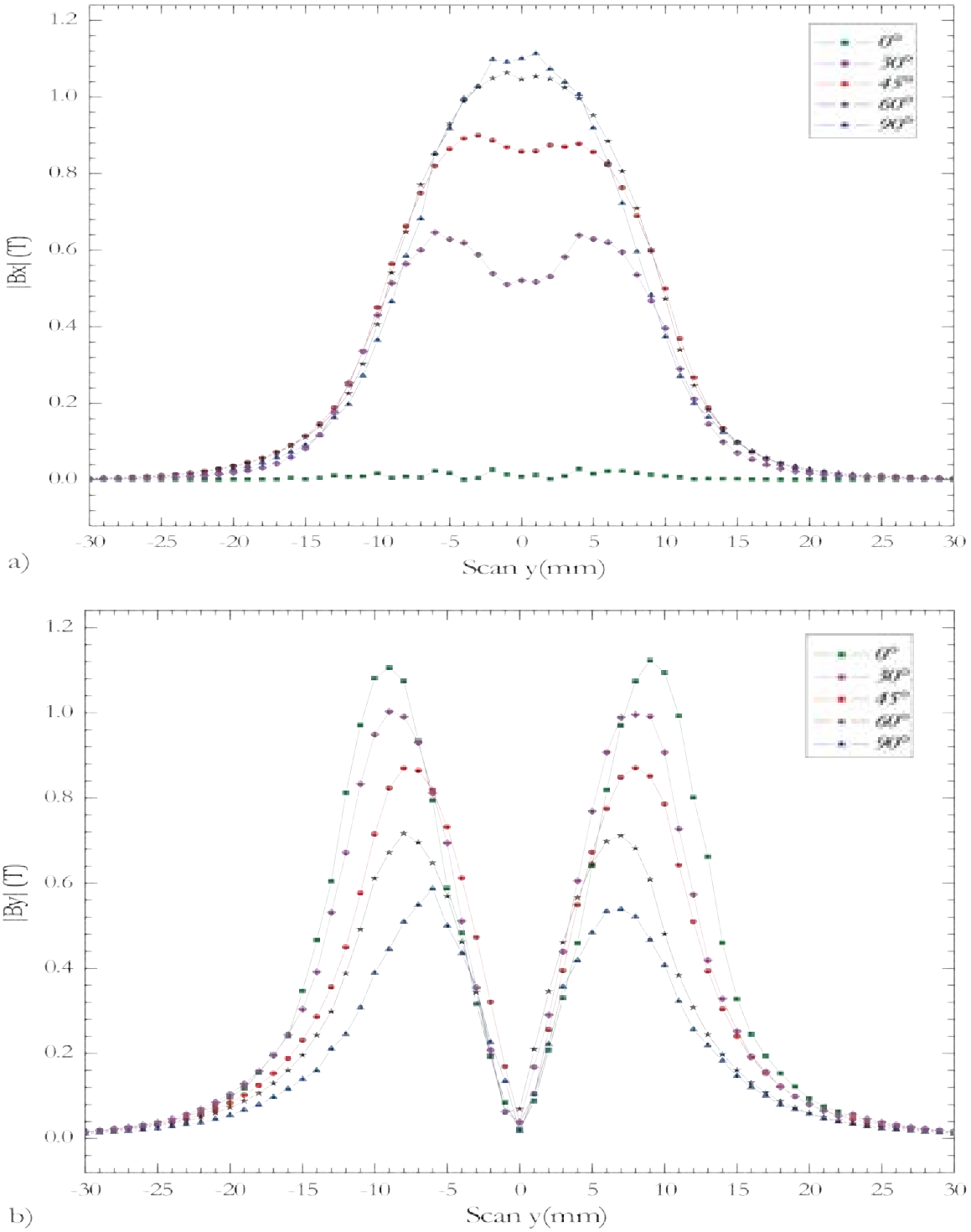

Figure 4.19: Magnetic flux density for different crack orientation: a)B_x component, b)B_y component.

values along the scanning path as shown in Figure 4.18a. Though the J_y curve (in green) which is corresponding to the crack orientation angle $\theta = 0°$, is the curve with the minimum values along the scanning path as shown in figure 4.18b).
The same observations are valid for the curves of the magnetic flux density components (B_x , B_y) shown in Figures 4.19a and 4.19b. Due to the selected path of scanning following the y axis, the eddy current J_x changes direction at the passage by $y = 0mm$; however its variation of the both sides of this point gives the same values. This explains the symmetrical nature of the J_x curves shown in Figure 4.18a. On the other hand, J_y does not change the direction along the scanning path as shown in Figure 4.18b.
On the other side, an important characteristics can be observed between the J_x and B_x in one hand and between J_y and B_y in the other hand. It present the same observation registered between the curves of(J_x and J_y) to the similarity of curves between (J_x and B_y) and (J_y and B_x) as explained above. As an example, it can be seen that for the crack orientation angle $0°$, J_x (green curve) takes the maximum values as shown in Figure 4.18a while B_x(green curve) takes the minimum values as shown in Figure 4.19a, this can be explained further by the fact that the resulting magnetic field from the coil is perpendicular to the lines of the induced eddy current in the plan of the studied model. This can also be observed in the same way between J_y(green curve) which takes the minimum values and it is nearly equal to zero as shown in Figure 4.18b, and B_y(green curve) that takes the maximum values as shown in Figure 4.19b.
It is worthy to clarify that at positions $y = -30mm, y = 0$ and $y = +30mm$, J_x is null for all the orientation angles and J_y is null for all the orientation angles at only $y = -30mm$ and $y = +30mm$, This is because the chosen measurement pointC_j is located near the crack as illustrated in Figure 4.16a.
Based on the obtained results, the crack orientation angle in terms of the peak values of (J_x and J_y) and (B_x and B_y) corresponding to the five considered crack orientation angles are plotted in Figures 4.20 and 4.21 respectively. In this manuscript, a simple interpolation of the four obtained curves is proposed to obtain their corresponding fitting functions. It is found that J_x and B_y curves can be fitted using a cubic function due to their similarity as shown in Figures 4.20a and 4.21b respectively. Similarly, J_y and B_x curves can be fitted by an exponential function due to their similarity as shown in Figures 4.20b and 4.21a respectively.

The obtained fitting functions are proposed to be as special empiric functions for the studied model of the cracked plate. They can be used to calculate the crack orientation angle

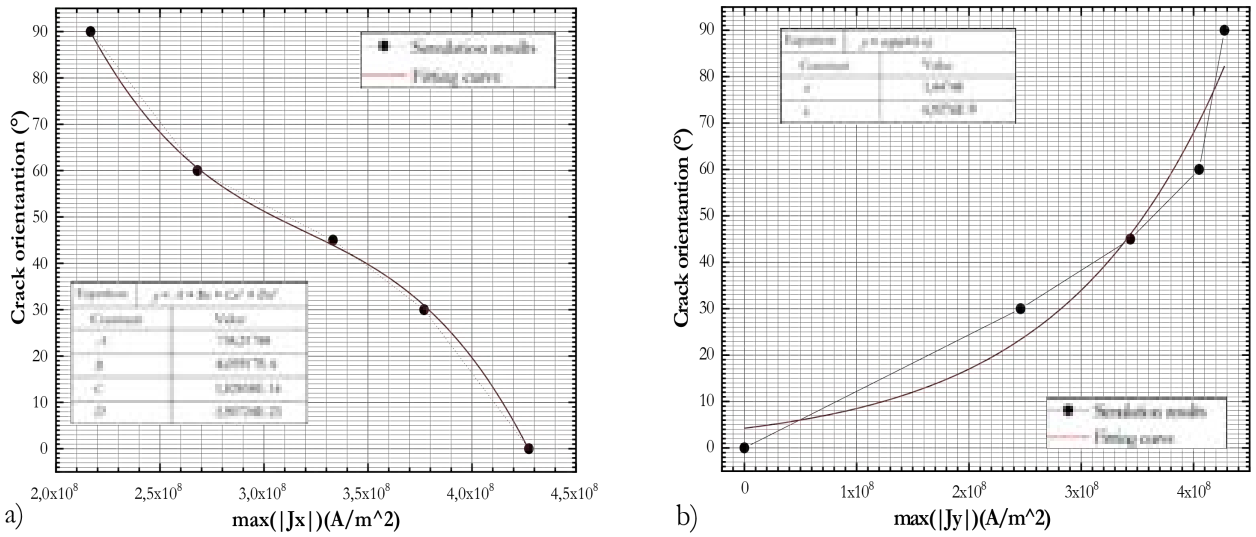

Figure 4.20: Maximum values of the eddy current density and the proposed empirical model following different crack orientation angles: a)$J_x$component, b)$J_y$component.

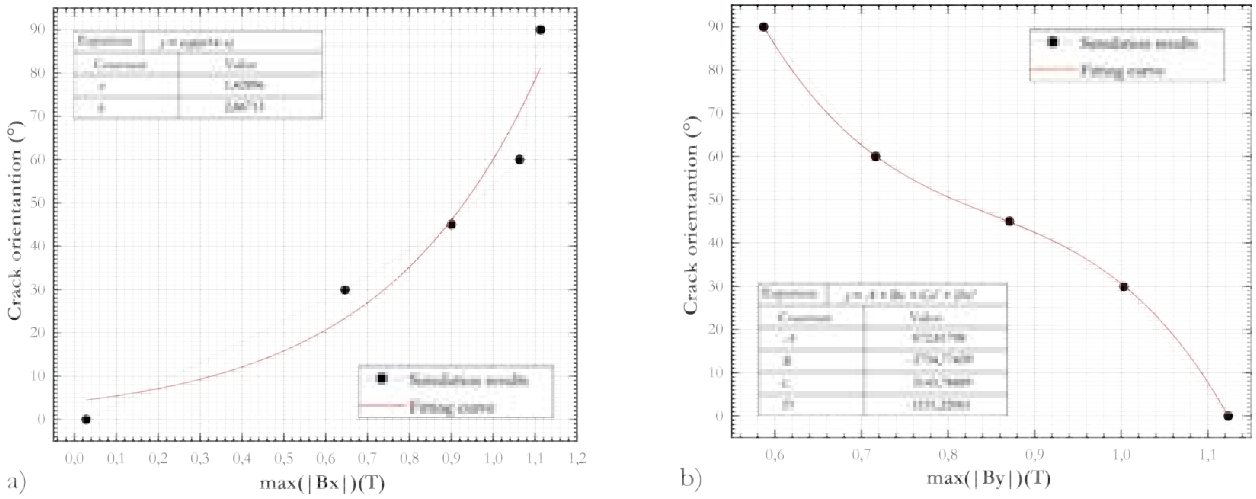

Figure 4.21: Maximum values of the magnetic flux density and the proposed empirical model: a)B_x component, b)B_y component.

from the measured eddy current or magnetic flux density. Hereinafter, this angle is used to calculate an important parameters of the cracked plate such as the Stress Intensity Factor (SIF) expressed as:

$$K_I = \sigma\sqrt{\pi a}cos^2(f(J_x)) \tag{4.8}$$

$$K_{II} = \sigma\sqrt{\pi a}cos(f(J_x))sin(f(J_x)) \tag{4.9}$$

where the orientation angle θ of the crack can be approximated the polynomial expression

function of J_x taken from 4.20a:

$$f(J_x) = \theta = A + BJ_x + CJ_x^2 + DJ_x^3 \tag{4.10}$$

with the fitting constants:
$A = 738.21788$; $B = -6.05917 \quad 10^{-6}$; $C = 1.82858 \quad 10^{-14}$; $D = -1.90724 \quad 10^{-23}$.
For example, a 2D model similar to the studied cracked plate is simulated with a crack length $a = 12mm$, an orientation angle $\theta = 20°$ and a tensile charge $\sigma = 100MPa$. The Young modulus and the Poisson' ratio of the considered model, respectively, are $E = 13000MPa$ and $\nu = 0.33$.
The maximal measured value of the eddy current obtained from the scanning process is: $J_x = 823.97573.10A/m^2$. Hence, the estimated crack orientation angle can be calculated based on the empiric function of (4.10) as follows:

$$\theta = f(J_x) = A + BJ_x + CJ_x^2 + DJ_x^3 = 21.04° = 0.3672rad \tag{4.11}$$

This value is very close to the real crack orientation angle which is 20°. Hence, the SIFs for the i^{th} mode can be estimated as follows:

$$K_I = 100\sqrt{\pi 12}cos^2(0.3672) = 534.86N/mm^{3/2} \tag{4.12}$$

$$K_{II} = 100\sqrt{\pi 12}cos(0.3672)sin(0.3672) = 205.73N/mm^{3/2} \tag{4.13}$$

Based on the obtained SIF values and the following equation:

$$J_i = K_i^2\frac{1-\upsilon^2}{E} \tag{4.14}$$

The J-integral components can be obtained as follows:

$$J_I = K_I^2\frac{1-\upsilon^2}{E} = 534.86^2\frac{1-0.33^2}{13000} = 19.609Joule \tag{4.15}$$

$$J_{II} = K_I I^2\frac{1-\upsilon^2}{E} = 205.73^2\frac{1-0.33^2}{13000} = 2.901Joule \tag{4.16}$$

From the obtained results, we conclude that the curves illustrated in Figures 4.20 and 4.21 can be considered as abacus to estimate the crack orientation corresponding to the maximum value of measured signals during the eddy current testing. Furthermore, it can help us to determine some important parameters such as the SIF, the J-integral and even to predict the dynamic propagation angle. In case where the fitting operation is difficult or even impossible, the use of one of the heuristic algorithms is an alternative.
In this context, we present in the next section one of these solutions which is the Harris hawks optimization approach.

4.4 Inverse problem using Harris hawks optimization

After the direct detection of crack orientation angle in axisymmetric model using the finite element method, we propose in this section an alternative method, which is the resolution of inverse problem using optimization method called Harris Hawks Optimization(HHO). This inverse problem consists in searching the best crack angle corresponding to the measured maximal value of the sensor impedance.

4.4.1 Historical review on the optimization algorithms

Every inverse problem requires decision making, either in engineering or economics, based on optimization algorithms. Making a decision means made a choice between several solutions. These algorithms drive our decision to the best one. An objective function or performance index describes the alternatives' effectiveness. The best alternative in optimization theory is given in terms of the objective function.
In recent years, the field of optimization has gotten a lot of interest, owing to the significant development of computer and computing techniques, such as high-speed and parallel processors, artificial intelligence techniques. Among the most popular optimization tools in engineering are the meta-heuristic optimization algorithms which have the following features:

- Based on simple concepts and simple to implement.
- Do not need gradient information.
- Can avoid local optima.
- Can be applied to a variety of situations from many areas.

Meta-heuristic algorithms inspired from nature solves optimization problems by imitating biological or physical procedures. They can be divided into three categorizes: evolution-based, physics-based, and swarm-based methods [137]. The laws of natural evolution motivate the development of an optimization algorithm based on evolution approaches. Among these, we can mention the genetic algorithms [138], the evolution strategy [139] and the biogeography based optimizer [140].
The physics-based algorithms mimic the universe's physical laws. The most known algorithms in this category are: simulated annealing [141], central force optimization [142], gravitational local search [143] and galaxy based search algorithm [144].
The third category is nature inspired algorithms, that imitate animal behavioral patterns.

It includes methods like: ant colony optimization [145], whale optimization algorithm [137], Harris hawks optimization [146], gray wolf optimization [146] and particle swarm optimization (PSO). The new commonly used algorithm in this category is the Harris hawks optimization(HHO) technique, created by Ali A. H. et al.[146] and adopted, in our case, to solve the inverse problem.

4.4.2 Harris hawks optimization

The HHO method is a meta-heuristic that allows to find the optimum of a function in a reasonable processing time. The HHO simulates the social behavior of Harris hawks' swarms. The main strategy of HHO algorithm based on the mathematical imitation of a chasing method of the Herris hawks named chasing which is pouncing cooperatively at the prey from many directions in an attempt to surprise it. this algorithm was checked its effectiveness on several kind of engineering problems comparing with the other metaheuristic algorithms[146]. This algorithm has two steps, exploratory and exploitative steps inspired by the exploring of prey, surprise pounce, and different attacking strategies of Harris hawks as illustrated in the Figure 4.22 . the Harris' hawks are considered as the candidate solutions while the best candidate solution in each step is considered as the intended prey.

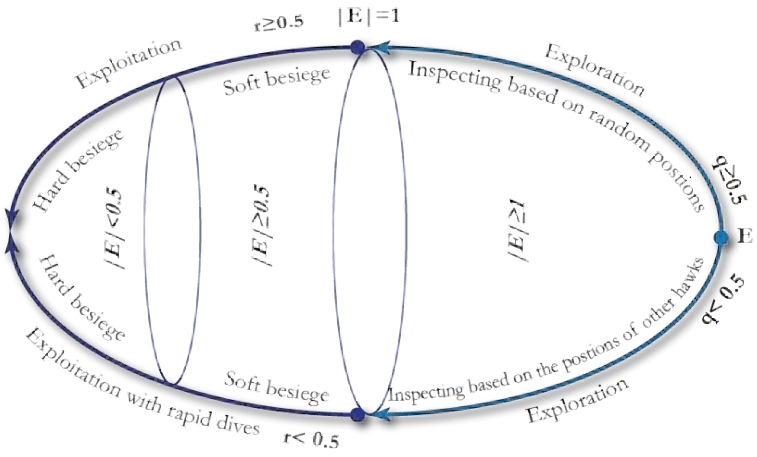

Figure 4.22: Exploratory and exploitative steps of HHO.

4.4.2.1 Exploration step

In this step, the Harris' hawks watch randomly some areas and inspect the existence of prey using two methods based on the equations.

$$X(t+1) = \begin{cases} Xrand(t) - r_1|X_{rand}(t) - 2r_2X(t)| & q \geq 0.5 \\ (X_{prey}(t) - X_m(t)) - r_3(LB + r_4(UB - LB)) & q < 0.5 \end{cases} \tag{4.17}$$

when

$q < 0.5$: the hawks inspecting based on positions close enough to the pray. $q \geq 0$: the hawks perch on random positions inside the main search area.

where $X(t+1)$is the position vector of hawks in the next iteration t, $Xprey(t)$ is the position of pry(rabbit), $X(t)$ is the current position vector of hawks, $r1, r2, r3, r4$, and q are random numbers inside (0,1), which are updated in each iteration, LB and UB show the upper and lower bounds of the search area, $Xrand(t)$ is a randomly selected hawk from the current swarm, and Xm is the average position of the current swarm of hawks.

4.4.2.2 Exploitation step

In this step, the Harris' hawks attack the intended prey detected in the previous phase using the surprise pounce technique. According to the escaping behaviors of the prey, the Harris' hawks use four possible strategies of attacking.

1. **Soft besiege:**
   When $r \geq 0.5$ and $|E| \geq 0.5$ the rabbit still has enough energy E to escape and the hawks encircle it softly, This behavior is modeled by the following rules:

$$X(t+1) = \Delta X(t) + E|MX_{prey}(t) - X(t)| \tag{4.18}$$

$$\Delta X(t) = X_{prey}(t) - X(t) \tag{4.19}$$

   where $\Delta X(t)$ is the difference between the position vector of the prey and the current location in iteration t, r_5 is a random number inside $(1, 2)$, and $M = 2(1-r_5)$ represents the random leap strength of the prey.

2. **Hard besiege:**
   When $r \geq 0.5$ and $E| < 0.5$ the prey has low escaping energy, and the Harris' hawks hardly encircle the intended prey to finally perform the surprise pounce. the current positions are updated using Eq. beginequation

$$X(t+1) = x_{prey}(t) - E|\Delta X(t)| \tag{4.20}$$

   the next two strategies mimic mathematically the escaping patterns of the prey and rapid dives of hawks around the escaping prey

3. **Soft besiege with progressive rapid dives:**
   when $|E| \geq 0.5$ and $r < 0.5$ the updating the positions of hawks in the soft besiege given by

$$X(t+1) = \begin{cases} Y & F(y) < F(X(t)) \\ Z & F(Z) < F(X(t)) \end{cases} \tag{4.21}$$

   with $Y = X_{prey}(t) - E|MX_{prey}(t) - X(t)|$ and $Z = Y + SxLF(D)$ where D is the dimension of problem and S is a random vector by size $1 \times$ D and LF is the levy flight function which mimic the real zigzag motions of preys[146].

4. **Hard besiege with progressive rapid dives:** When $|E| < 0.5$ and$r < 0.5$ the escape energy of prey is weak and a hard besiege is done before the surprise pounce to catch the prey, the updating positions of howks $X(t+1)$ estimate by the same previous equation (4.21) with new form of $Y = X_{prey}(t) - E|MX_{prey}(t) - X_m(t)|$.

4.4.3 Algorithm of Harris hawks optimization

For more details, the Figure 4.23 presents the HHO procedure. Starting by the input parameters such as the iterations and hawks number and initiation of the first Hawks swarm, passing to the processing which contains the calculation of fitness and personal best solution of each hawks thought two steps (exploration and exploitation), and for each iteration and each step, there is an updating of the positions of hawks, until the stopping condition is achieved and finishing by estimation of the best global solution and its fitness function which is in our problem the best crack orientation angle for given value of the impedance sensor and its relative error.

4.4.4 Description of the inverse problem

As example we take the previous axisymmetric problem with same input parameters (frequency, left off, conductivity). During the scan process, the absolute sensor recorded the following maximal value of normalized impedance $dZ_{exp} = 0.6364\Omega$. According to the direct problem, treated previously, this value corresponds to the angle $\theta_{exact} = 45°$. The question here is to find the best corresponding crack orientation angle θ_{gb} using the Harris hawks optimization with the following set of parameters:

- $N = 10$ the number of hawks.
- $T = 10$ the number of iterations.

1. **Input** the hawks number N and the iterations number.
2. **Initialize** the random postions of hawks Xi(i = 1, 2, . . . , N)
3. **If** (stopping condition is not met) do for t iteration
   3.1. Calculate the fitness values of hawks.
   3.2. Set Xrabbit as the location of rabbit (best location)
   3.3. for (each hawk (Xi)) do
   -Update the initial energy E_0 and jump strength M
   -Update the E using this equation $E=2E_0(1-t/T)$
   - **If** ($|E| \geq 1$) then (Exploratory step)
     -Update the location vector using equation 4.17
   - **If** ($|E| < 1$) then (Exploitative step)
     - **If** ($r \geq 0.5$ and $|E| \geq 0.5$) then (Soft besiege)
       -Update the location vector using equation 4.18
     - **Else if** ($r \geq 0.5$ and $|E| < 0.5$) then (Hard besiege)
       -Update the location vector using equation 4.20
     - **Else if** ($r < 0.5$ and $|E| \geq 0.5$) then (Soft besiege with progressive rapid dives)
       -Update the location vector using equation 4.21
     - **Else if** ($r < 0.5$ and $|E| < 0.5$) then (Hard besiegewith progressive rapid dives)
       -Update the location vector using equation 4.20 with new Y
     - **End if**
   - **End if**
4. **Output** the location of prey and its fitness value Xprey

Figure 4.23: Harris hawks optimization algorithm.

- $LB = 0, UB = pi/2$ the lower and upper band of the search area for crack orientation angles respectively.

In this example, the fitness function is given by:

$$fit = \left| \frac{dZ_{est} - dZ_{exp}}{dZ_{exp}} \right| \tag{4.22}$$

where dZ_{est} is the estimated normalized impedance using the HHO and $dZ_{exp} = 0.6364\Omega$ is the experimental value of the normalized impedance.

4.4.5 Results and interpretation

The Figure 4.24 illustrates the obtained global fitness using the aforementioned parameters. The fitness decreases exponentially with the number of iterations which proves that the HHO

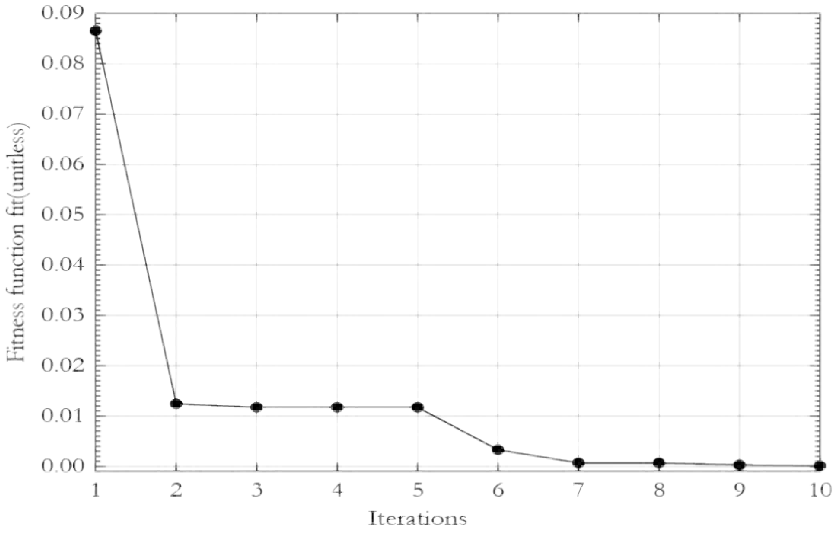

Figure 4.24: Global fitness for each iteration.

converges rapidly due to the simplicity of the treated inverse problem. Indeed, it has one dimension which mean one target parameter (crack orientation) in the search area.
The Figure 4.25 presents the global best crack orientation θ_{gb}:

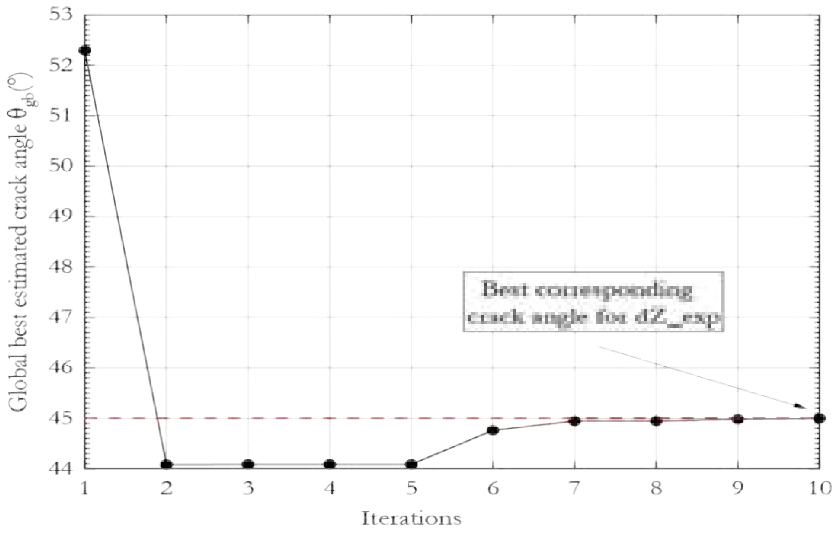

Figure 4.25: Global best solution for each iteration.

We remark that the global best solution decreases exponentially and converges rabidly to the exact value of the crack angle ($\theta_{exact} = 45°$), which is corresponding to the value of dZ_{exp} (measured experimentally) and proves,thus, the effectiveness of this method to treat such type of problems.
From iteration 2 to iteration 9, the value of global best solution was goes below the exact

crack angle $\theta_{exact} = 45°$. This due to the fact that the investigated crack angle is in the middle of the search area$[0, \pi/2]$ and the random nature of searching causing this feature.
The computing time for 10 hawks and 10 iteration is 850s (14 minutes). It can be considered relatively large, but it is acceptable if we look at the size of the treated problem and the accuracy of the obtained results.
The previous results requires more analysis on the personal fitness and best solution of each hawk and also studying the effect of the hawks number, iterations number on the results accuracy and the computing time. Initially, Tables 4.5 and 4.6 present, respectively, the personal fitness and the best solution for each hawk i in each iteration t. From Tables 4.5 and

	Iterations (t)									
i	1	2	3	4	5	6	7	8	9	10
1	0.26301	0.31015	0.31259	0.17999	0.31015	0.27453	0.06392	0.02943	0.31031	0.00340
2	0.29434	0.15247	0.01918	0.31015	0.25921	0.03265	0.01675	0.01675	0.00269	0.00051
3	0.27823	0.02185	0.30471	0.31015	0.11884	0.05964	0.05964	0.05964	0.04497	0.00842
4	0.29727	0.31015	0.31259	0.04187	0.04187	0.19098	0.31259	0.08597	0.03416	0.01362
5	0.14011	0.14011	0.17429	0.31015	0.01735	0.00685	0.00685	0.00069	0.00069	0.00069
6	0.28739	0.31015	0.31259	0.04091	0.14207	0.14207	0.14207	0.03933	0.01471	0.00816
7	0.21672	0.31015	0.22428	0.01012	0.00182	0.00182	0.00182	0.00182	0.00073	0.00038
8	0.04711	0.03808	0.01668	0.31015	0.10262	0.06831	0.06348	0.00962	0.00258	0.00258
9	0.30301	0.31015	0.20615	0.31015	0.31015	0.02387	0.02387	0.31015	0.01261	0.00202
10	0.30655	0.29543	0.18392	0.31015	0.30148	0.26640	0.01035	0.01035	0.01035	0.00254

Table 4.5: Personal fitness of N hawks in each iteration t.

	Iterations (t)									
i	1	2	3	4	5	6	7	8	9	10
1	-41.887	116.837	29.130	-1.154	12.100	40.363	42.497	1.065	45.257	44.935
2	31.704	46.757	-9.946	19.772	48.087	46.533	46.533	45.192	44.959	44.959
3	47.087	5.429	-11.795	34.747	50.166	50.166	50.166	48.879	44.424	44.877
4	-20.223	108.394	41.398	41.398	27.783	125.273	38.153	48.227	46.216	45.390
5	56.912	61.002	-19.961	46.589	45.572	45.572	44.942	44.942	44.942	44.942
6	-10.866	91.536	48.828	32.638	32.638	32.638	41.686	46.310	44.448	44.448
7	-66.221	67.945	44.231	45.103	45.103	45.103	45.103	44.939	44.944	**44.994**
8	48.564	46.823	-19.931	53.747	39.817	40.404	44.277	44.823	44.823	44.933
9	-127.962	64.968	-64.481	0.000	43.105	43.105	-0.833	46.124	45.130	44.970
10	81.799	62.027	-64.050	7.402	13.653	45.802	45.802	45.802	44.828	44.979

Table 4.6: Personal best solution (crack angle) of N hawks in each iteration t.

4.6, we observe that the personal fitness and best solution of all hawks decrease passing from iteration 1 to iteration 10. Nevertheless, there are some fluctuations due to the randomness of the parametersr_i $i = 1_5$ defined previously in the HHO algorithm.

The hawk 7 has the minimal personal fitness means it reaches the best solution at the iteration 10 ($\theta_{pb} = 44.994°$) as shown in Table 4.6.

For more clarification of the previous observation, the Figures 4.26 and 4.27. illustrate, respectively, the personal fitness and the personal best solution of the hawk during the 10 iterations.

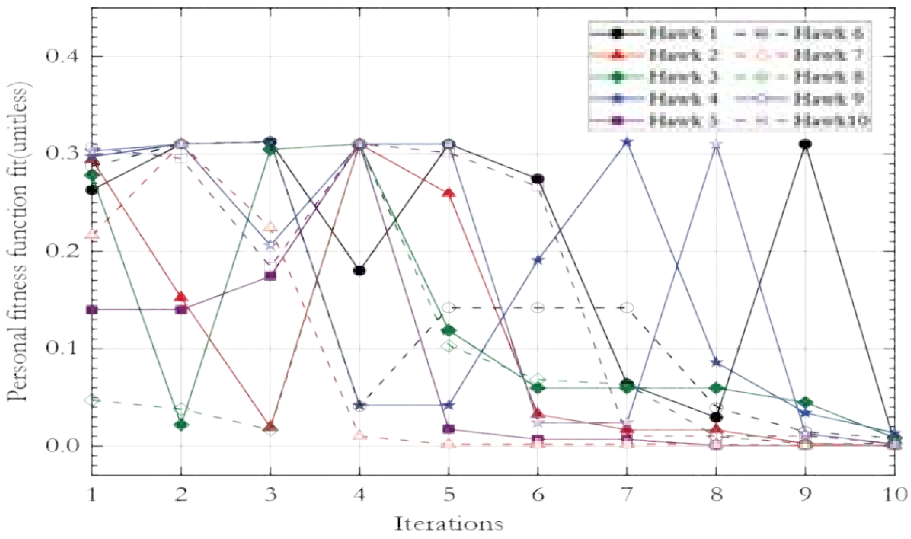

Figure 4.26: Personal fitness of hawks for each iteration.

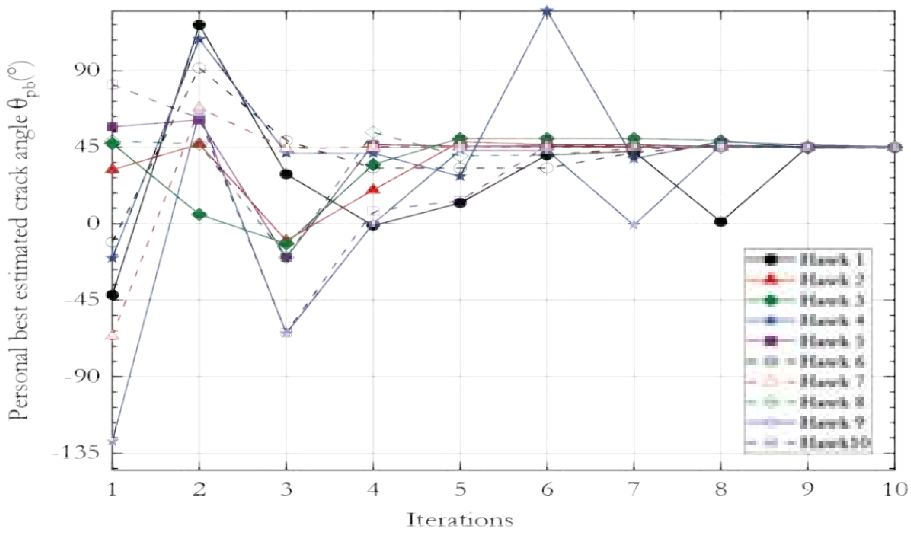

Figure 4.27: Personal best solution of hawks for each iteration.

From the Figure 4.26, we note that the hawk 9 has the most stable convergence. It is obvious from Figure 4.27 that all personal best solution (crack angle) converge to the exact value $\theta_{exact} = 45°$ and the hawk 7 has the fastest convergence rate.

The negative angles appears almost for all hawks and even pass the boundary of search area(LB,UB) as shown in Figure 4.27, are due to the chosen random coefficient r_i of the exploration step.

Iterations number effect:

Passing to the parametric study on the iterations number. The Figure 4.28 presents fitness for range of 10 to 100 iterations with step of 10 iteration and fixed number of hawks equal 10. Firstly, the fitness always decrease whatever the final number of the iterations but with dif-

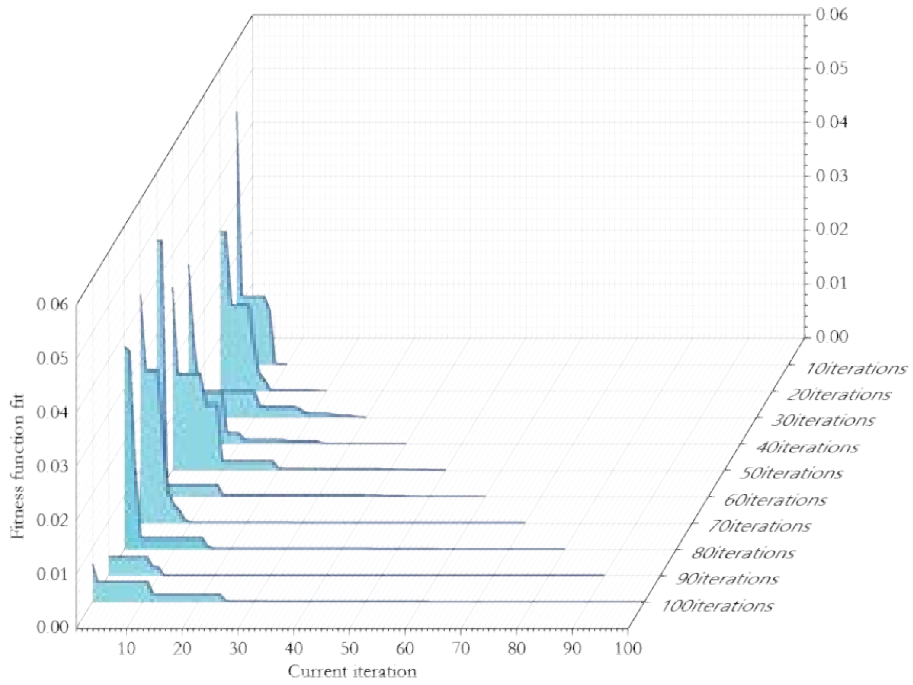

Figure 4.28: Effect of the iterations number on the fitness function.

ferent ways. That can be explained by the random nature of the exploration and exploitation steps. Secondly, most of the element converge to the minimal value of fitness at 30 iterations. As a consequence, for this kind of problems, 30 iterations is sufficient to provide adequate accuracy of results.

The Figure 4.29 illustrate the effect of the iterations number on the three important factors: the best solution (crack orientation) given in Figure 4.29a, the relative error on estimating the crack angle as shown in Figure4.29b, and the consumed computing time illustrated in Figure 4.29c. The interpretations of these results can be summarized as follows:

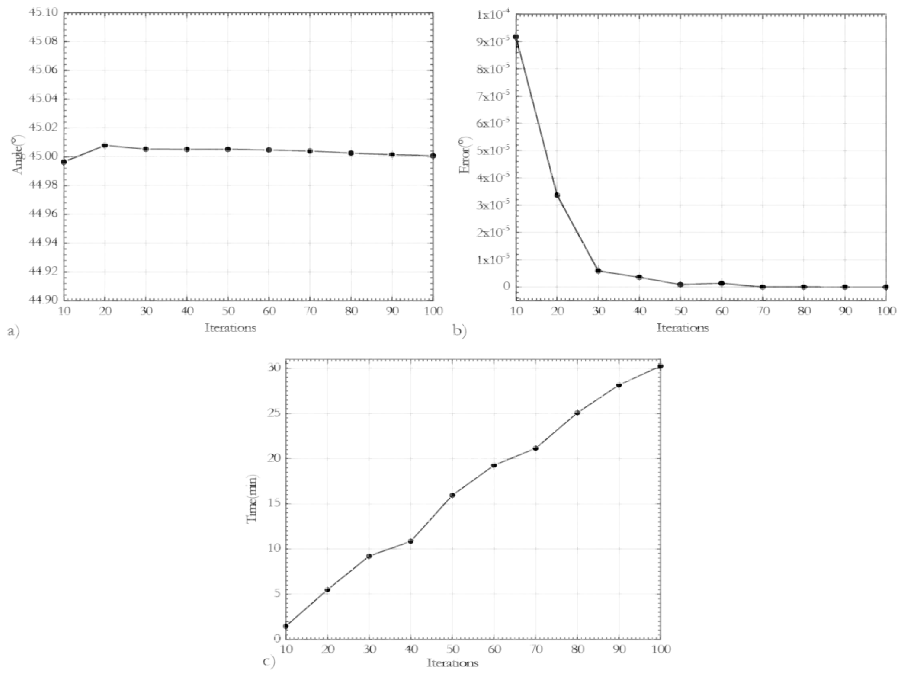

Figure 4.29: Effect of iteration number on the best solution: a)best crack angle, b) relative error, c)computing time.

From Figure 4.29, the HHO convergences with stable way to the best angle and, practically, attain it in 70 iteration . Additionally, the computing time increases almost linearly with the iterations number, which is a logical fact, because the iterations are not related to each other and the same operations are done for each iteration. The relative error decrease exponentially which indicates the effeteness of the algorithm.

Hawks number effect:

The Figure 4.30 illustrates the effect of the hawks number on the fitness function with fixed number of iteration equal to 10. The range of the hawks changes is $[10, 100]$ with a step of 10. The observations that we can extract from this figure that the number of the hawks affects linearly the convergence unlike the iterations number that affects it gradually.

The fitness converges, differently, to the minimal value for each range of hawks. The fast convergence of fitness is with the range of 100 hawks which reach the minimal value at the second iteration. The convergence speed changes randomly with the hawks number due to the random nature of hawk movement.

The Figure 4.31 illustrates the effect of the hawks number on the best solution(crack orientation), on the relative error and on the computing time. The observations that can be collected, from the Figure 4.31, are:

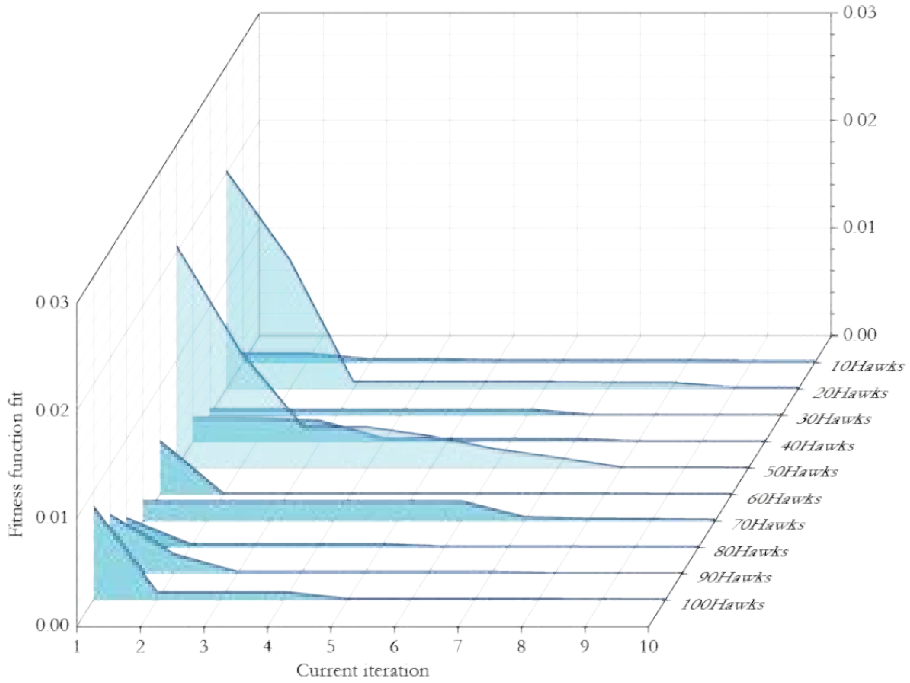

Figure 4.30: Effect of hawks number on the fitness function.

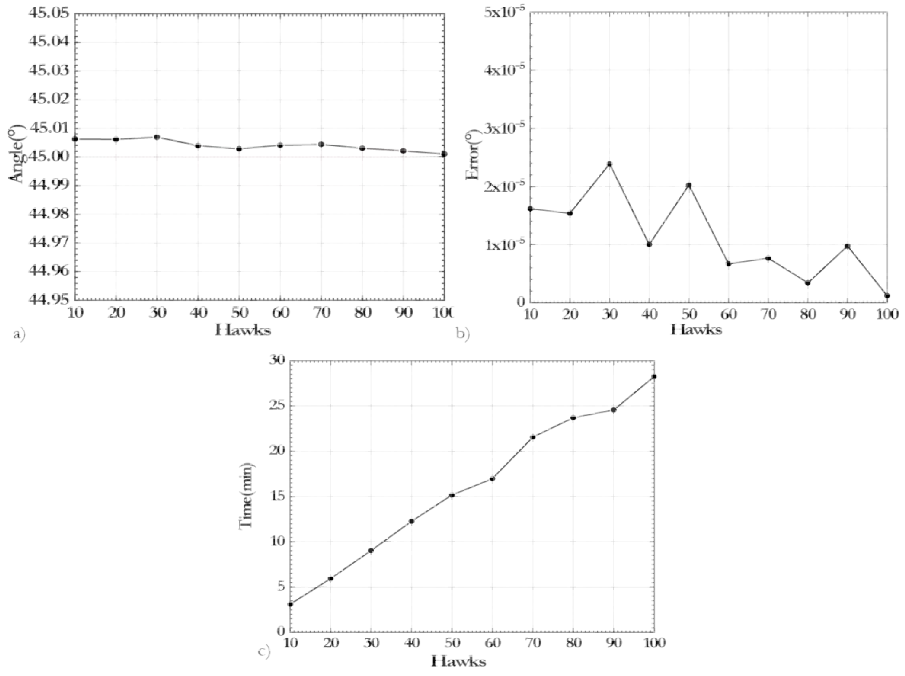

Figure 4.31: Effect of hawks number on the best solution: a)best crack angle, b)relative error, c)computing time.

- The best solution decrease to the exact value and converges to it at 100 hawks.

- the decreasing fluctuation of relative error indicates that the updated positions of hawks become very small. Hence, this marks the end of the optimisation operation.
- The consumed computing time increases almost linearly with the iteration number because the hawks interacts independently with each other.

4.5 Conclusion

As this chapter contains mostly the fruit of this thesis, the important solutions and conclusions of the treated problem are summarized as follows:
Firstly, the study of 2D axisymmertic model of inspected rod by absolute sensor led to the fallowing conclusions:

- The real and imaginary parts of the magnetic potential vector are effected directly by the change of the crack orientation and this fact has been proved theoretically and numerically.
- Under the use of adequate values of frequency and the left off, the impedance can be used as a good indicator of the existence and position of internal cracks,and also its orientation.
- The reactance of the absolute sensor is more affected, than the resistance, by the crack orientation.

Secondly, through the simulation of the 3D model of multi-turn coil investigating a cracked metal plate, the major results are:

- The crack orientation angle has a big influence on the output electromagnetic signals such as magnetic flux density and eddy current components. This fact is the first main result of our work.
- The second main result, of our work, is the quantification of this influence by simple empiric equation that relates directly the the variation of eddy current to the value the crack orientation.
- The third main result is in the empiric equation utility for the calculation of fracture parameters such as the stress intensity factor SIF and the J-integral.

Lastly, to deal with the difficulties that face the engineer to use the proposed direct approaches, we proposed, as fourth main contribution, an alternative method based on HHO to treat the inverse problem of the axisymmetric model. The proposed approach allows us to find and even to predict the orientation of hidden cracks using measured values of the sensor impedance.

General conclusion and perspectives

The objective of this thesis was to provide some contributions in the field of non-destructive control (NDT) by eddy current (EC) and to use it in the domain of fracture mechanics. The contributions was around the treatment of two type of problems.
The direct problem aims to provide qualitative and quantitative information about crack orientation. Our goal was, on one hand, to show the importance of the crack orientation in the fracture parameters calculation. On the other hand, to prove, the presence of the effect crack orientation on the output signals of the NDT-EC and to quantify, that effect on the eddy current, the magnetic flux density and the impedance. The inverse problem, which aims to characterize the crack orientation, gives an estimate of their value in order to deduce its gravity and to give support to specialists to facilitate the interpretation of the measured signals and to make the right decision.
The study of the direct problem was carried out by exploiting the finite element method by resolving the magnetodynamic equation in 2D axisymmetric geometry and in 3D model of a metal cracked plate. The scanning of the tested metal plate is done using absolute probe in two cases of 2D and 3D of the problem. The impedance, eddy current and magnetic flux signals, according to the scan position and for each studied crack angle, are obtained by re-meshing the whole model and re-run the finite element process.
The conclusions that can be drawn from the 3D model are:

- After many tries in the previous studies and also in this present work, to find a specific convenient topology of sensors to detect the crack orientation, simply we find that an absolute sensor can quantify the crack orientation using the output signals of eddy current or magnetic flux density. The main idea was the decomposition of each signal into two components along x and y axes. The study showed, after, that the crack orientation angle affects the values of these four components and their values depend on the crack orientation angle and the position of the crack.

- An empirical model is developed using an interpolation technique to express the crack

orientation as function of the NDT-EC output signals.

- The estimated crack angle orientation is used for the calculation of the stress intensity factor SIF and the J-integral components, which gives precise details on the severity and the degradation level of the structure caused by the crack. This allows avoiding major damage and risks that may happen to the whole structure and estimating the remaining of its lifetime.

Additional conclusions are obtained from the study of the axisymmetric model and listed as follows:

- The model proved that the magnetic vector potential is affected, quantitatively, by the crack orientation and this was demonstrated theoretically and numerically.
- The impedance showed to be a good and effective inspector for the existence of hidden and internal cracks, to locate them and even to determine their orientation.
- The reactance is affected by the crack orientation more than the resistance of the absolute sensor.

Finally, we showed that the HHO used for the resolution of the inverse problem provide a good alternative to predicate the crack orientation in case when the direct methods fail to accomplish the mission.
In light of the obtained results, we notice that the proposed NDT-EC solution is quite effective and provides very accurate results as well as its ease of conception and its low cost. The angle of crack orientation has a large influence and precise sensibility to the eddy current components,the magnetic flux density and the impedance. The provided results allows the prediction of the crack orientation under static loading, and the crack propagation and the calculation of parameters like the SIF, the J-integral and the CTOD under dynamic or fatigue loading.
Through the use of NDT-EC, all parameters of fracture mechanics mentioned in this work can be determined. The proposed solutions are ready to use, especially for hidden and/or micro cracks with a noticeable accuracy, ease of access and remarkable performance.
As perspectives for this work, we can mention some of them as follows:

- Experimental validation of the proposed approaches and the use of advanced sensing technologies.

- Detection of the orientation crack with other type of sensors such as the differential sensor, the array sensor, the planar sensor and sensors with specific shapes.
- Study of the interaction between multi cracks and its effect on their orientations.
- Utilization of other new optimization algorithms for crack parameters estimation.
- Numerical investigation of the electromagnetic and mechanical coupling to get more realistic simulation of the NDT-EC technique.
- Prediction of the cark orientation using artificial intelligence techniques.

Bibliography

[1] P. M. Yu and P. John. Squid magnetometers for depth-selective, oriented, eddy current imaging. *Review of Progress in QNDE*, pages 67–74, 1998.

[2] L. Perez, L. J. Hir, C. Dolabdjian, and L. Butin. Investigation in detection of fatigue cracks under rivet head airframe using improved gmr magnetometer in an eddy current system. *Journal of electrical engineering*, pages 73–76, 2004.

[3] C. Dolabdjian and L. Perez. Improvement in subsurface fatigue cracks under airframes fasteners detection using improved rotating giant magneto-resistance magnetometer head. *Insight-Non-Destructive Testing and condition Monitoring*, pages 133–136, 2006.

[4] H. Rimond, C. Cordier, S. Saez S, and C. Dolabdjian. Giant magnetoimpedance sensor for non destructive evaluation eddy current system. *Sensor Letters*, pages 437–441, 2009.

[5] Y. Z. Lei and W. Zhang. Transient electromagnetic field due to a focusing coil above a conducting plate. *in: Proceedings of CSSE*, pages 119–128, 2010.

[6] W. Zhang and Y. Z. Lei. Analytical solution of eddy current problem due to a figure 8 shaped coil above a conducting plate. *Nondestr Test*, page 57–60, 2007.

[7] G. Yang, Z Zeng, Y. Deng, X. Liu, L. Udpa, A. Tamburrino A, and al. 3d ec-gmr sensor system for detection of subsurface defects at steel fastener sites. *NDT E E Int*, pages 20–28, 2012.

[8] H. Rimond, c. Cordier, and C. Dolabdjian. Eddy-current non-destructive testing system for the determination of crack orientation. *NDT E Int*, page 24–29, 2014.

[9] Y. Chaofeng, Y. Huang, L. Udpa, and S. S. Udpa. Differential sensor measurement with rotating current excitation for evaluating multilayer structures. *IEEE Sens J*, page 782–789, 2015.

[10] F. Mengban, Q. Wang, B. Cao, B. Ye, A.I. Sunny, and G. Tian. Frequency optimization for enhancement of surface defect classification using the eddy current technique. *Sensors*, page 16: 649, 2016.

[11] Y. Chaofeng, A. Rosell, M. Haq, E. Stitt, L. Udpa, and S. Udpa. Ec probe with orthogonal excitation coils and tmr sensor for cfrp inspection. *Int J Appl Electromagnet Mech*, pages 1247–1255, 2019.

[12] A. S. Repelianto, N. Kasai, K. Sekino, M. Matsunaga, and L.Q. Trung. Flaw detection in aluminum plates using a rotating uniform eddy current probe with two pairs of excitation coils. *Metals*, page 9: 1069, 2019.

[13] X. Zhiyuan, W. Xiang, and D. Yiming. Rotating focused field eddy-current sensing for arbitrary orientation defects detection in carbon steel. *Sensors*, pages 23–39, 2020.

[14] J. J. Duga, W. H. Fisher, R. W. Buxhaum, A. R. Rosenfield, A. R. Buhr, E. J. Honton, and S. C. McMillan. *The economic effects of fracture in the United States*. NBS Special Publication, USA, 1983.

[15] R. L. Jay and P. B. Joseph. Leonardo da vinci's tensile strength tests: implications for the discovery of engineering mechanics. *Civil Engineering and Environmental Systems*, pages 1–8, 2000.

[16] A. A. Griffith. The phenomena of rupture and flow in solids. *Philosophical Transactions of The Royal Socity A*, pages 582–593, 1920.

[17] C. E. Inglis. Stresses in a plate due to the presence of cracks and sharp corners. *the Institute of Naval Architects*, pages 3–17, 1913.

[18] G. R. Irwin. Fracture dynamics. *Fracturing of Metals*, pages 147–166, 1948.

[19] G. R. Irwin. Onset of fast crack propagation in high strength steel and aluminum alloys. Technical report, Naval Research Laboratories Report 4763, 1956.

[20] G. R. Irwin. Analysis of stresses and strains near the end of a crack traversing a plate. *Journal of Applied Mechanics*, pages 361–364, 1957.

[21] H. M. Westergaard. Bearing pressures and cracks. *Journal of Applied Mechanics*, pages A49–A53, 1939.

[22] A. A. Wells. *The condition of fast fracture in aluminum alloys with particular reference to comet failures*. British Welding Research Association, UK, 1955.

[23] D. H. Winne and B. M. Wundt. Application of the griffith-irwin theory of crack propagation to the bursting behavior of disks, including analytical and experimental studies. *Transactions of the American Society of Mechanical Engineers*, pages 1643–1655, 1958.

[24] P. C. Paris, M. P. Gomez, and W. P. Anderson. A rational analytic theory of fatigue. *The Trend in Engineering*, pages 9–14, 1961.

[25] G. R. Irwin. Plastic zone near a crack and fracture toughness. In *Proceedings of Sagamore Research Conference*, 1960.

[26] D. S. Dugdale. Yielding in steel sheets containing slits. *Journal of the Mechanics and Physics of Solids*, pages 100–104, 1960.

[27] G. I. Barenblatt. The mathematical theory of equilibrium cracks in brittle fracture. *Advances in Applied Mechanics*, pages 55–129, 1962.

[28] A. A. Wells. Unstable crack propagation in metals: Cleavage and fast fracture. In *Proceedings of the Crack Propagation Symposium*, 1961.

[29] J. R. Rice. A path independent integral and the approximate analysis of strain concentration by notches and cracks. *Journal of Applied Mechanics*, pages 379–386, 1968.

[30] J. D. Eshelby. The continuum theory of lattice defects. *Solid State Physics*, pages 79–144, 1956.

[31] J. W. Hutchinson. Singular behavior at the end of a tensile crack tip in a hardening material. *Journal of the Mechanics and Physics of Solids*, pages 13–16, 1968.

[32] J. R. Rice and G. F. Rosengren. Plane strain deformation near a crack tip in a power-law hardening material. *Journal of the Mechanics and Physics of Solids*, pages 1–12, 1968.

[33] J. A. Begley and J. D. Landes. The j-integral as a fracture criterion. *Fracture Toughness*, pages 1–20, 1972.

[34] ASTM. Standard test method for JIC. Standard, American Society for Testing and Materials, 1981.

[35] C. F. Shih and J. W. Hutchinson. Fully plastic solutions and large-scale yielding estimates for plane stress crack problems. *Journal of Engineering Materials and Technology*, pages 289–295, 1976.

[36] V. Kumar, M. D. German, and C. F. Shih. An engineering approach for elastic-plastic fracture analysis. Standard, Electric Power Research Institute, 1981.

[37] C. F. Shih. Relationship between the j-integral and the crack opening displacement for stationary and extending cracks. *Journal of the Mechanics and Physics of Solids*, pages 305–326, 1981.

[38] H. Tada, P. C. Paris, and G. R. Irwin. *The stress analysis of cracks handbook (2nd ed.)*. Paris Productions, Inc., France, 1985.

[39] F. Z. Li, C. F. Shih, and A. Needleman. A comparison of methods for calculating energy release rates. *Engineering Fracture Mechanics*, pages 405–421, 1985.

[40] C. F. Shih, P. Paris, and G. Irwin. On cracks in rectilinearly anisotropic bodies. *International Journal of Fracture Mechanics*, pages 189–203, 1965.

[41] A. Karlsson and J. Backlund. J-integral at loaded crack surfaces. *International Journal of Fracture*, pages R311–R314, 1978.

[42] T. K. Hellen and W. S. Blackburn. The calculation of stress intensity factors for combined tensile and shear loading. *International Journal of Fracture*, pages 605–617, 1975.

[43] D. M. Tracy. Finite element solutions for crack tip behavior in small-scale yielding. *Journal of Engineering Materials and Technology*, pages 146–151, 1976.

[44] C. F. Shih. Relationship between crack tip opening displacement for stationary and extending cracks. *Journal of Mechanics and Physics of Solids*, pages 305–326, 1981.

[45] L. B. Freund. Dynamic crack propagation. In *Mechanics of Fracture*, pages 105–134. American Society of Mechanical Engineers, USA, 1976.

[46] L. B. Freund. Crack propagation in an elastic solid subjected to general loading–i. constant rate of extension. *Journal of the Mechanics and Physics of Solids*, pages 129–140, 1972.

[47] L. B. Freund. Crack propagation in an elastic solid subjected to general loading–ii. nonuniform rate of extension. *Journal of the Mechanics and Physics of Solids*, pages 141–152, 1972.

[48] L. B. Freund. Crack propagation in an elastic solid subjected to general loading–iii. stress wave loading. *Journal of the Mechanics and Physics of Solids*, pages 47–61, 1973.

[49] L. B. Freund. *Dynamic Fracture Mechanics*. Cambridge University Press, Cambridge, UK, 1990.

[50] M. F. Kanninen and C. H. Poplar. *Advanced Fracture Mechanics*. Oxford University Press, New York, 1985.

[51] L. R. F. Rose. Recent theoretical and experimental results on fast brittle fracture. *International Journal of Fracture*, pages 799–813, 1976.

[52] C. Atkinson and J. D. Eshlby. The flow of energy into the tip of a moving crack. international. *Journal of Fracture Mechanics*, pages 3–8, 1968.

[53] G. C. Sih. Dynamic aspects of crack propagation. In *Inelastic Behavior of Solids*, pages 607–633. McGraw-Hill, New York, 1970.

[54] L. B. Freund. Energy flux into the tip of an extending crack in an elastic solid. *Journal of Elasticity*, pages 341–349, 1972.

[55] B. Moran and C. F. Shih. A general treatment of crack tip contour integrals. *International Journal of Fracture*, pages 295–310, 1987.

[56] S. N. Atluri. Path independent integrals in finite elasticity and inelasticity, with body forces,inertia, and arbitrary crack face conditions. *Engineering Fracture Mechanics*, pages 341–369, 1982.

[57] K. Kishimoto, S. Aoki, and M. Sakata. On the path independent integral j. *Engineering Fracture Mechanics*, pages 841–850, 1980.

[58] K. Kishimoto, S. Aoki, and M. Sakata. Standard test methods for notched bar impact testing of metallic materials. standard, American Society for Testing and Materials, 1988.

[59] D. Gregoire, H. Maigre, J. Rethore, and A. Combescure. Dynamic crack propagation under mixed-mode loading – comparison between experiments and x-fem simulations. *International Journal of Solids and Structures*, pages 6517–6534, 2007.

[60] H. Maigre and D. Rittel. Mixed-mode quantification for dynamic fracture initiation: application to the compact compression specimen. *International Journal Solids Structures*, pages 3233–3244, 1993.

[61] A. Gravouil, T. Elguedj, and H. Maigre. An explicit dynamics extended finite element method. part 1: Mass lumping for arbitrary enrichment functions. *Computer Methods in Applied Mechanics and Engineering*, pages 2297–2317, 2009.

[62] A. Gravouil, T. Elguedj, and H. Maigre. An explicit dynamics extended finite element method. part 2: Element-by-element stable-explicit/explicit dynamic scheme. *Computer Methods in Applied Mechanics and Engineering*, pages 2318–2328, 2009.

[63] P. Paris, M. Gomez, and W. Anderson. A rational analytic theory of fatigue. *The Trend in Engineering*, pages 9–14, 1961.

[64] M. Pais, N. H. Kim, and T. A. Davis. Reanalysis of the extended finite element method for crack initiation and propagation. In *Structural Dynamics and Materials Conference*, 2010.

[65] Y. Liu and S. Mahadevan. Threshold stress intensity factor and crack growth rate prediction under mixed-mode loading. *Engineering Fracture Mechanics*, pages 332–345, 2007.

[66] R. J. Nuismer. An energy release rate criterion for mixed mode fracture. *International Journal of Fracture*, pages 708–712, 1975.

[67] F. Erdogan and G. C. Sih. On the crack extension in plates under plane loading and transverse shear. *Journal of Basic Engineering*, pages 519–525, 1963.

[68] H. A. Richard, M. Fulland, and M. Sander. Theoretical crack path prediction. *Fatigue and Fracture of Engineering Materials and Structures*, pages 3–12, 2005.

[69] N. Sukumar and J. H. Prévost. Modeling quasi-static crack growth with the extended finite element method, part i: Computer implementation. *International Journal of Solids and Structures*, pages 7513–7537, 2003.

[70] N. Moes, J. Dolbow, and T. Belytschko. A finite element method for crack growth without remeshing. *International Journal for Numerical Methods in Engineering*, pages 131–150, 1999.

[71] H. Brauer, M. Ziolkowski, K. Weise, M. Carlstedt, R. P. Uhlig, and M. Zec. *Motion-Induced Eddy Current Techniques for Non-Destructive Testing and Evaluation*. The Institution of Engineering and Technology, USA, 2019.

[72] T. Aastroem. From fifteen to two hundred ndt methods in fifty years. In *World Conference on Nondestructive Testing*, 2008.

[73] X. Wu, C. Zhang, and P. Goldberg. Early pottery at 20000 years ago in xianrendong cave. *Science*, pages 1696–1700, 1696.

[74] M. R. Kandroodi, B. N. Araabi, and M. N. Ahmadabadi. Detection of natural gas pipeline defects using magnetic flux leakage measurements. In *Iranian Conference on Electrical Engineering*, 2013.

[75] M. M. Salama, B. J. Nestleroth, M. A. Maes, C. Rodriguez, and D. Blumer. Characterization of the accuracy of the mfl pipeline inspection tools. In *Proceedings of International Conference on Ocean, Offshore and Arctic Engineering*, 2012.

[76] H. Toepfer H. Brauer, M. Ziolkowski. Defect detection in conducting materials using eddy current testing techniques. *Serbian Journal of Electrical Engineering*, pages 535–549, 2014.

[77] D. Mery R. Silva. State of the art of weld seam inspection by radiographic testing part 1, image processing. *Materials Evaluation*, pages 643–647, 2007.

[78] C. A. Harding and G. R. Hugo. Review of literature on probability of detection for liquid penetrant nondestructive testing. Technical report, Defence Science and Technology Organisation (Australia), 2011.

[79] J. Vrana, A. Zimmer, and H. Lohmann. Evolution of the ultrasonic inspection over the past decades on the example of heavy rotor forgings. In *World Conference on Non-Destructive Testing*, 2016.

[80] J. Krautkrämer and H. Krautkrämer. *Material test with ultrasound*. Springer-Verlag, Berlin, 1990.

[81] C. J. Hellier. *Handbook of Nondestructive Evaluation*. McGraw-Hill Education LLC, New York, 2013.

[82] F. Foerster. Theoretical and experimental principles of non-destructive material testing i. destination pulse method. *Magazine for metalwork*, pages 163–171, 1952.

[83] J. E. See. *Visual Inspection: A Review of the Literature*. Sandia National Laboratories Albuquerque, New Mexico, 2012.

[84] X. Guirong, G. Xuesong, Q. Yuliang, and G. Yan. Analysis and innovation for penetrant testing for airplane parts. *Procedia Engineering*, pages 1438–1442, 2015.

[85] K. G. Boving. *NDE Handbook. Non-Destructive Examination Methods for Condition Monitoring*. Elsevier Ltd. UK, 1989.

[86] International Atomic Energy Agency. Guidelines on training, examination and certification in digital industrial radiology testing (rt-d). Technical report, Vienna Centre of IAEA, 2015.

[87] C. H. Chen. *ultrasonic and advanced methods for nondestructive testing and material characterization*. World Scientific Publishing Co. Pte. Ltd. Singapore, 2007.

[88] V. Vavilov and D. Burleigh. *Infrared Thermography and Thermal Nondestructive Testing*. Springer International Publishing, Switzerland, 2020.

[89] International Atomic Energy Agency. Eddy current testing at level 2. Technical report, Vienna Centre of IAEA, 2011.

[90] D. E. Abdelli. *Modélisation par les volumes finis d'un problème de contrôle non destructif de forme complexe*. Magister manuscript, Université Mohamed Kheider de Biskra (Algérie), 2014.

[91] J. G. Martín, J. G. Gil, and E. V. Sánchez. Non-destructive techniques based on eddy current testing. *Sensors*, 2011.

[92] P. Xu, S. Huang, and W. Zhao. Differential eddy current testing sensor composed of double gradient winding coils for crack detection. In *Proceedings of the IEEE Sensors Applications Symposium*, 2010.

[93] J. Bae and S. Kim. Hot wire inspection using eddy current. In *Proceedings of the IEEE Instrumentation and Measurement Technology Conference*, 2001.

[94] A. L. Ribeiro, F. Alegria, O. Postolache, and H. Ramos. Eddy current inspection of a duralumin plate. In *Proceedings of IEEE Instrumentation and Measurement Technology Conference*, Singapore, 2009.

[95] J. Tian, D. Li, and L. Ye. Study on braking characteristics of a novel eddy current-hydraulic hybrid retarder for heavy-duty vehicles. *IEEE Transactions on Energy Conversion*, pages 1658–1666, 2020.

[96] P. J. Wang and S. J. Chiueh. Analysis of eddy-current brakes for high speed railway. *IEEE Transactions on Magnetics*, pages 1237–1239, 1998.

[97] H. Y. Zhang, Z. Q. Chen, X. G. Hua, Z. W. Huang, and H. W. Niu. Design and dynamic characterization of a large-scale eddy current damper with enhanced performance for vibration control. *Mechanical Systems and Signal Processing*, page 106879, 2020.

[98] A. Zaoui. *Contribution à la Modélisation de CND par Matrice des capteurs à Courants de Foucault*. Phd thesis, Ecole Militaire Polytechnique d'Alger (Algérie), 2008.

[99] S. Harzallah. *Contribution à l'analyse des endommagements par la technique du contrôle non-destructif et l'utilisation des capteurs à courant de Foucault : Investigation numérique et expérimentale*. Phd thesis, Université de Sciences et Technologie Houari Boumedienne d'Alger (Algérie), 2017.

[100] S. Hughes. Magnetic force, magnetic fields and ampere's law. Technical report, Massachusetts Institute of Technology (USA), 2014.

[101] M. H. Al-Taweel T. R. Al-Shaikhli, B. A. Ulhisham. The implementations and applications of ampere's law to the theory of electromagnetic fields. *International Journal of Advanced Science and Technology*, pages 515–525, 2019.

[102] R. Bansal. *Handbook of Engineering Electromagnetics*. Marcel Dekker, New York, 2004.

[103] S. Zerguini. *Elaboration de Modèles Electromagnétiques Caractérisant le Contrôle Non Destructif par Courant de Foucault*. Phd thesis, Université de Constantine (Algérie), 2009.

[104] G. W. C. Kaye and T. H. Laby. Values for some common materials. https://en.wikipedia.org/wiki/Permeability_(electromagnetism).

[105] A. Dina, G. Reham, I. Kareem, M. Mahitab, Z. Yomna, G. Athnasious, H. Ahmed, H. Ahmed E.-N Eman, and A.-Z. Mohamed. Electrically conductive concrete. In *Proceedings of Annual Conference of the Canadian Society of Civil Engineering*, 2018.

[106] N. Benhadda. *Modélisation et Etude pour la Réalisation d'un Capteur à Courants de Foucault en Mode Différentiel pour le Contrôle non Destructif.* Phd thesis, Université Hadj Lakhdar de Batna (Algérie), 2015.

[107] B. Helifa. *Contribution a la simulation du cnd par courants de foucault en vue de la caracterisation des fissures debouchantes.* Phd thesis, Universite de Nantes (France), 2012.

[108] U. Tröltzsch, F. Wendler, and O. Kanoun. Simplified analytical inductance model for a single turn eddy current sensor. *Sensors and Actuators*, pages 11–21, 2013.

[109] N. Oukacine. *Utilisation des réseaux de neurones pour la reconstitution de défauts en évaluation non destructive.* Magister manuscript, Université Mouloud Mammeri de Tizi-ouzou (Algérie), 2012.

[110] A.-E. Lakhdari. *Etude et modelisation de capteurs en CND par courants de foucault :application a la detection des fissures.* Magister manuscript, Université Mohamed Khider de Biskra (Algérie), 2011.

[111] T. Bouchala. *Développement de Méthodes Rapides pour la Résolution des Problèmes Directes dans les Systèmes de CND par Courants de Foucault.* Phd thesis, Université Hadj Lakhdar de Batna (Algérie, 2014.

[112] Y. Le Bihan, J. Pavo, and C. Marchand. Calculation of ect signal of a minute crack by fem-bim hybrid method. *The European Physical Journal Applied Physics*, page 355–360, 2004.

[113] J. R. Nagel. Finite-difference simulation of eddy currents in nonmagnetic sheets via electric vector potential. *IEEE Transactions on Magnetics*, pages 1–8, 2019.

[114] F. Moukalled, L. Mangani, and M. Darwish. *The Finite Volume Method in Computational Fluid Dynamics.* Springer Cham Heidelberg, New York, 2016.

[115] A. Cheriet. *Contribution à la modelisation tridimensionnelle par la methode des volumes finis de dispositifs electromagnetiques.* Phd thesis, Universite Mohamed Khider de Biskra (Algérie), 2007.

[116] V. Doirat. *Contribution à la modélisation de systèmes de Contrôles Non Destructifs par Courants de Foucault. Application à la caractérisation physique et dimensionnelle de matériaux de l'aéronautique*. Phd thesis, Ecole Polytechnique de l'Université de Nantes (France), 2007.

[117] C. V. Dodd and W. E. Deeds. Analytical solutions to eddy current probe coil problems. *Journal of Applied Physics*, pages 2829–2838, 1968.

[118] Y. Choua. *Application de la méthode des Eléments Finis pour la Modélisation de Configurations de Contrôle non Destructif par Courants de Foucault*. Phd thesis, Université de Paris Sud 11 (France), 2010.

[119] M. Guesmi, B. E. Hachi, M. Badaoui, M. S. Goual, and A. Benmessaoud. Dynamic analysis by xfem of planar structures containing stationarycracks. In *1 er Séminaire national de genie civil souk-ahras, Algerie*, 2012.

[120] M. Guesmi, B. E. Hachi, M. Badaoui, M. S. Goual, and A. Benmessaoud. Dynamic stress intensity factor computation by using xfem formulation. *Applied Mechanics and Materials*, pages 716–720, 2012.

[121] K. C. Nehar, B. K. Hachi, M. Badaoui, M. Guesmi, and A. Benmessaoud. The evaluation of the spectral dynamic stress intensity factor by the x-fem method coupled with the spectral modal analysis. *Asian journal of civil engineering (building and housing)*, pages 771–784, 2016.

[122] A. C. Lahrech. *Contribution à l'Etude de l'E-CND par Courants de Foucault de Matériaux Composites à Fibres de Carbone*. Phd thesis, Université Batna 2 (Algérie), 2020.

[123] M. Guesmi, S. Harzallah, and A. Kouzou. New non-destructive testing approach based on eddy current for crack orientation detection and parameter estimation. *International Journal of Applied Electromagnetics and Mechanics*, pages 431–451, 2021.

[124] R. M'hemed and M. Fèliachi. 3-d movement simulation techniques using fe methods: Application to eddy current non-destructive testing. *NDT E E International*, pages 35–42, 2007.

[125] S. Harzallah, R. Rebhi, M. Chabaat, and A. Rabehi. Eddy current modelling using multi-layer perceptron neural networks for detecting surface cracks. *Frattura ed Integrità Strutturale*, pages 147–155, 2018.

[126] Z. Bofang. *The Finite Element Method: Fundamentals and Applications in Civil, Hydraulic, Mechanical and Aeronautical Engineering.* John Wiley & Sons Singapore Pte, Ltd, 2018.

[127] M. Rachek. *Modélisation par éléments finis de systèmes électromagnétiques en mouvement de structures tridimensionnelles.* Phd thesis, Universite Mouloud Mammeri de Tizi-Ouzou (Algérie), 2007.

[128] A. Abdou. *Contrôle non Destructif (CND) :Étude et Modélisation d'un capteur inductif à Courants de Foucault.* Phd thesis, Université Batna 2 (Algérie), 2018.

[129] N. Benhadda. *Modélisation des Capteurs Inductifs à Courants de Foucault.* Magister manuscript, Université El Hadj Lakhdar de Batna (Algérie), 2006.

[130] S. Bennoud and M. Zergoug. Modeling and simulation for 3D eddy current testing in conducting materials. *International Journal of Aerospace and Mechanical Engineering*, pages 754–757, 2014.

[131] S. K. Burke. A benchmark problem for computation of dz in eddy-current nondestructive evaluation (nde). *Journal of Nondestructive Evaluation*, pages 34–41, 1988.

[132] H. A. Sabbagh and S. K. Burke. Benchmark problems in deddy-current nde. *Review of Progress in Quantitative Nondestructive Evaluation*, pages 2017–224, 1992.

[133] J. R. Bowler, S. A. Jenkins, L. D. Sabbagh, and H. A. Sabbagh. Eddy current probe impedance due to a volumetric flaw. *journal of Applied Physics*, pages 1107–1114, 1991.

[134] S. Harzallah and M. Chabaat. 3d-fem computation and experimental of eddy currents for characterization of surface cracks. *International Journal of Structural Integrity*, pages 603–610, 2017.

[135] X. Zhiyuan X, W. Xiang, and D. Yiming. Rotating focused field eddy-current sensing for arbitrary orientation defects detection in carbon steel. *Sensors*, pages 23–45, 2020.

[136] A. S. Repelianto and N. Kasai. The improvement of flaw detection by the configuration of uniform eddy current probes. *Sensors*, page 397, 2019.

[137] S. Mirjalili and A. Lewis. The whale optimization algorithm. *Advances in Engineering Software*, pages 51–67, 2016.

[138] J. H. Holland. Genetic algorithms. *Scientific American*, page 66–72, 1992.

[139] I. Rechenberg. Evolutions strategien. *Springer Berlin Heidelberg*, page 83–114, 1978.

[140] D. Simon. Biogeography-based optimization. *IEEE Trans Evol Comput*, page 702–13, 2008.

[141] S. Kirkpatrick, C. D. Gelatt, and M. P. Vecchi. Optimization by simmulated annealing. *Science*, page 671–80, 1983.

[142] R. A. Formato. Central force optimization: A new metaheuristic with applications in applied electromagnetics. *Prog Electromag Res*, page 425–91, 2007.

[143] B. Webster and P. J. Bernhard. A local search optimization algorithm based on natural principles of gravitation. In *Proceedings of the 2003 international conference on information and knowledge engineering*, 2003.

[144] H. Shah-Hosseini. Principal components analysis by the galaxy-based search algorithm: a novel metaheuristic for continuous optimisation. *Int J Comput Sci Eng*, page 132–40, 2011.

[145] M. Dorigo, M. Birattari, and T. Stutzle. Ant colony optimization. *IEEE Comput Intell*, page 28–39, 2006.

[146] A. A. Heidari, S. Mirjalili, H. Faris, I. Aljarah, M. Mafarja, and H. Chen. Harris hawks optimization: Algorithm and applications. *Future Generation Computer Systems*, pages 1–23, 2019.

Personal Bibliography

Publications

1. **M. GUESMI** and S. Harzallah and A. Kouzou, New nondestructive testing approach based on eddy current for crack orientation detection and parameter estimation, *International Journal of Applied Electromagnetics and Mechanics*, pp. 431-451, 2021.

2. B. K. Hachi, **M. GUESMI** and M. Haboussi, Modeling of planar embedded cracks of arbitrary shape under non uniform mode I loadings, *Applied Mechanics and Materials Journal*, pp. 568-572, 2012.

3. **M. GUESMI**, B. K. Hachi, M. Badaoui, M. S. Goual and A. Benmessaoud, Dynamic stress intensity factor computation by using XFEM formulation, *Applied Mechanics and Materials Journal*, pp. 716-720, 2012.

4. A. Benmessaoud, M. Badaoui, B. K. Hachi, C. K. Nehar and **M. GUESMI**, Modal stress intensity factor using extended finite element method, *Applied Mechanics and Materials Journal*, pp. 686-690, 2012.

International Communications

1. **M. GUESMI**, K. Guesmi, S. Harzallah and B. Benchikh, Numerical analysis of 2D crack orientation detection using the particle swarm optimization, *International Conference on Artificial Intelligence in Renewable Energetic Systems*, 20-22 November 2022, Tamenrasset (Algeria).

2. **M. GUESMI**, K. Guesmi, S. Harzallah and B. Benchikh, Detection of crack orientation using the non-destructive testing by eddy current, *Séminaire International en Génie Industriel et Mathématiques Appliquées*, 23-24 October 2022, Skikda (Algeria).

3. H. A. HOUA, B. K. Hachi, **M. GUESMI**, M. Haboussi and M. Badaoui, Dynamic modeling by XFEM of cracked 2D structures containing inclusion, *21ème Congrès Français de la Mécanique*, 26-30 August 2013, Bordeaux (France).

4. M. R. KIRED, B.K. Hachi, **M. GUESMI**, S. Rechak and M. Badaoui, Dynamic and fatigue modeling of cracked structures containing voids by XFEM, *21ème Congrès Français de la Mécanique*, 26-30 August 2013, Bordeaux (France).

5. K. C. Nehar, M. Badaoui, B. K. Hachi, **M. GUESMI** and A. Benmessaoud, Modal spectral analysis of planar cracked structures subjected to seismic excitations by the extended finite element method, *21ème Congrès Français de la Mécanique*, 26-30 August 2013, Bordeaux (France).

6. K. C. Nehar, M. Badaoui, B. K. Hachi, **M. GUESMI** and A. Benmessaoud, Modélisation de la fissuration des structures en béton armé par la méthode X-FEM, *1er Séminaire International de Génie Civil*, 06-07 March 2013, Bechar (Algeria).

7. K. C. Nehar, M. Badaoui, B. K. Hachi, **M. GUESMI** and A. Benmessaoud, Modélisation modale spectrale par la X-FEM des structures planes fissurées soumises à des excitations sismiques, *1er Congrès International de Génie Civil et d'hydraulique*, 10-11 December 2012, Guelma (Algeria).

8. **M. GUESMI**, B. K. Hachi, M. Badaoui, M.S. Goual and A. Benmessaoud, X-FEM modeling in dynamic analysis of planar cracked structures, *Colloque International Reduction du risque sismique*, 10-11 October 2012, Chlef (Algeria).

9. **M. GUESMI**, B. K. Hachi, M. Badaoui, M. S. Goual and A. Benmessaoud, Dynamic stress intensity factor computation by using XFEM formulation, *International Conference on Mechanical and Aerospace Engineering*, 7-8 July 2012, Paris (France) (Received the best presentation award).

National Communications

1. K. C. Nehar, M. Badaoui, B. K. Hachi, **M. GUESMI** and A. Benmessaoud, Modélisation en dynamique des structures fissurées par X-FEM et l'analyse modale spectrale, *1er Séminaire National de Génie Civil*, 22-23 October 2012, Souk Ahras (Algeria).

2. **M. GUESMI**, B. K. Hachi, M. Badaoui, M.S. Goual and A. Benmessaoud, Dynamic analysis by XFEM of planar structures containing stationary cracks, *1er Séminaire National de Génie Civil*, 22-23 October 2012, Souk Ahras (Algeria).

3. B. K. Hachi, **M. GUESMI** and M. Haboussi, Analyse tridimensionnelle des fissures internes dans des structures soumises à des charges en mode I arbitrairement reparties, *Les 1ers Workshops de Génie Civil*, 11-12 April 2012, Djelfa (Algeria).

4. B. K. Hachi, **M. GUESMI** and M. Haboussi, Etude en 3D des fissures internes dans un matériau fragile sous un chargement à répartition arbitraire, *Séminaire National de Mécanique*, 6–7 December 2011, Laghouat (Algeria).

5. **M. GUESMI**, B. K. Hachi, M. Badaoui and S. Rechak, Modélisation des fissures planes de forme quelconque dans des structures 3D par la méthode des fonctions de poids a incrémentation numérique, *9ème Congrès National de la Physique et de ses Applications*, 24-26 October 2010, Ouargla (Algeria).